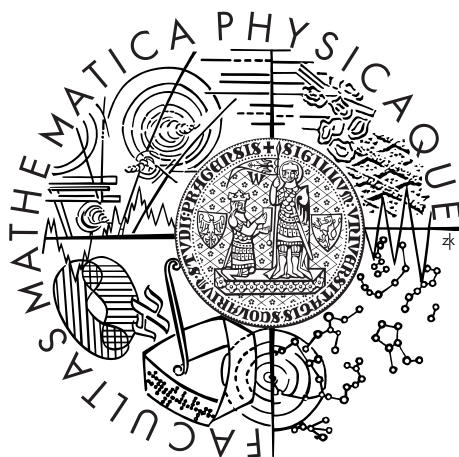


Univerzita Karlova v Praze  
Matematicko-fyzikální fakulta

## DIPLOMOVÁ PRÁCE



Jan Zubáč

## Elektronové vlastnosti sloučenin $R\text{Pd}_5\text{Al}_2$

Katedra fyziky kondenzovaných látek

Vedoucí diplomové práce: doc. Mgr. Pavel Javorský, Dr.

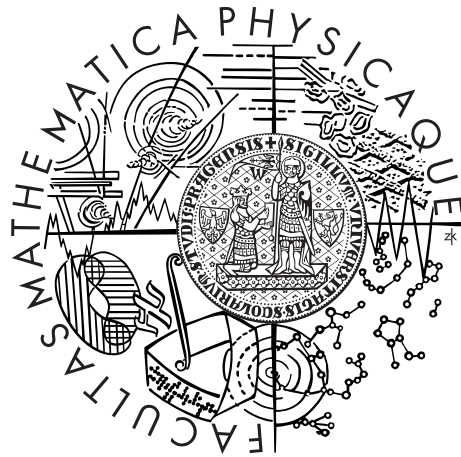
Studijní program: Fyzika

Studijní obor: Fyzika kondenzovaných soustav  
a materiálů

Praha 2016

Charles University in Prague  
Faculty of Mathematics and Physics

## MASTER THESIS



Jan Zubáč

## Electronic properties of $RPd_5Al_2$ compounds

Department of Condensed Matter Physics

Supervisor of the master thesis: doc. Mgr. Pavel Javorský, Dr.

Study programme: Physics

Specialization: Physics of Condensed Matter  
and Materials

Prague 2016

First and foremost, I would like to thank my supervisor, doc. Mgr. Pavel Javorský, Dr., for his guidance during my studies, for his patience and kind attitude and also for introducing me into the world of neutron scattering experiments. Then, I would like to acknowledge my colleagues from the Department of Condensed Matter Physics who helped me during daily work in the laboratory as well as with solving different problems and overcoming difficulties I came across. Namely, I would like to thank RNDr. Marie Kratochvílová, Ph.D., Ing. Barbora Vondráčková, Mgr. Michal Vališka, Mgr. Attila Bartha, Mgr. Petr Opletal and Mgr. Petr Doležal. I appreciate Bc. Karel Pajskr for helping me with the program I used for the crystal field analysis and also for his comments and fruitful discussions. I would like to thank Bc. Kristina Vlášková.

I must also acknowledge RNDr. Jan Prokleška, PhD., RNDr. Róbert Tarasenko, Ph.D., RNDr. Vladimír Tkáč, Ph.D., who helped me during measurements in the JLMS laboratory and Bc. Petr Proschek who performed magnetization measurements using Hall probes. My thanks go to doc. RNDr. Martin Diviš, CSc. for performing the theoretical calculations and for discussions about crystal field and to Ing. Jiří Kulda, CSc. for his suggestions concerning the inelastic neutron scattering data. I am very thankful to Mgr. Jana Leová for reading the manuscript and correcting grammatical mistakes.

Last but not least, I would like to thank my family and particularly my parents for their unconditional support and encouragement during all my studies.

I declare that I carried out this master thesis independently, and only with the cited sources, literature and other professional sources.

I understand that my work relates to the rights and obligations under the Act No. 121/2000 Coll., the Copyright Act, as amended, in particular the fact that the Charles University in Prague has the right to conclude a license agreement on the use of this work as a school work pursuant to Section 60 paragraph 1 of the Copyright Act.

In ..... date .....

signature of the author

Název práce: Elektronové vlastnosti sloučenin  $RPd_5Al_2$

Autor: Jan Zubáč

Katedra: Katedra fyziky kondenzovaných látek

Vedoucí diplomové práce: doc. Mgr. Pavel Javorský, Dr., Katedra fyziky kondenzovaných látek

Abstrakt:

Tato práce se zabývá magnetickými vlastnostmi sloučeniny  $NdPd_5Al_2$  studovanými pomocí magnetizačních měření, měření měrných tepel a rozptylu neutronů. Sloučenina krystalizuje v tetragonální grupě  $I4/mmm$  s mřížovými parametry  $a = 4.147 \text{ \AA}$  a  $c = 14.865 \text{ \AA}$ , magneticky se uspořádává pod  $T_N = 1.3 \text{ K}$  a vykazuje magnetokrystalovou anizotropii kvůli působení krystalového pole. Magnetický fázový diagram se podobně jako u strukturně příbuzných sloučenin  $RTX_5$  a  $R_2TX_8$  vyznačuje přítomností dvou různých magnetických fází. Antiferomagnetická fáze v nulovém poli se propaguje s vektorem  $k = (\frac{1}{2}00)$  a vyznačuje se uspořádáním neodymových momentů o velikosti  $2.22 \mu_B/Nd$  podél tetragonální osy  $c$ , jak bylo zjištěno pomocí neutronové difrakce. Fázový přechod z paramagnetického do magneticky uspořádaného stavu v nulovém poli je fázovým přechodem prvního druhu. Pomocí nepružného rozptylu neutronů jsme detekovali krystalovopolní hladiny o energiích  $3.0 \text{ meV}$ ,  $7.4 \text{ meV}$ ,  $8.6 \text{ meV}$  a  $17.1 \text{ meV}$ . Naše poznatky o krystalovém poli ve sloučenině  $NdPd_5Al_2$  získané pomocí nepružného rozptylu neutronů dále porovnáváme s výsledky analýzy krystalového pole pomocí susceptibilit a výpočtů z prvních principů a konfrontujeme s experimentálními magnetizačními daty a magnetickými měrnými tepley. Výsledky rovněž diskutujeme v kontextu příbuzných sloučenin  $RPd_5Al_2$ ,  $R_2TX_8$  a  $RTX_5$ .

Klíčová slova: magnetismus, supravodivost, krystalové pole

Title: Electronic properties of  $RPd_5Al_2$  compounds

Author: Jan Zubáč

Department: Department of Condensed Matter Physics

Supervisor: doc. Mgr. Pavel Javorský, Dr., Department of Condensed Matter Physics

Abstract:

We have studied magnetic properties of the intermetallic  $NdPd_5Al_2$  compound by means of specific heat and magnetization measurements and neutron scattering. The compound crystallizes in the tetragonal  $I4/mmm$  space group with lattice parameters  $a = 4.147 \text{ \AA}$  and  $c = 14.865 \text{ \AA}$ , orders antiferromagnetically below  $T_N = 1.3 \text{ K}$  and presents large magnetocrystalline anisotropy due to the crystal-field effects. The obtained magnetic phase diagram is characterized by two distinct magnetically ordered phases similarly to structurally related tetragonal  $RTX_5$  and  $R_2TX_8$  compounds. The zero-field antiferromagnetic phase is characterized by the propagation vector  $k = (\frac{1}{2}00)$  and antiferromagnetic coupling of Nd moments along the tetragonal  $c$ -axis with the amplitude of magnetic moments of  $2.22 \mu_B/Nd$  as was revealed by neutron diffraction. The transition from the paramagnetic to magnetically ordered in zero field is the first-order phase transition. The CF excitations in  $NdPd_5Al_2$  were detected by means of INS at 3.0 meV, 7.4 meV, 8.6 meV and 17.1 meV. We further compare our findings about CF in  $NdPd_5Al_2$  obtained from INS, susceptibility analysis and first-principles calculations and confront them with the experimental magnetization and magnetic specific heat data. Our results will be also discussed with respect to related tetragonal  $RPd_5Al_2$ ,  $R_2TX_8$  and  $RTX_5$  compounds.

Keywords: magnetism, superconductivity, crystal field

# Contents

<b>Introduction</b>	<b>2</b>
Outline . . . . .	2
<b>1 Theoretical background</b>	<b>3</b>
1.1 Magnetism of free ions . . . . .	3
1.1.1 Rare earth ions . . . . .	3
1.1.2 Paramagnetism of free ions . . . . .	5
1.2 Magnetism of solids . . . . .	7
1.2.1 Crystal field . . . . .	7
1.2.2 Influence of the crystal field on magnetic properties . . . .	10
1.2.3 Exchange interactions . . . . .	11
1.3 Heat capacity of solids . . . . .	13
<b>2 Experimental techniques</b>	<b>16</b>
2.1 Magnetic measurements . . . . .	16
2.2 Heat capacity . . . . .	16
2.3 Neutron scattering . . . . .	17
2.3.1 Neutron diffraction . . . . .	17
2.3.2 Inelastic neutron scattering . . . . .	18
<b>3 Previous results</b>	<b>21</b>
3.1 Related tetragonal compounds . . . . .	21
3.2 $RPd_5Al_2$ compounds . . . . .	22
<b>4 Results and discussion</b>	<b>24</b>
4.1 Sample preparation . . . . .	24
4.2 Susceptibility and magnetization . . . . .	26
4.3 Specific heat and magnetic phase diagram . . . . .	28
4.4 Magnetic specific heat . . . . .	32
4.5 Neutron diffraction . . . . .	35
4.5.1 Magnetic structure . . . . .	35
4.5.2 Critical behaviour . . . . .	38
4.6 Crystal-field analysis . . . . .	39
4.6.1 Susceptibility fitting and ab-initio calculations . . . . .	39
4.6.2 Inelastic neutron scattering . . . . .	42
4.6.3 Energy-level scheme and specific heat . . . . .	46
4.7 Discussion . . . . .	48
<b>5 Conclusion</b>	<b>51</b>
<b>Bibliography</b>	<b>52</b>

# Introduction

Tetragonal ternary intermetallic compounds of elements with partially filled  $f$ -electron shell attract attention of scientific community due to the broad variety of exciting properties ranging from complex magnetic ordering and pronounced magnetocrystalline anisotropy to unconventional superconductivity and strong electron correlations.

Several of these materials, in particular the cerium-based from  $RTX_5$  and  $R_2TX_8$  series ( $R$  is a rare earth element or actinide,  $T$  represents a transition metal and  $X$  a  $p$ -metal)[1–3], have been extensively studied due to the relationship between magnetism and an unconventional superconductivity which is mediated by magnetic fluctuations and it is thus closely connected to magnetism and properties of  $f$ -electrons. For proper understanding of their often intriguing behaviour, investigation of their isostructural magnetic analogues is of a big importance. Magnetic properties of these analogues are predominantly governed by exchange interactions of RKKY type and CF, which influences fundamentally the magnetocrystalline anisotropy. Neodymium analogues are due to their closeness to the cerium compounds for such studies good candidates.

$RPd_5Al_2$  compounds, which are structurally closely related to  $R_2TX_8$  and  $RTX_5$  compounds, have aroused an interest after the discovery of a paramagnetic unconventional heavy-fermion superconductor  $NpPd_5Al_2$  ( $T_c = 4.9$  K,  $\gamma = 200$  mJ mol $^{-1}$  K $^{-2}$ ) by Aoki et al. in 2007 [4] and a Kondo lattice antiferromagnet  $CePd_5Al_2$  [5] followed by reporting of a pressure-induced superconductivity in this compound [6].

These findings motivated us for the study of  $NdPd_5Al_2$  compound, on which we aim in this work. We have focused in particular on crystal field in the context of anisotropic magnetic properties and detailed examination of the magnetically ordered state and its development in magnetic fields.

## Outline

The thesis is composed of four chapters and it is organized in following way: Chapter 1 provides a theoretical framework from magnetism of free ions to magnetism of solids with the focus on the crystal field and overviews briefly basic concepts of heat capacity of solids. Experimental methods of bulk magnetization and specific heat measurements and employed neutron scattering techniques are presented in Chapter 2. Chapter 3 overviews concisely previously studied related compounds. The principal chapter of the thesis, Chapter 4, consists of two main parts. In the first part (4.2 to 4.5), the results of bulk magnetization and specific heat measurements and details of the magnetic phase diagram are complemented by findings about the magnetic structure studied by neutron diffraction. The second part (4.6) is concerned with crystal field investigated by three different methods including inelastic neutron scattering. Finally, our results are summarized in Conclusion (5).

# 1. Theoretical background

The purpose of this chapter is to introduce concisely an essential theoretical framework related to the topic of the thesis. We will overview the most important equations, definitions and relations between quantities significant for magnetism.

## 1.1 Magnetism of free ions

### 1.1.1 Rare earth ions

Electronic properties of rare earth atoms and ions are particularly given by the incompletely occupied  $4f$  electron shell. Since  $4f$  electrons of rare earths keep their character to a profound extent even after inserting into a solid, free ions are a good starting point for understanding of rare earth magnetism.

The non-relativistic Hamiltonian of a free atom/ion system can be written in a form [7]

$$\mathcal{H} = \mathcal{H}_0 + \mathcal{H}_{\text{res}}, \quad (1.1)$$

where  $\mathcal{H}_0$  consists of the kinetic energy of electrons at positions  $\mathbf{r}_i$ , Coulomb interaction between electrons and a nucleus of an element with an atomic number  $Z$  and an effective spherically symmetric one-electron potential  $V_{\text{eff}}$  which simulates a part of the electron-electron interaction:

$$\mathcal{H}_0 = \sum_i -\frac{\hbar^2}{2m_e} \nabla_i^2 - \frac{Ze'^2}{r_i} + V_{\text{eff}}(r_i). \quad (1.2)$$

$\mathcal{H}_{\text{res}}$  is a so-called residual interaction and involves electron-electron interaction diminished by the effective potential

$$\mathcal{H}_{\text{res}} = \frac{1}{2} \sum_{\substack{i,j \\ i \neq j}} \frac{e'^2}{|\mathbf{r}_i - \mathbf{r}_j|} - \sum_i V_{\text{eff}}(r_i). \quad (1.3)$$

Introducing central potential  $V_{\text{eff}}$  into Eqs. (1.2) and (1.3) simplifies the solution of the problem (1.1) and assures that  $\mathcal{H}_{\text{res}}$  can be treated as a weak disturbance in terms of the perturbation theory. Then an effective one-electron approach (based on e. g. Hartree-Fock approximation or density functional theory) can be employed using one-electron hydrogen-like eigenfunctions of Eq. (1.2) in the form [8]:

$$\psi_{nlm_l m_s}(\mathbf{r}, \sigma) = R_{nl}(r) Y_{lm_l}(\theta, \phi) \chi_{m_s}. \quad (1.4)$$

Here  $R_{nl}$  is a radial wave function,  $Y_{lm_l}$  a spherical harmonic,  $\chi_{m_s}$  a spin function and  $n$ ,  $l$ ,  $m_l$  and  $m_s$  denote principal, azimuthal, magnetic and spin quantum numbers. As it is known, these quantum numbers determine energy of the states in a hydrogen-like atom, magnitude of the orbital angular momentum of individual electrons, its projection on a selected axis (usually  $z$ -axis), respectively projection of their spin. Quantum numbers  $n$  and  $l$  define  $\binom{2(2l+1)}{k}$ -times degenerate eigenstates of  $\mathcal{H}_0$  referred as electron configuration ( $k$  is number of the electrons in the incompletely occupied shell).

Spin and orbital angular momentums of individual electrons couple to form separately a total angular momentum of the ion. For transition elements, including rare earths, Russell-Saunders ( $LS$ ) coupling is well-applicable [9]. In this vector coupling scheme, spin and orbital angular momentums\* of electrons  $\mathbf{s}^{(i)}$  and  $\mathbf{l}^{(i)}$  contribute to give separately the overall spin angular momentum  $\mathbf{S}$  and the overall orbital momentum  $\mathbf{L}$  of and the total angular momentum  $\mathbf{J}$  of the system is then a vector sum of the spin and orbit part, schematically:

$$\mathbf{L} = \sum_i \mathbf{l}^{(i)}, \quad (1.5)$$

$$\mathbf{S} = \sum_i \mathbf{s}^{(i)},$$

Russell-Saunders coupling

$$\mathbf{J} = \mathbf{L} + \mathbf{S}.$$

States characterized by quantum numbers  $L$  and  $S$  (associated with the eigenvalues of the appropriate operators), which arise from Eq. (1.1) after considering the residual term  $\mathcal{H}_{\text{res}}$ , are  $(2L + 1)(2S + 1)$ -times degenerate and we call them terms. They are usually labelled as  $^{2S+1}L$  and following spectroscopic notation is used for corresponding values of  $L$ :

$$\begin{array}{rcccccccc} L= & 0 & 1 & 2 & 3 & 4 & 5 & 6 \dots \\ & S & P & D & F & G & H & I \dots \end{array}$$

Assuming  $LS$  coupling, the most important relativistic correction, i. e. the spin-orbit interaction, can be introduced in the form [10]

$$\mathcal{H}_{\text{SO}} = \zeta(LS)(\mathbf{S} \cdot \mathbf{L}) \quad (1.6)$$

and added to the Hamiltonian (1.1), thus we have

$$\mathcal{H} = \mathcal{H}_0 + \mathcal{H}_{\text{res}} + \mathcal{H}_{\text{SO}}. \quad (1.7)$$

Symbol  $\zeta$  in Eq. (1.6) designates the spin-orbit coupling constant. The spin-orbit coupling further lifts the degeneracy of the terms and splits them into multiplets  $^{2S+1}L_J$ . Possible values of the total angular momentum  $J$  range from  $|L - S|$  to  $L + S$ .

In order to determine the ground state of the rare earth ion, which is crucial for magnetism, and corresponding values of  $L$ ,  $S$  and  $J$ , empirical Hund's rules can be applied [11]:

1. The lowest-lying energy level has the maximal possible value of  $S$  consistent with the Pauli exclusion principle.
2. Among the levels with the same value of  $S$ , the level with the maximal allowed value of  $L$  gives the lowest energy.
3. For the less than half-filled shell, the lowest-lying energy level has  $J = |L - S|$ . For the more than half-filled shell, the lowest-lying energy level has  $J = L + S$ .

---

\*We will consider angular momentums  $\mathbf{L}$ ,  $\mathbf{S}$  and  $\mathbf{J}$  as dimensionless, i. e. expressed in the terms of reduced Planck constant constant  $\hbar$ .

First two Hund's rule enable us to choose the ground-state term, third Hund's rule the ground-state multiplet after considering the spin-orbit coupling, i. e. corresponding to the Hamiltonian (1.7).

### 1.1.2 Paramagnetism of free ions

Eigenstates of (1.7) can be also conveniently labelled as  $\{|\alpha JM_J LS\rangle\}$ ; index  $\alpha$  further specifies the electron configuration. These states are still  $2J + 1$ -times degenerate with respect to the projection of the total angular momentum  $M_J$ . Angular momentums  $\mathbf{L}$  and  $\mathbf{S}$  are directly associated with the paramagnetic moment of the ion via relation [9]

$$\boldsymbol{\mu} = -\mu_B(\mathbf{L} + 2\mathbf{S}). \quad (1.8)$$

According to the Wigner-Eckart theorem, matrix elements of the operators with same transport properties are proportional, particularly for matrix elements of spin, orbital and total angular momentum it holds [12]

$$\langle \alpha JM_J LS | \mathbf{L} + 2\mathbf{S} | \alpha JM'_J LS \rangle = g(LSJ) \langle \alpha JM_J LS | \mathbf{J} | \alpha JM'_J LS \rangle, \quad (1.9)$$

where the constant of proportionality  $g$  is so-called Landé  $g$ -factor

$$g = 1 + \frac{J(J+1) + S(S+1) - L(L+1)}{2J(J+1)}. \quad (1.10)$$

Let us now consider an ion in the state  $|\alpha JM_J LS\rangle$  inserted into a static uniform external magnetic field  $\mathbf{H}$ . For an ion with partially filled shell, we may neglect weak diamagnetic correction, namely Larmor diamagnetism, and write the Zeeman interaction Hamiltonian in a form

$$\mathcal{H}_{\text{Zeem}} = -\boldsymbol{\mu} \cdot \mathbf{H} = \mu_B(\mathbf{L} + 2\mathbf{S}) \cdot \mathbf{H} = g\mu_B(\mathbf{J} \cdot \mathbf{H}). \quad (1.11)$$

Since Zeeman splitting produced by ordinary laboratory magnetic fields is usually much weaker than splitting caused by spin-orbit coupling, it can be taken into consideration as a consecutive perturbation which additionally lifts the  $2J + 1$ -fold degeneracy of the states  $\{|\alpha JM_J LS\rangle\}$  in  $M_J$ . Magnetization, respectively overall magnetic moment, of a paramagnetic system of ions is generally given by thermal-averaged contributions  $\mu_{\tilde{n}}$  from individual levels which follow the Boltzmann statistics

$$M_i = \frac{1}{Z} \sum_{\tilde{n}} \mu_{\tilde{n}} \exp\left(\frac{-E_{\tilde{n}}}{k_B T}\right). \quad (1.12)$$

Here  $\mu_{\tilde{n}} = -g\mu_B \langle \tilde{n} | J_i | \tilde{n} \rangle$  is the moment of the level with the energy  $E_{\tilde{n}}$ ,  $J_i$  is the projection of the total angular momentum to the direction of an applied field and  $Z$  is the partition function

$$Z = \sum_{\tilde{n}} \exp\left(\frac{-E_{\tilde{n}}}{k_B T}\right). \quad (1.13)$$

Magnetization (per unit volume) of  $N$  free ions can be then, considering perturbed Hamiltonian (1.11), expressed in a closed form[13]

$$M = \frac{N}{V} \mu_B g J B_J(x), \quad (1.14)$$

where we adopted the Brillouin function  $B_J$

$$B_J(x) = \frac{2J+1}{2J} \coth\left(\frac{(2J+1)x}{2J}\right) - \frac{1}{2J} \coth\left(\frac{x}{2J}\right) \quad (1.15)$$

with  $x = \frac{\mu_B g J H}{k_B T}$ . For  $x \ll 1$  we can obtain the Curie law for the static longitudinal paramagnetic susceptibility [9]

$$\chi_{\text{Curie}} = \frac{\partial M}{\partial H} \Big|_{H \rightarrow 0} = \frac{N}{V} (g\mu_B)^2 \frac{J(J+1)}{3k_B T} = \frac{C}{T}, \quad (1.16)$$

where  $C$  is the Curie constant. Quantity  $p = g\sqrt{J(J+1)}$ , squared in the nominator of Eq. (1.16), characterizes the paramagnetic behaviour of a system of ions and is called the effective Bohr magneton number [13]. For  $x \rightarrow \infty$ , namely in the limit of high fields and low temperatures, the Brillouin function approaches 1 and magnetization (1.14) therefore saturates at the value proportional to  $gJ$  referred to as the saturated moment (in units of  $\mu_B$ ). Values of these quantities as well as other properties of trivalent rare earth ions are listed in the Table 1.1 below.

Ion	Electron configuration	Ground state	$g$	$p$	$gJ$
Ce <sup>3+</sup>	$4f^1 5s^2 p^6$	$^2F_{5/2}$	$\frac{6}{7}$	2.54	2.14
Pr <sup>3+</sup>	$4f^2 5s^2 p^6$	$^3H_4$	$\frac{4}{5}$	3.58	3.20
Nd <sup>3+</sup>	$4f^3 5s^2 p^6$	$^4I_{9/2}$	$\frac{5}{7}$	3.62	3.27
Pm <sup>3+</sup>	$4f^4 5s^2 p^6$	$^5I_4$	$\frac{3}{5}$	2.68	2.40
Sm <sup>3+</sup>	$4f^5 5s^2 p^6$	$^6H_{5/2}$	$\frac{2}{7}$	0.85	0.71
Eu <sup>3+</sup>	$4f^6 5s^2 p^6$	$^7F_0$	0	0	0
Gd <sup>3+</sup>	$4f^7 5s^2 p^6$	$^8S_{7/2}$	2	7.94	7.0
Tb <sup>3+</sup>	$4f^8 5s^2 p^6$	$^7F_6$	$\frac{3}{2}$	9.72	9.0
Dy <sup>3+</sup>	$4f^9 5s^2 p^6$	$^6H_{15/2}$	$\frac{4}{3}$	10.65	10.0
Ho <sup>3+</sup>	$4f^{10} 5s^2 p^6$	$^5I_8$	$\frac{5}{4}$	10.61	10.0
Er <sup>3+</sup>	$4f^{11} 5s^2 p^6$	$^4I_{15/2}$	$\frac{6}{5}$	9.58	9.0
Tm <sup>3+</sup>	$4f^{12} 5s^2 p^6$	$^3H_6$	$\frac{7}{6}$	7.56	7.0
Yb <sup>3+</sup>	$4f^{13} 5s^2 p^6$	$^2F_{7/2}$	$\frac{8}{7}$	4.54	4.0

Table 1.1: Trivalent rare earth ions and their properties[14]: electron configuration, spectroscopic symbol of the ground state, Landé  $g$ -factor and  $gJ$ .

Experimental values of  $g$ ,  $p$  and  $gJ$  for intermetallic rare earth compounds usually somewhat differ from those mentioned in the table for free ions - the reason for that are in principle additional interactions emerging in solids, e. g. crystal field, hybridization with conduction electrons, Kondo effect and others, some of them will be discussed in the following.

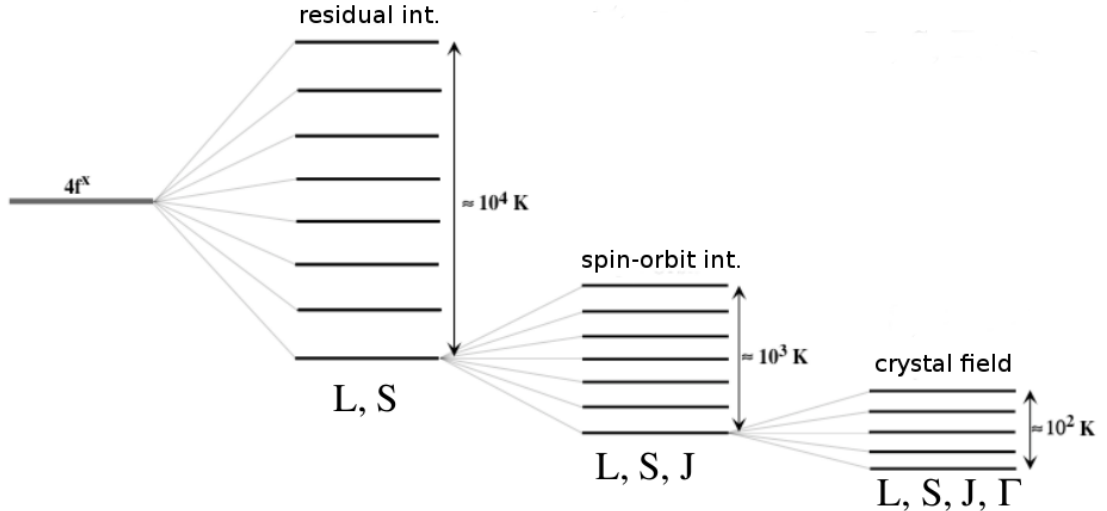


Figure 1.1: Consecutive splitting of  $4f$  energy levels due to the residual interaction, spin-orbit coupling and crystal field, its typical magnitudes and quantum numbers characterizing states. After [16].

## 1.2 Magnetism of solids

### 1.2.1 Crystal field

When an ion is embedded into a crystal, it experiences a crystal field (CF) (also crystalline electric field) which is given by the surroundings of the ion and symmetry of the ion site. Symmetry of a crystal, defined by a finite crystallographic group, is necessarily lower than full rotational symmetry of a free ion and, thus, CF effects generally lead to the splitting of the free-ion energy levels according to the group theory [15]. In contrast with ions of  $3d$  elements, the perturbation due to the CF is in the case of rare earth ions small compared to the spin-orbit splitting (which is weaker than residual interaction) and hence CF lifts the degeneracy of multiplets as illustrated in the Fig. 1.1. The degeneracy of the ions with odd number of electrons cannot be removed by the CF completely - according to the Kramers theorem energy levels of an ion in a presence of an electric field of any nature, including CF, remain at least twofold and evenly degenerate [17]. Ions with odd numbers of electrons (including e. g.  $\text{Ce}^{3+}$  and  $\text{Nd}^{3+}$ ) are therefore referred to as Kramers ions.

We will describe CF effects on the basis of a simple point-charge model as presented in [18] using the method of operator equivalents originally introduced by Stevens [19]. Although CF effects cannot be interpreted as an electrostatic interaction only [20], this model provides a qualitatively good description of the CF, since a number of energy levels and their degeneracy is determined solely by symmetry. It assumes that CF effects of crystalline environment on a single magnetic ion can be described as electrostatic interaction with point charges  $q_j$  at positions  $R_j$  with potential

$$V_{\text{CF}}(\mathbf{r}) = \sum_j \frac{q_j}{|\mathbf{R}_j - \mathbf{r}|}. \quad (1.17)$$

The further step is to express the electrostatic potential (1.17) in terms of spher-

ical harmonics employing the so-called Laplace expansion [21]

$$\frac{1}{|\mathbf{R}_j - \mathbf{r}|} = \sum_n \frac{r^n}{R_j^{n+1}} \frac{4\pi}{2n+1} \sum_{m=-n}^n (-1)^m Y_n^{-m}(\theta_j, \phi_j) Y_n^m(\theta, \phi) \quad (1.18)$$

and subsequently switch from complex spherical harmonics  $Y_n^m$  to their real counterparts - tesseral harmonics  $Z_n^m$  which are defined and listed e. g. in [22]. Tesseral harmonics  $Z_n^m$  are already closely related to Stevens operators  $O_n^m$ , which can be obtained by substitution of coordinates  $x, y$  and  $z$  with (properly symmetrized) components of total angular momentum  $J_x, J_y$  and  $J_z$ , respectively, as illustrated below on the example of tesseral harmonic  $Z_2^0$  and operator  $O_2^0$

$$Z_2^0 \propto 3z^2 - r^2$$

$$\sum_j (3z_j^2 - r_j^2) \propto \langle r^2 \rangle [3J_z^2 - J(J+1)] = \langle r^2 \rangle O_2^0.$$

A complete list of other Stevens operators  $O_n^m$  can be found in [18] or [23]. Finally, we can thereby get the CF Hamiltonian  $\mathcal{H}_{\text{CF}}$  from Eq. (1.17) in a well-known form:

$$\mathcal{H}_{\text{CF}} = \sum_{n,m} B_n^m O_n^m = \sum_{n,m} A_n^m \langle r^n \rangle \theta_n O_n^m. \quad (1.19)$$

Here  $B_n^m$ , respectively  $A_n^m$  are crystal-field parameters, multiplicative factors  $\theta_n$  ( $\theta_2 \equiv \alpha_J, \theta_4 \equiv \beta_J, \theta_6 \equiv \gamma_J$ ) are so-called Stevens coefficients which are tabulated for each RE ion [18]. Matrix elements of the CF Hamiltonian (1.19) can be then thanks to the Wigner-Eckart theorem evaluated within the basis of functions  $\{|\alpha JM_J LS\rangle\}$  without the need of going back to the Cartesian Hamiltonian (1.17). In practice, summation in Eq. (1.19) does not run over all possible indices  $n, m$  but due to the symmetry is restricted to only several relevant independent terms yielding non-zero matrix elements, especially [24]:

- All terms with  $n > 2l$ , where  $l$  is the orbital quantum number of a single electron in the incompletely occupied shell, vanishes.
- Terms with  $n > 2J$  do not contribute.
- The term with  $n = m = 0$  is spherically symmetric and hence it does not cause splitting.
- All odd- $n$  terms in Eq. (1.19) disappear in consequence of orthogonality of spherical harmonics.
- Having the coordinate axes properly chosen with respect to a crystal, it holds due to the local point symmetry of the magnetic ion site:
  - If the  $z$ -axis is a  $p$ -fold axis of symmetry, terms do not apply unless  $m$  is an integer multiple of  $p$ .
  - If the  $y$ -axis is a twofold axis of symmetry, terms with  $n + m$  odd vanish.

These rules practically reduce a number of applicable terms in Eq. (1.19) to some of those with  $n = 2, 4, 6$ . Furthermore, relations among Stevens operators of the same order apply for particular CF symmetries. Consequently, there are only several independent CF parameters for particular crystal systems depending on a crystallographic point group of the magnetic ion site as listed in the Table 1.2.

Table 1.2: Independent CF parameters for particular crystal systems and point groups. Symbol \* designates complex CF parameters [25].

crystal system	point groups (Schoenflies)	point groups (Hermann-Mauguin)	CF parameters
cubic	$T T_d T_h O O_h$	23 $\bar{4}3m$ $m\bar{3}$ 432 $m\bar{3}m$	$B_4^0 B_6^0$
tetragonal	$D_{4h} D_{2d} C_{4v} D_4$	4/ $mmm$ 42m 4mm 422	$B_2^0 B_4^0 B_4^4 B_6^4 B_6^0$
tetragonal	$C_4 S_4 C_{4h}$	4 $\bar{4}$ 4/ $m$	$B_2^0 B_4^0 B_4^4 B_6^{4*} B_6^0$
hexagonal	$C_{3h} D_{3h} C_{6v} D_6 C_6 D_{6h} C_{6h}$	$\bar{6}$ $\bar{6}m2$ 6mm 622 6 6/ $mmm$ 6/ $m$	$B_2^0 B_4^0 B_6^0 B_6^6$
trigonal	$C_{3v} D_{3d} D_3$	3m $\bar{3}m$ 32	$B_2^0 B_4^0 B_4^3 B_6^3 B_6^6$
trigonal	$C_3 S_6$	3 $\bar{3}$	$B_2^0 B_4^0 B_4^3 B_6^3 B_6^{6*}$
orthorhombic	$D_2 C_{2v} D_{2h}$	222 2mm $mmm$	$B_2^0 B_2^2 B_4^0 B_4^2 B_4^4 B_6^0 B_6^2 B_6^4 B_6^6$
monoclinic	$C_2 C_{2h}$	2 2/ $m$	$B_2^0 B_2^2 B_4^0 B_4^2 B_4^{4*} B_6^0 B_6^2 B_6^4 B_6^{6*}$
triclinic	$C_1 C_i$	1 $\bar{1}$	(15 parameters)

As an illustrative example of (1.19) we present the CF Hamiltonian of the  $Ce^{3+}$  ion in the tetragonal environment<sup>†</sup>. In general, Hamiltonian of the tetragonal CF consists of five terms:

$$\mathcal{H}_{CF}^{tetr} = B_2^0 \hat{O}_2^0 + B_4^0 O_4^0 + B_4^4 O_4^4 + B_6^0 O_6^0 + B_6^4 O_6^4. \quad (1.20)$$

But since  $J = 5/2$  for  $Ce^{3+}$  ion, the higher-order terms with  $n = 6$  do not contribute according to the previously mentioned rules and by evaluating the Eq. (1.20) in the basis  $\{|\alpha J M_J L S\rangle\}$  we get (here states are designated by  $|M_J\rangle$ )

$$\mathcal{H}_{CF}^{tetr}(Ce^{3+}) = \begin{matrix} \langle 5/2| \\ \langle 3/2| \\ \langle 1/2| \\ \langle -1/2| \\ \langle -3/2| \\ \langle -5/2| \end{matrix} \begin{pmatrix} |5/2\rangle & |3/2\rangle & |1/2\rangle & |-1/2\rangle & |-3/2\rangle & |-5/2\rangle \\ A & 0 & 0 & 0 & 12\sqrt{5}B_4^4 & 0 \\ 0 & B & 0 & 0 & 0 & 12\sqrt{5}B_4^4 \\ 0 & 0 & C & 0 & 0 & 0 \\ 0 & 0 & 0 & C & 0 & 0 \\ 12\sqrt{5}B_4^4 & 0 & 0 & 0 & B & 0 \\ 0 & 12\sqrt{5}B_4^4 & 0 & 0 & 0 & A \end{pmatrix} \quad (1.21)$$

where

$$\begin{aligned} A &= 10B_2^0 + 60B_4^0 \\ B &= -2B_2^0 - 180B_4^0 \\ C &= 120B_4^0 - 8B_2^0. \end{aligned} \quad (1.22)$$

Energies and corresponding wave functions can be then obtained by solving a standard eigenvalues problem. In case of  $Ce^{3+}$  in the tetragonal CF, the procedure

<sup>†</sup>Initially, we intended to present the Hamiltonian of the  $Nd^{3+}$  in the tetragonal CF here which would be more meaningful with respect to the topic of the thesis. But since its matrix is much larger ( $10 \times 10$ ) and involves sixth-order terms we decided on  $Ce^{3+}$  for better lucidity, similarly as in [26].

leads to three Kramers doublets. Using values of the CF parameters for e. g. the tetragonal compound CePd<sub>5</sub>Al<sub>2</sub> published by Nakano et. al. [27] ( $B_2^0 = -12$  K,  $B_4^0 = -0.1$  K and  $B_4^2 = 1.9$  K) we will explicitly have:

$$\begin{aligned} |\Gamma_7^\pm\rangle &= \mp 0.963 |\pm 5/2\rangle \pm 0.269 |\mp 3/2\rangle \leftrightarrow E_{\Gamma_7} = 0 \text{ K} \\ |\Gamma_8^\pm\rangle &= 0.269 |\pm 5/2\rangle + 0.963 |\mp 3/2\rangle \leftrightarrow E_{\Gamma_8} = 197 \text{ K} \\ |\Gamma_9^\pm\rangle &= |\pm 1/2\rangle \leftrightarrow E_{\Gamma_9} = 224 \text{ K}. \end{aligned} \quad (1.23)$$

As we can see individual Kramers doublets are composed of linear combinations of wave functions with the opposite projection of the total angular momentum.

In the following section we will inspect effects of the CF on magnetic properties.

### 1.2.2 Influence of the crystal field on magnetic properties

Since the CF produces an energy level scheme different from that of a free ion and affects a charge density distribution upon the magnetic ion site, it is crucial for magnetic properties influencing fundamentally the magnetocrystalline anisotropy. The Hamiltonian of the CF system under magnetic field may be written as follows:

$$\mathcal{H} = \mathcal{H}_{\text{CF}} + g\mu_B J_i H, \quad (1.24)$$

where  $J_i$  is the component of the total angular momentum in the direction of the field  $H$ . Field dependence of magnetization can be then calculated with the help of formula (1.12) considering Hamiltonian (1.24) and its eigenstates. Zeeman term in Eq. (1.24) causes rather small splitting compared to the CF (typically in order of 1-10 K for rare-earth systems in common laboratory magnetic fields) allowing us employing perturbation expansion in order to find an expression for susceptibility. The energy up to second-order perturbation will be

$$E_n(H) = E_n + g\mu_B H \langle n | J_i | n \rangle + (g\mu_B)^2 H^2 \sum_{m \neq n} \frac{|\langle m | J_i | n \rangle|^2}{E_m - E_n}. \quad (1.25)$$

Using partition function (1.13), its relation to the free energy  $F = -k_B T \ln Z$  and thermodynamic definition of susceptibility  $\chi = \frac{\partial M}{\partial H} \Big|_{H \rightarrow 0} \propto -\frac{\partial^2 F}{\partial H^2}$ , we can obtain after some rather tedious derivation (more thoroughly e. g. in [26]) an appropriate relation for the paramagnetic CF susceptibility:

$$\begin{aligned} \chi_{\text{CF}}^i &= \frac{N (g_J \mu_B)^2}{V Z} \left[ \frac{\sum_n |\langle n | J_i | n \rangle|^2}{k_B T} \exp\left(\frac{-E_n}{k_B T}\right) \right. \\ &\quad \left. + \sum_{\substack{n,m \\ n \neq m}} |\langle m | J_i | n \rangle|^2 \frac{\exp\left(\frac{-E_n}{k_B T}\right) - \exp\left(\frac{-E_m}{k_B T}\right)}{E_m - E_n} \right]. \end{aligned} \quad (1.26)$$

States  $|n\rangle$  and energies  $E_n$  are eigenstates and eigenvalues of the CF Hamiltonian. First term in (1.26) containing diagonal matrix elements of the total angular

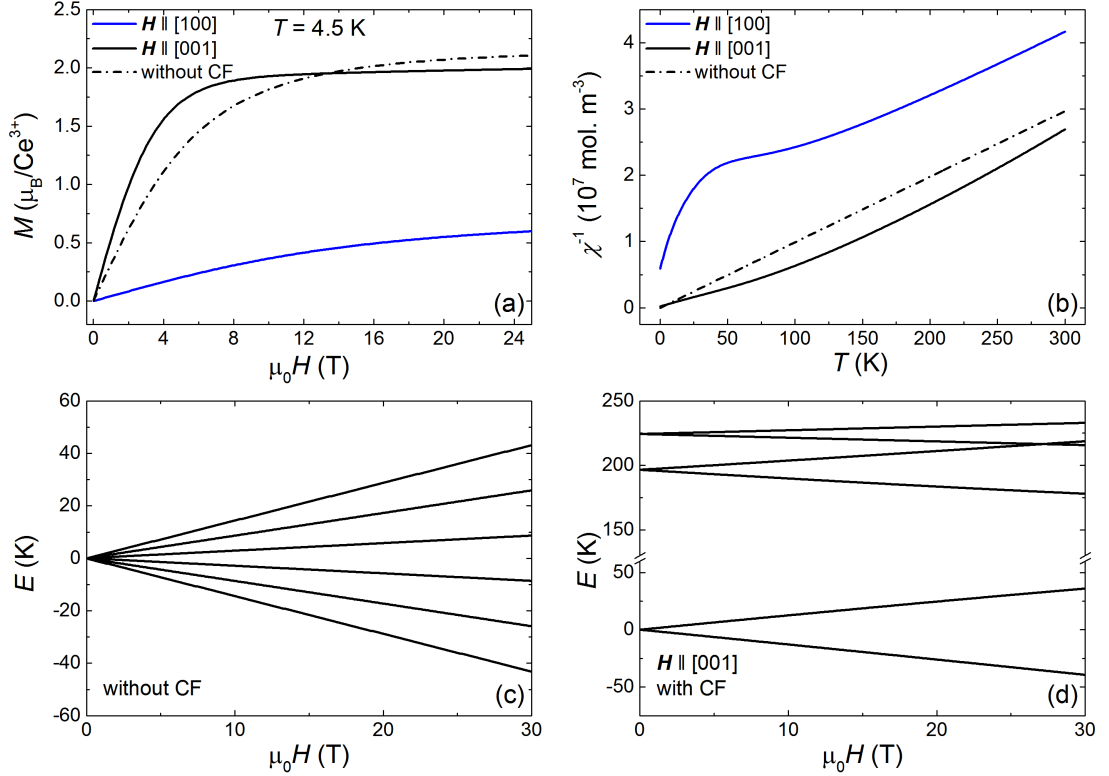


Figure 1.2: Effects of the CF on magnetic properties in the tetragonal  $\text{CePd}_5\text{Al}_2$ : Field dependence of magnetization (a) using (1.12), susceptibility (b) according relations (1.26) and (1.31), splitting of the energy levels under magnetic field without (c) and with the CF (d). Parameters used for calculation of the curves are taken from [27]:

$$\begin{aligned}
 B_2^0 &= -12 \text{ K}, B_4^0 = -0.1 \text{ K}, B_6^0 = 1.9 \text{ K}, \\
 \lambda^{[100]} &= -5.8 \times 10^6 \text{ mol m}^{-3}; \lambda^{[001]} = -2.0 \times 10^5 \text{ mol m}^{-3}; \\
 \chi_0^{[100]} &= -6.3 \times 10^{-10} \text{ m}^3 \text{ mol}^{-1}, \chi_0^{[001]} = -5.0 \times 10^{-9} \text{ m}^3 \text{ mol}^{-1}.
 \end{aligned}$$

momentum tends to diverge as  $\frac{1}{T}$  at low temperatures and it is the Curie term already mentioned in the Section 1.1.2. The latter term incorporating matrix elements between different CF states becomes constant at zero temperature and it is referred as the Van Vleck paramagnetic contribution [10].

To demonstrate effects of the CF on magnetic properties we again chose the tetragonal  $\text{CePd}_5\text{Al}_2$  as an example and we used wave functions and energies (1.23) to calculate field dependence of magnetization, susceptibility and splitting of the energy levels under magnetic field with and without CF (Fig. 1.2).

### 1.2.3 Exchange interactions

Exchange interactions originate from the antisymmetry of the fermionic wave function and are principally responsible for the phenomenon of long-range magnetic ordering in solids.

We distinguish direct exchange which applies in case of ions with a significant overlap of charge distributions, primarily in  $3d$  electron systems, and indirect exchange which occurs in  $4f$  compounds [28]. Indirect exchange interaction can be mediated either by non-magnetic ions or by itinerant electrons. The former type

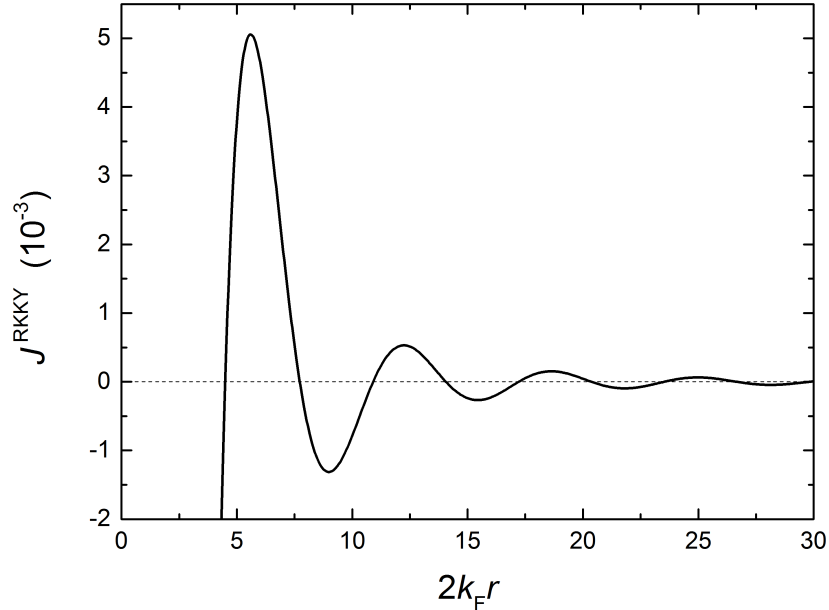


Figure 1.3: Oscillatory part of the RKKY exchange parameter (1.28) as a function of  $2k_{\text{F}}r$ .

of indirect exchange coupling is observed in insulators and it is also called superexchange, whereas the latter dominates in  $4f$  metals and intermetallic compounds and it is known as the RKKY interaction (after Ruderman, Kittel, Kasuya, and Yosida).

The common description of exchange interactions is based on the isotropic Heisenberg Hamiltonian where coupling between two  $S$ -state ions with spins  $\mathbf{S}_i$  and  $\mathbf{S}_j$  takes form [8]

$$\mathcal{H}_{ij} = -\mathcal{J}_{ij} \mathbf{S}_i \cdot \mathbf{S}_j. \quad (1.27)$$

$\mathcal{J}_{ij}$  represents exchange parameter. The exchange parameter of the RKKY type  $\mathcal{J}^{\text{RKKY}}$  takes a form of an oscillatory function (see Fig. 1.3) varying as [29]

$$\mathcal{J}^{\text{RKKY}} \propto \frac{x \cos(x) - \sin(x)}{x^4} \quad (1.28)$$

where  $x = 2k_{\text{F}}r$  and  $k_{\text{F}}$  is the Fermi  $k$ -vector. Preferable type of magnetic ordering then depends on the sign of  $\mathcal{J}^{\text{RKKY}}$  on the site of the neighbouring magnetic ion exhibiting ferromagnetism characterized by parallel moments when the sign is positive, (simple) antiferromagnetism with the antiparallel alignment of the moments for the negative sign or more complicated types of magnetic ordering (e. g. helical structures) for the oscillating  $\mathcal{J}^{\text{RKKY}}$ .

Usual treatment of the exchange interactions further employs mean field approximation which enables expressing exchange interactions effectively in terms of a single-ion Hamiltonian

$$\mathcal{H}_{\text{ex}} = -\boldsymbol{\mu} \cdot \mathbf{H}_{\text{m}} \quad (1.29)$$

and the molecular field  $\mathbf{H}_{\text{m}}$  which is proportional to magnetization. Altogether with the foregoing, we will have Hamiltonian of the same type as (1.24):

$$\mathcal{H} = \mathcal{H}_{\text{CF}} + g\mu_{\text{B}}J_i(H + \lambda_i M_i), \quad (1.30)$$

where effective field  $H_{\text{eff}} = H + \lambda_i M_i$  involves the influence of both external magnetic field and exchange interactions represented by the molecular field constant  $\lambda_i$ . Eq. (1.30) sufficiently well describes paramagnetic behaviour as well as a variety of other properties of most rare-earth compounds [8].

For the overall susceptibility we may then write a relation

$$\chi_i = \frac{1}{\frac{1}{\chi_{\text{CF}}^i} - \lambda_i} + \chi_0^i, \quad (1.31)$$

where we, besides molecular field constant  $\lambda_i$  which shifts the reciprocal CF susceptibility  $1/\chi_{\text{CF}}^i$ , also added the temperature-independent term  $\chi_0^i$  representing Pauli paramagnetic susceptibility of conduction electrons. However, Pauli contribution of conduction electrons is usually by several orders of magnitude weaker than paramagnetic contribution of magnetic ions and thus often negligible [12].

CF susceptibility  $\chi_{\text{CF}}^i$  in the isotropic case, i. e. without the influence of the CF, reduces simply to  $\chi_{\text{Curie}}$  (1.16) and we may obtain from (1.31) Curie-Weiss law for paramagnetic susceptibility<sup>‡</sup>

$$\chi^{\text{CW}} = \frac{C}{T - \Theta_p}, \quad (1.32)$$

where  $\Theta_p$  is the paramagnetic Curie temperature. Within assumptions of the mean field theory, this temperature should correspond to the critical temperature  $T_C$  of a ferromagnet (respectively Néel temperature of an antiferromagnet) at which the spontaneous ordering occurs and which can be in this model related to the molecular field parameter  $\lambda$  and exchange parameter  $\mathcal{J}$ :

$$T_C = \frac{J(J+1)\mathcal{J}}{3k_B} = \frac{N}{V} \frac{(g\mu_B)^2}{3k_B} J(J+1)\lambda. \quad (1.33)$$

Nevertheless, experimental values of  $\Theta_p$  often more or less differs from  $T_C$  also due to the CF. Taken vice versa, experimental Curie paramagnetic temperatures may serve for preliminary analysis of the CF and can be used, considering isotropic Heisenberg exchange, for estimation of the parameter  $B_2^0$  - leading CF parameter of anisotropic uniaxial (i. e. tetragonal and hexagonal) materials [10]:

$$k_B \Theta_{\parallel} = \frac{1}{3} J(J+1)\mathcal{J} - \frac{4}{5} \left(J - \frac{1}{2}\right) \left(J + \frac{3}{2}\right) B_2^0 \quad (1.34)$$

$$k_B \Theta_{\perp} = \frac{1}{3} J(J+1)\mathcal{J} + \frac{2}{5} \left(J - \frac{1}{2}\right) \left(J + \frac{3}{2}\right) B_2^0, \quad (1.35)$$

where  $\Theta_{\parallel}$  ( $\Theta_{\perp}$ ) are determined by fitting high-temperature part of susceptibilities to the Curie-Weiss law when field is applied parallel, respectively perpendicular to the principal axis.

### 1.3 Heat capacity of solids

Heat capacity is the heat required to change the temperature of a substance by 1 K. Although it is one of the most fundamental physical quantities, it may

---

<sup>‡</sup>We have dropped the Pauli susceptibility  $\chi_0$  here.

provide useful information about internal degrees of freedom in matter which are responsible for the capability of storing energy supplied as heat. It is thus closely connected to the entropy of a system and we may write defining relation in the following manner:

$$C_{V,p} = \left( \frac{\partial Q}{\partial T} \right)_{V,p} = T \left( \frac{\partial S}{\partial T} \right)_{V,p}, \quad (1.36)$$

where  $C_V$  designates heat capacity at constant volume (more fundamental quantity for calculations) and  $C_p$  heat capacity at constant pressure (quantity which is usually more easily experimentally accessible). We often consider heat capacity per unit amount of a material, namely specific heat. Total specific heat of a solid typically consists of several additive contributions

$$C_{\text{tot}} = C_{\text{ph}} + C_{\text{el}} + C_{\text{mag}} + C_{\text{etc}}. \quad (1.37)$$

$C_{\text{ph}}$  symbolizes the phonon specific heat,  $C_{\text{el}}$  is the specific heat of conduction electrons,  $C_{\text{mag}}$  comprises contributions of magnetic origin and  $C_{\text{etc}}$  involves possible other contributions (e. g. nuclear specific heat).

Phonon specific heat has its origin in lattice vibrations and typically represents the largest part of the specific heat at higher temperatures. For its description we use two models based on the harmonic approximation - the Einstein model and the Debye model.

The Einstein model assumes an ensemble of atoms oscillating at the same frequency  $\omega_E$  leading to the relation (for one phonon mode) [13]:

$$C_E = k_B N_A \left( \frac{\Theta_E}{T} \right)^2 \frac{\exp(\frac{\Theta_E}{T})}{\left[ \exp(\frac{\Theta_E}{T}) - 1 \right]^2}, \quad (1.38)$$

where  $\Theta_E = \frac{\hbar\omega_E}{k_B}$  is the Einstein temperature and  $N_A$  Avogadro constant. This model is convenient for approximation of optical phonon branches.

Debye model can be utilized for description of acoustic phonon branches. It considers linear dispersion  $\omega = ck$  and permits phonon frequencies up to Debye frequency  $\omega_D = \frac{k_B\Theta_D}{\hbar}$  with the resulting specific heat per one phonon branch as follows:

$$C_D = 3k_B N_A \left( \frac{T}{\Theta_D} \right)^3 \int_0^{\frac{\Theta_D}{T}} \frac{x^4 \exp(x)}{\left[ \exp(x) - 1 \right]^2} dx. \quad (1.39)$$

Findings of the Sommerfeld theory of metals provide an expression for specific heat of conduction electrons depending linearly on temperature:

$$C_{\text{el}} = \gamma T \quad (1.40)$$

This contribution becomes relatively more significant at low temperatures. Altogether with the lattice contribution given by expansion of (1.39) for  $T \ll \Theta_D$  the widely used equation for the low-temperature specific heat therefore reads [12]

$$C_{\text{ph}} + C_{\text{el}} = \gamma T + \beta T^3, \quad (1.41)$$

where  $\beta = \frac{12}{5}\pi^4 k_B N_A \left( \frac{1}{\Theta_D} \right)^3$  considering all three acoustic branches.

An important task from the viewpoint of magnetism is proper separation of the magnetic term  $C_{\text{mag}}$  from (1.37) and its further examination. The analysis comprises two parts: In the ordered state, magnetic excitations and critical phenomena at the vicinity of phase transition contribute to the specific heat. The spin wave theory suggests that specific heat ascribed to magnetic excitations depends on their dimensionality  $d$ , type of ordering and possible gap  $\Delta$  in the magnon spectrum, summarizing all that we will have [30]

$$C_M = aT^{\frac{d}{m}} \exp(-\Delta/T), \quad (1.42)$$

where  $a$  is a parameter reflecting spin wave stiffness and  $m = 2$  for ferromagnetic, respectively  $m = 1$  for antiferromagnetic magnons. Moreover, there is a contribution spread well in the paramagnetic region - Schottky specific heat is connected to the entropy change as the excited CF levels are occupied and it is given as follows:

$$C_{\text{Schottky}} = k_B N_A \left[ \frac{\sum_n \frac{E_n^2}{k_B^2 T^2} \exp\left(\frac{-E_n}{k_B T}\right)}{Z} - \frac{\left(\sum_n \frac{E_n}{k_B T} \exp\left(\frac{-E_n}{k_B T}\right)\right)^2}{Z^2} \right]. \quad (1.43)$$

Maximum change of magnetic entropy between fully ordered and completely disordered state of a system consisting of  $2J + 1$  levels is then [31]

$$S_{\text{mag}} = R \ln(2J + 1). \quad (1.44)$$

# 2. Experimental techniques

## 2.1 Magnetic measurements

Magnetic measurements were performed on the Magnetic Property Measurement System (MPMS) XL manufactured by the company Quantum Design\*[32]. The device is equipped with the sensitive SQUID detection system and 7 T superconducting magnet and can operate in the temperature range 2 - 400 K. It utilizes induction technique - as a sample is moved through the pick-up coils, it produces variation of the magnetic flux and thus induces voltage on coils which is proportional to the sample's magnetic moment.

The magnetization at temperatures below 2 K was measured using cross-shaped Hall effect probes. The sample was placed on the Hall cross on the  $a$ - $c$  plane with the edge in the middle of the cross and magnetic field applied along the tetragonal  $c$ -axis (and in plane of the Hall cross). With this setup the Hall sensor is sensitive to the stray field proportional to the  $c$ -axis magnetization. Absolute values of magnetization were calculated by comparison with the MPMS data using measurement at 2 K as a reference.

## 2.2 Heat capacity

Heat capacity was measured using the Physical Property Measurement System (PPMS) 9 T, respectively 14 T equipped with Helium 3 refrigerator for achieving low temperatures (down to  $\approx 0.4$  K) and supplied also by Quantum Design. We have employed two different methods:

Relaxation technique involves monitoring of the sample's response to a constant-power heating pulse and subsequent exponential relaxation down to the temperature of the thermal bath as the heating is turned off. Heat capacity is then determined from the relaxation constant  $\tau$  during cooling according to the relation [33]

$$T_{\text{sample}}(t) - T_{\text{bath}} = \Delta T e^{-t/\tau}, \quad (2.1)$$

respectively heating, when the temperature difference between a sample and the bath follows  $\propto 1 - e^{-t/\tau}$ . The temperature rise  $\Delta T$  produced by the heater should be considerably small within this method (typically in order of  $\sim 1\%$  of  $T_{\text{bath}}$  [34]) to assure that heat capacity does not change rapidly and might be considered as constant. With this assumption, the method is not convenient for measurement of the heat capacity in the proximity of sharp features as e. g. first-order phase transitions [35].

Dual-slope method typically uses large temperature rises (i. e. in order of Kelvins). Temperature dependence of the sample during heating  $T_{\text{h}}(t)$  and cooling  $T_{\text{c}}(t)$  is recorded and heat capacity of the sample is evaluated directly from heating and cooling rates as [36]:

$$C(T) \propto \left( \frac{\partial T_{\text{h}}}{\partial t} - \frac{\partial T_{\text{c}}}{\partial t} \right)^{-1}. \quad (2.2)$$

---

\*Quantum Design homepage: <http://www.qdusa.com/>

In contrast with the relaxation measurement, the method should avoid of smearing specific-heat anomalies associated to the phase transitions [34].

## 2.3 Neutron scattering

Unique characteristics of neutrons - possessing of a magnetic moment due to the spin and electrical neutrality together with long penetration depths in most materials predetermines their broad applications in studies of structure and dynamics of matter. This makes neutron scattering a robust technique in modern condensed matter research. We would like to mention two neutron scattering methods, namely neutron diffraction and inelastic neutron scattering.

### 2.3.1 Neutron diffraction

Thermal neutrons commonly interact with a solid in a twofold manner: Short range forces in nuclei of atoms give rise to nuclear scattering, whereas dipolar interactions with magnetic moments of unpaired electrons cause magnetic scattering. These two contributions to neutron scattering can be usually considered separately. In crystals, we can conveniently apply formalism of scattering theory taking advantage of their periodicity. This introduces i. a. an important term of structure factors - intensities measured in the diffraction experiment are then generally proportional to their squared modulus. Structure factor for neutron nuclear scattering  $F_N^{hkl}$  might be obtained as [37]:

$$F_N^{hkl} = \sum_j b_j^c e^{-i\mathbf{Q}\cdot\mathbf{r}_j} e^{-W_j}. \quad (2.3)$$

Summation runs over atoms in the unit cell at positions  $\mathbf{r}_j$ ,  $b_j^c$  are their coherent scattering lengths,  $\mathbf{Q}$  is a momentum transfer and  $W_j$  represents the temperature factor. From  $F_N^{hkl}$  we can retrieve essentially similar information about crystal structure as from X-ray diffraction - positions of the peaks in diffraction patterns are given by the Bragg's law and correspond to the distances of crystal planes with Miller indices  $hkl$ . The difference between the two methods lies in scattering-angle independent nuclear scattering lengths  $b_j^c$  (in contrast with varying X-ray form factors) and comparatively higher sensitivity of neutrons to light elements.

The importance of neutrons consists in determining of magnetic structures. These are usually described in terms of propagation vectors, also called  $\mathbf{k}$ -vectors. For magnetic structure factor we can use the following formula, summing over moments within the unit cell [38]:

$$\mathbf{F}_M \propto \sum_j f_j(\mathbf{Q}) \mathbf{m}_j^{\mathbf{k}} e^{-i\mathbf{Q}\cdot\mathbf{r}_j} e^{-W_j}, \quad (2.4)$$

where  $f_j$  is a magnetic form factor and  $\mathbf{m}_j^{\mathbf{k}}$  component of the moment associated with the propagation vector  $\mathbf{k}$  (also the basis vector) and related to the physical magnetic moment  $\mathbf{m}_j$  of the  $j$ -th atom in a unit cell by Fourier expansion:

$$\mathbf{m}_j = \sum_{\{\mathbf{k}\}} \mathbf{m}_j^{\mathbf{k}} e^{-i\mathbf{k}\cdot\mathbf{T}}, \quad (2.5)$$

where  $\mathbf{T}$  is the lattice translational vector.

## Instrument description

The neutron diffraction experiment was carried out at the instrument E6 at the Helmholtz Centre Berlin. E6 (see Fig. 2.1) is a focusing diffractometer optimized for the neutron wavelength  $2.4\text{\AA}$  and covering scattering angles from  $5^\circ$  to  $140^\circ$  [39, 40]. The device allows experiments on both single crystalline and powdered samples. It is equipped with a vertically and horizontally bent monochromator and a position sensitive detector. As for collimation, the instrument offers two options: The steady Soller type collimator provides better maximal possible resolution at the cost of relatively low neutron flux, so measurement requires longer time. The adjustable fan collimator can change inclination of its blades during angular scan delivering higher flux and together with the monochromator it enables optimal performance at medium resolution [41].

Various different sample environments can be installed on the diffractometer to perform experiments under required conditions. In order to deliver low temperatures down to  $0.4\text{ K}$ , we used Oxford Instruments Variox cryostat during our measurement.

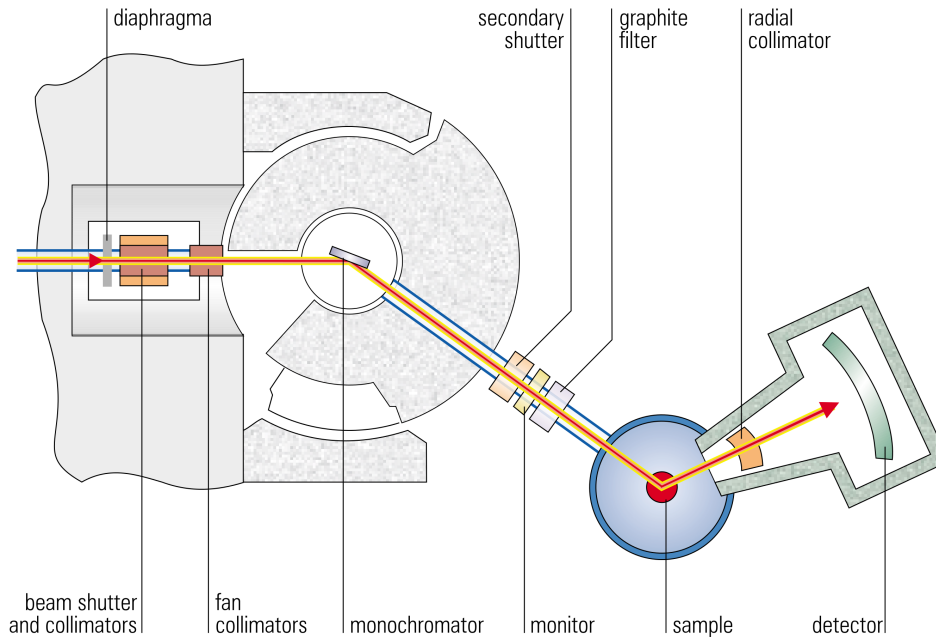


Figure 2.1: Schematic view of the E6 diffractometer. Taken from [42].

### 2.3.2 Inelastic neutron scattering

Inelastic neutron scattering (INS) is a powerful tool for examination of excitations in condensed matter. One of its numerous possible applications is using it for the direct investigation of CF levels in crystals. In such case, the following formula for a double differential cross section might be employed assuming the dipole

approximation and an unpolarized beam of neutrons [25, 43]:

$$\begin{aligned} \frac{d^2\sigma}{d\Omega dE} &= N \frac{k_f}{k_i} (\gamma r_0)^2 e^{-2W} \left[ \frac{1}{2} g f(\mathbf{Q}) \right]^2 \\ &\times \sum_{i,j} p_i |\langle \Gamma_i | \mathbf{J}_\perp | \Gamma_j \rangle|^2 \delta(\hbar\omega - E_i + E_j) = \frac{k_f}{k_i} S(\mathbf{Q}, E). \end{aligned} \quad (2.6)$$

Here constants  $N$ ,  $\gamma$  and  $r_0$  denote a number of scattering centres (ions), the neutron gyromagnetic ratio and the classical electron radius, respectively,  $k_f$  and  $k_i$  represent the final and initial neutron wavevector. Information about the CF is included in the sum: Magnitudes of the CF transition intensities observed in the INS spectrum are given by matrix elements of the operator  $\mathbf{J}_\perp$  between CF states  $|\Gamma_i\rangle$  and  $|\Gamma_j\rangle$  and by Boltzmann probabilities  $p_i$ , their positions correspond to the energy differences between CF levels. Quantity  $\hbar\omega$  is the change of the neutron energy (energy transfer) and function  $S(\mathbf{Q}, E)$  on the rightmost side of (2.6) is the so-called scattering function.

CF excitations might be often conveniently studied with a polycrystalline sample. In such case, matrix elements of the operator  $\mathbf{J}_\perp$  in (2.6) (projection of the total angular momentum  $\mathbf{J}$  to the direction perpendicular to the scattering vector  $\mathbf{Q}$ ) take the form of the polycrystalline average [44]:

$$\langle \Gamma_i | \mathbf{J}_\perp | \Gamma_j \rangle^2 = \frac{1}{3} \left( \langle \Gamma_i | J_+ | \Gamma_j \rangle^2 + \langle \Gamma_i | J_- | \Gamma_j \rangle^2 + 2 \langle \Gamma_i | J_z | \Gamma_j \rangle^2 \right). \quad (2.7)$$

In practice, CF linewidths broaden due to relaxation processes in a material and the delta function in (2.6) passes into Lorentzian. However, the data collected in the experiment are above that always convoluted with the instrument resolution function which is in case of the time-of-flight spectrometer discussed in the following paragraph nearly Gaussian [45].

### Instrument description and the time-of-flight technique

The inelastic neutron scattering experiment was performed at the IN4C instrument [46] at the ILL Grenoble. IN4C (shown in Fig. 2.2) is the indirect geometry high-flux time-of-flight spectrometer. It operates in the thermal neutron energy range ( $\sim 10$ -100 meV) and offers several possible monochromators delivering different neutron wavelengths. The bank of  $^3\text{He}$  tube detectors (complemented by the  $^3\text{He}$  multidetector) covers scattering angles of up to  $120^\circ$ .

The experiment at the instrument proceeds as follows: The polychromatic neutron beam is firstly partially monochromatised by the two counter-rotating disc choppers. This is further accomplished by the monochromator, so the energy of the incoming neutrons is well-defined. Then the neutrons pass through the Fermi chopper which is essentially a rotating collimator producing short pulses of the monochromatic neutron beam. For each packet of neutrons the time of flight is measured, which is defined as the duration between leaving the Fermi chopper and recording a neutron on a detector. Since the neutron beam is on this flightpath of a known length subject of scattering on the sample (both elastic and inelastic), the differences between the time of flight of detected neutrons and the time of flight expected for the incident ones directly bear information about energies of excitations in the sample. Detecting neutrons in the whole range

of scattering angles then allows to reconstruct the scattering function  $S(\mathbf{Q}, E)$  completely.

Further details about the instrument, its technical possibilities, e. g. eventual choices of monochromators and more about its operation can be found in ref. [46] (especially under the bookmark "Characteristics") or in the article [47].

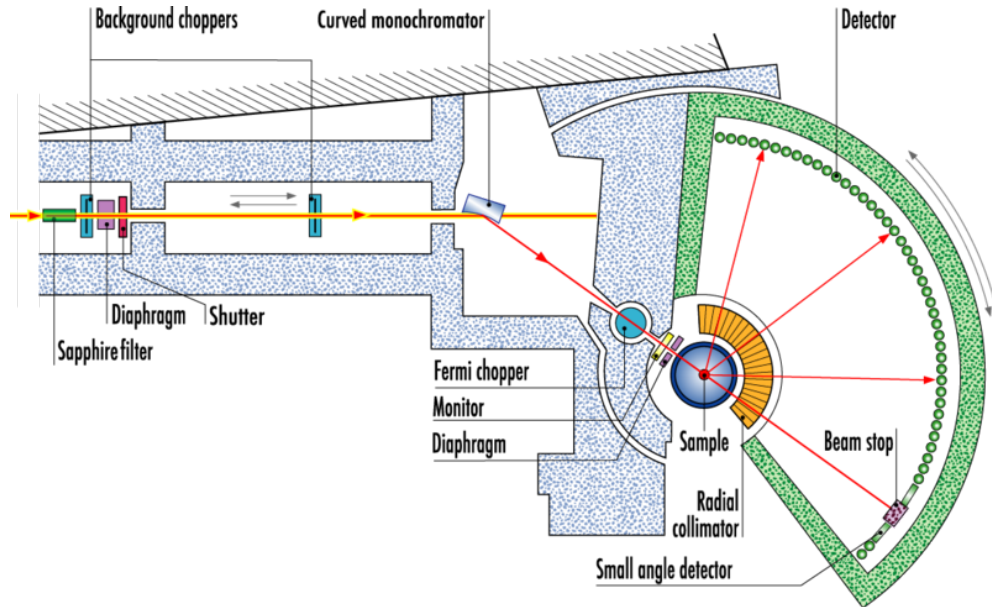


Figure 2.2: Schematic view of the IN4C time-of-flight spectrometer. The figure was taken from [46].

# 3. Previous results

## 3.1 Related tetragonal compounds

$RPd_5Al_2$  compounds belong to a large family of structurally related tetragonal intermetallics which involves among others  $RTX_5$  and  $R_2TX_8$  compounds ( $R$  is a rare earth element or actinide,  $T$  represents a transition metal and  $X$  a  $p$ -metal), their structures are presented in Fig. 3.1. Several of these materials from  $RTX_5$  and  $R_2TX_8$  series, in particular cerium-based, are archetypal heavy-fermion systems with complicated behaviour, exhibit phenomena as quantum criticality or the Kondo effect and were intensively studied due to the relationship between magnetism and an unconventional superconductivity which is here seemingly mediated by magnetic fluctuations and it is thus also closely connected to properties of  $f$ -electrons [1–3]. On the other hand, magnetic properties of their non-Kondo isostructural rare-earth analogues are mainly driven by RKKY and CF interactions only and their investigation is therefore crucial for better understanding of magnetism in these compounds. Hence, since early 2000s, when mentioned papers about  $CeTX_5$  heavy-fermion superconductors were published, a lot of other related substituted rare-earth materials has been prepared as well. From  $RTX_5$  series we can mention  $RCoIn_5$  [48],  $RCoGa_5$  [49] or  $RRhIn_5$  [50, 51] compounds. As for  $R_2TX_8$  series, we can refer to e. g. papers [52, 53] for  $R_2CoIn_8$ , [54] for  $R_2CoGa_8$  or to [55, 56] for  $R_2RhIn_8$  compounds, respectively. General features of most of these compounds are relatively large magnetocrystalline anisotropy which could be attributed to the CF interactions (see e. g. [51, 54] for detailed analysis) and the presence of two low-temperature magnetically ordered phas-

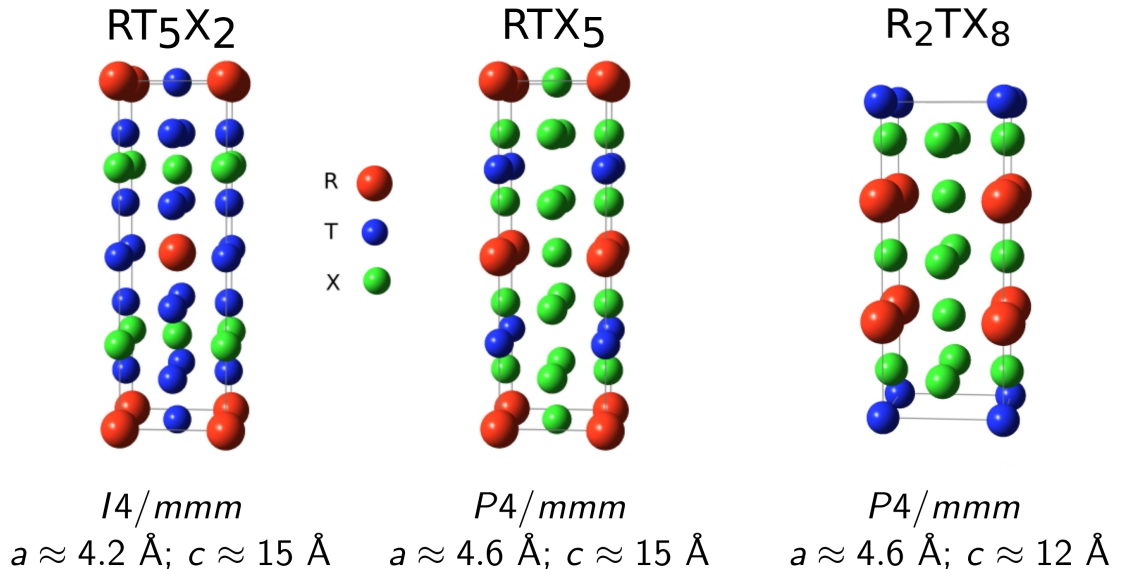


Figure 3.1: Comparison of structures of  $RT_5X_2$ ,  $RTX_5$  and  $R_2TX_8$  compounds: Structure of the  $RT_5X_2$  compounds resembles that of the  $RTX_5$  with exchanged atoms of transition metal ( $T$ ) and  $p$ -metal ( $X$ ).  $R_2TX_8$  structure consists of the same alternating layers of transition metal atoms,  $p$ -metal atoms and layers with rare earth atoms  $R$  as  $RTX_5$ .

es: the ground-state antiferromagnetic phase and another field-induced magnetic phase (even three different phases were observed in the case of  $\text{Ho}_2\text{RhIn}_8$  [57]), see Fig. 3.2.

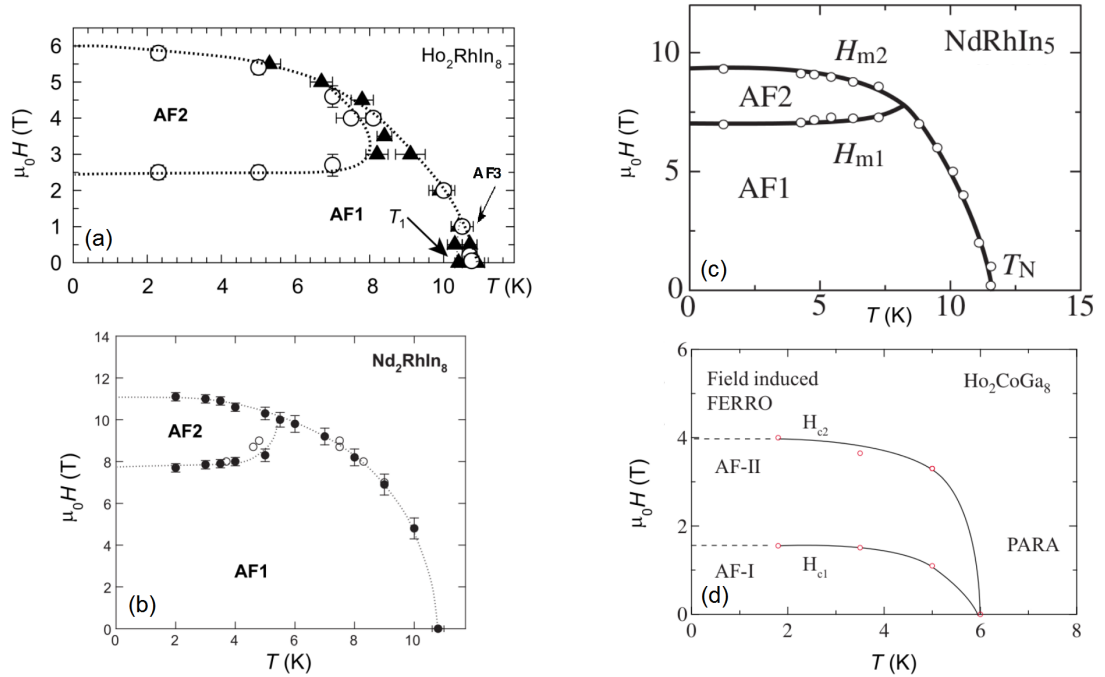


Figure 3.2: Magnetic phase diagrams of  $R_2TX_8$  and  $RTX_5$  compounds in magnetic field applied along the tetragonal  $c$ -axis:  $\text{Ho}_2\text{RhIn}_8$  (a) shows aside from the antiferromagnetic phase AF1 and field-induced phase AF2 also zero-field incommensurate phase AF3 [56, 57]. The phase diagram of  $\text{Nd}_2\text{RhIn}_8$  (b), ref. [58], typical for  $R_2\text{RhIn}_8$  series resembles that of  $\text{NdRhIn}_5$  (c) and other  $RR\text{hIn}_5$  compounds in [50], whereas it differs from the phase diagram proposed for  $\text{Ho}_2\text{CoGa}_8$  (d) from  $R_2\text{CoGa}_8$  series [54], where the region of the field-induced phase reaches down to the temperature axis. Captions and axis descriptions were modified.

### 3.2 $RPd_5Al_2$ compounds

$RPd_5Al_2$  compounds have aroused an interest of scientific community after the discovery of a paramagnetic unconventional heavy-fermion superconductor  $\text{NpPd}_5Al_2$  ( $T_c = 4.9$  K,  $\gamma = 200$  mJ mol $^{-1}$  K $^{-2}$ ) by Aoki et al. in 2007 [4] and a Kondo lattice antiferromagnet  $\text{CePd}_5Al_2$  [5] followed by reporting of a pressure-induced superconductivity in this compound [6]. These findings motivated further investigations of mentioned materials [59–61], revealing i. a. complicated magnetic phase diagram [62] and sinusoidally modulated magnetic structure [63] of  $\text{CePd}_5Al_2$ , as well as studies of analogous compounds also crystallizing in the tetragonal  $\text{ZrNi}_2Al_5$ -type structure (space group  $I4/mmm$ ).

$\text{UPd}_5Al_2$  reported in 2008 [64] exhibit paramagnetic Curie-Weiss behaviour and saturation of the susceptibility in low temperatures due to the non-magnetic ground state. Griveau and his co-workers succeeded in a preparation of  $\text{PuPd}_5Al_2$  which was found to be antiferromagnetic with  $T_N = 5.6$  K but does not present a superconductivity [65].

Ribeiro et al. reported a number of rare-earth based materials  $RPd_5Al_2$  ( $R = Y, Ce, Pr, Nd, Sm, Gd$ ) [66]. Most of them ( $R = Ce, Nd, Sm, Gd$ ) order magnetically, namely  $NdPd_5Al_2$  shows anomaly in the heat capacity due to an antiferromagnetic transition at 1.2 K.  $PrPd_5Al_2$ , studied also by Nakano et al. [27], is a paramagnet with a singlet ground state showing saturation of the low-temperature susceptibility similarly to  $UPd_5Al_2$ .  $YbPd_5Al_2$ , originally presented by Hirose et al. [67], is presumably an antiferromagnet with the ordering temperature only 0.19 K. Another actinide compound  $AmPd_5Al_2$  [68] does not show any hints for magnetic ordering nor superconductivity down to 2 K.

Recently, a paper by Benndorf and his colleagues has been published to complete a family of the  $RPd_5Al_2$  rare-earth compounds with until then missing members ( $R = Tb-Tm$ ) [69], so the whole range of analogous  $4f$ -compounds from Ce to Yb (except for Eu) and the non-magnetic analogues  $YPd_5Al_2$  and  $LuPd_5Al_2$  exist [6, 70]. The new  $RPt_5Al_2$  ( $R = Y, Gd-Tm, Lu$ ) samples were prepared as well [69].

Information about mentioned  $RPd_5Al_2$  compounds is summarized in the Table 3.1.

Whereas previous studies of rare-earth isostructural  $RPd_5Al_2$  homologues [66, 69] deal mainly with polycrystals, in this work we aim also to measurements on a single crystalline sample which is desired for a proper investigation of anisotropic physical properties. Details about its preparation together with the preparation of polycrystals for neutron scattering experiments are presented in the following section.

$R =$	ordering	$T_N$ (K)	form	additional notes	refs.
Ce	AF	2.9, 4.1	single	pressure-ind. SC, easy $c$ -axis	[5, 6, 61–63]
Pr	P	-	single	singlet CF g.s., easy $c$ -axis	[27, 66]
Nd	AF	1.3	single	easy $c$ -axis	[66, 71]
Sm	AF	1.7	poly	isotropic	[66]
Gd	-	6.0	poly	isotropic	[66]
Tb	AF	9.8	poly	-	[69]
Dy	AF	3.7	poly	-	[69]
Ho	P to 2.5 K	-	poly	-	[69]
Er	P to 2.5 K	-	poly	-	[69]
Tm	P to 2.5 K	-	poly	-	[69]
Yb	AF	0.19	single	easy $a$ -axis	[67, 69]
U	P	-	single	non-mag. g. s.	[64]
Np	P	-	single	heavy-fermion SC, easy $a$ -axis	[4, 59, 60, 64]
Pu	AF	5.6	poly	-	[65]
Am	P to 2 K	-	single	non-mag. g. s.	[68]

Table 3.1: Overview of  $RPd_5Al_2$  compounds: Type of ordering (AF for antiferromagnetic, P for paramagnetic), crystalline form of a reported compound (single- or polycrystalline) and additional notes about the magnetocrystalline anisotropy and the ground state (g. s.) are presented.

# 4. Results and discussion

## 4.1 Sample preparation

Single crystalline samples of  $\text{NdPd}_5\text{Al}_2$  have been prepared by the Czochralski method in a tri-arc furnace. Pure metals (Nd: 99.5 % , Pd: 99.995 % , Al: 99.9999 %) were used as a starting material. In case of Nd, the initial purity was further enhanced by solid state electrotransport (SSE). Ingot (rod) of Nd was heated up close to the melting temperature ( $\approx 1200$  K for Nd) by electrical currents ( $\approx 120$  A) and kept there for 3 to 5 weeks for purification. A stoichiometric mixture of all constituent elements with total mass of 8 g was firstly melted into a button under a protective argon atmosphere and flipped and remelted several times for better homogenization. The rod was then pulled out of the melt at a translation speed of 4 mm/h using tungsten as a virtual seed. The resultant ingot consisted of elongated plate-like stacked grains with crystallographic  $c$  direction perpendicular to the ingot. Individual crystals used for the measurement were separated from the ingot with a fine wire saw and polished. Most of the bulk measurements were performed on the same piece of the single crystalline sample with dimensions approximately  $2.3 \times 1.3 \times 0.3$  mm<sup>3</sup> weighing 6.4 mg. From this crystal a small fragment with the mass of  $\sim 1.5$  mg was later separated which was used for the magnetization measurement using a Hall probe. Resistivity and specific heat in the field applied perpendicular to the tetragonal  $c$ -axis were measured using a different samples with masses 1.62 mg, respectively 5.52 mg.

In order to prepare polycrystalline samples for neutron scattering experiments, standard arc melting technique was employed likewise as in the preparation of the button for the Czochralski growth.

To verify homogeneity of the samples, electron-probe microanalysis was performed on the Mira Tescan scanning electron microscope (SEM) equipped with an energy-dispersive X-ray detector (EDX). In case of single crystals, no secondary phase was found. Polycrystalline samples contained except the primary phase attributed to the  $\text{NdPd}_5\text{Al}_2$  also traces of the Pd-Al binary phase or Al-depleted ternary phase. Pieces of polycrystals were further powderized to perform powder X-ray diffraction (XRD) on Bruker D8 diffractometer. XRD measurements implied that our samples were from the vast majority composed of the desired phase and no additional peaks were observable in the XRD patterns beside those corresponding to the  $\text{NdPd}_5\text{Al}_2$  and  $I4/mmm$  space group, see Figure 4.1 and Table 4.1b. Structural parameters were refined with Fullprof software [72] and are given in the Table 4.1a. Quality of the single crystals as well as their orientation was checked by the back-reflection Laue method, see Figure 4.2.

In order to be able to subtract lattice specific heat of  $\text{NdPd}_5\text{Al}_2$ , we have prepared polycrystalline samples of a non-magnetic  $\text{LuPd}_5\text{Al}_2$  compound. Specific heat data of the non-magnetic  $\text{YPd}_5\text{Al}_2$  analogue from [70] were also available.

(a) Structural parameters of NdPd <sub>5</sub> Al <sub>2</sub>				(b) Results of EDX analysis			
Space group:	$a = 4.147(2) \text{ \AA}$			Atomic concentration [%]			
$I4/mmm$ (139)	$c = 14.865(6) \text{ \AA}$						
	$x$	$y$	$z$	#1	#2	ideal 1:5:2	
Nd	0	0	0	Nd	10.3±0.6	0.3±0.1	12.5
Pd (1)	0	0	1/2	Pd	64.8±2.8	63.0±3.4	62.5
Pd (2)	0	1/2	0.146(1)	Al	24.9±0.4	36.7±0.7	25.0
Al	0	0	0.241(3)				

Table 4.1: (a) Structural parameters of NdPd<sub>5</sub>Al<sub>2</sub> refined by the Rietveld method using Fullprof software (See Figure 4.1). (b) Typical composition of the polycrystalline sample as determined by the EDX microanalysis: #1 indicates primary phase and #2 the impurity phase (see the inset of Figure 4.1) . Uncertainties were evaluated by the Esprit software as standard deviations from fitting of the EDX spectra.

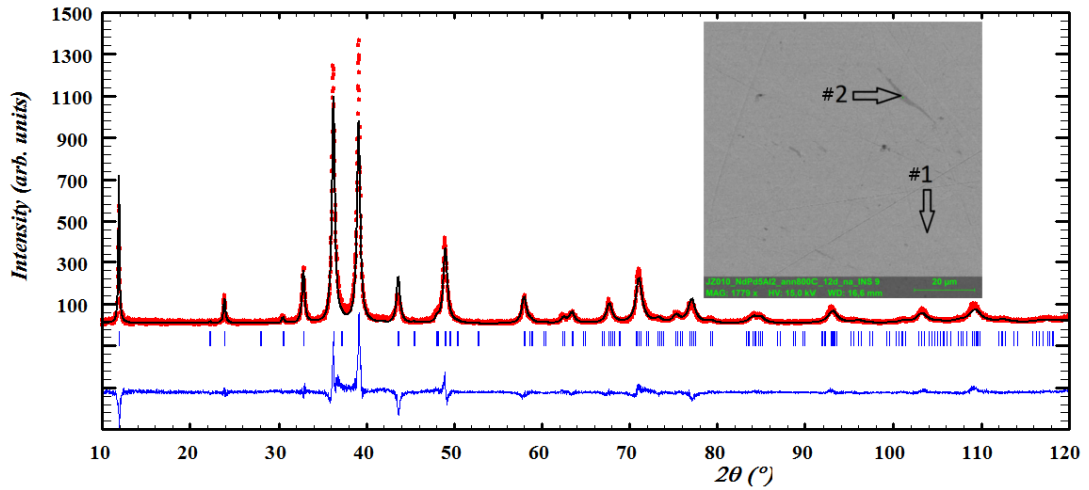


Figure 4.1: Representative powder XRD pattern measured of one of the polycrystalline samples. Red points represent experimental data, black curve fit to the proposed model and blue curve the difference between them. Refined structural parameters are given in the Table 4.1a. Inset shows polished surface of the polycrystalline sample obtained by the SEM imaging in the secondary electron contrast. Composition of the indicated points is given in the Table 4.1b.

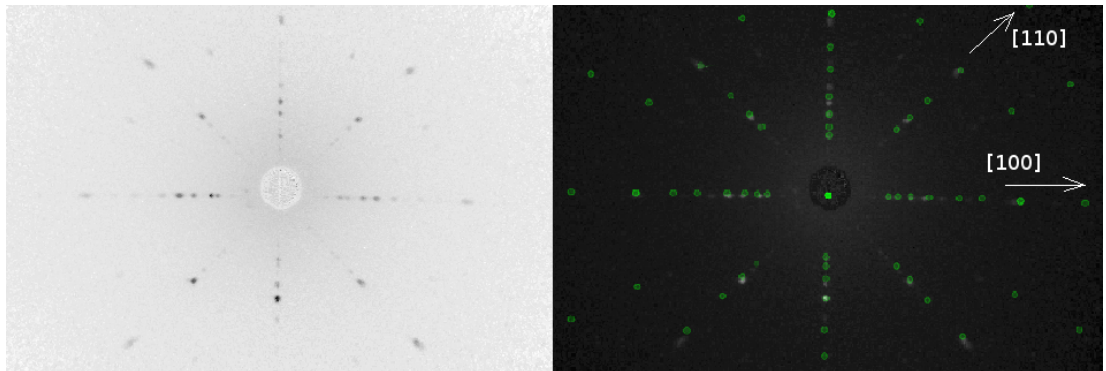


Figure 4.2: Lauegram of NdPd<sub>5</sub>Al<sub>2</sub> single crystal used for the majority of bulk measurements (left) and the same figure complemented by simulated pattern for an appropriate structure (right).

## 4.2 Susceptibility and magnetization

Temperature dependence of magnetic susceptibility is presented in the Figure 4.3. The data were collected in the field of 1 T applied along [100], [110] and [001] directions and in the temperature range from 300 K to 2 K, where the compound is in the paramagnetic state. At temperatures above 100 K the  $H/M$  vs.  $T$  dependences show linear Curie-Weiss-like behaviour for all three field directions. Whereas this more or less holds for the susceptibility in the field applied along the tetragonal  $c$ -axis, which is the easy direction of magnetization, also down to the low temperatures, dependences for the field applied within the basal plane (i. e. for  $H \parallel [100]$  and  $H \parallel [110]$ ) show a noticeable kink below 50 K due to the crystal-field effects which will be further discussed in Section 4.6. The fit to the Curie-Weiss law in the region 50-300 K leads to the paramagnetic Curie-Weiss temperature  $\Theta_p = 8.6$  K and the effective magnetic moment  $\mu_{\text{eff}} = 3.62 \mu_B$  for  $H \parallel [001]$ , respectively  $\Theta_p = -27.1$  K and  $\mu_{\text{eff}} = 3.71 \mu_B$  for  $H \parallel [100]$  and  $\Theta_p = -28.0$  K and  $\mu_{\text{eff}} = 3.68 \mu_B$  for  $H \parallel [110]$ . Values of the  $\mu_{\text{eff}}$  are close to the  $\text{Nd}^{3+}$  free-ion moment. Results of the Curie-Weiss analysis are synoptically summarized in the Table 4.3.

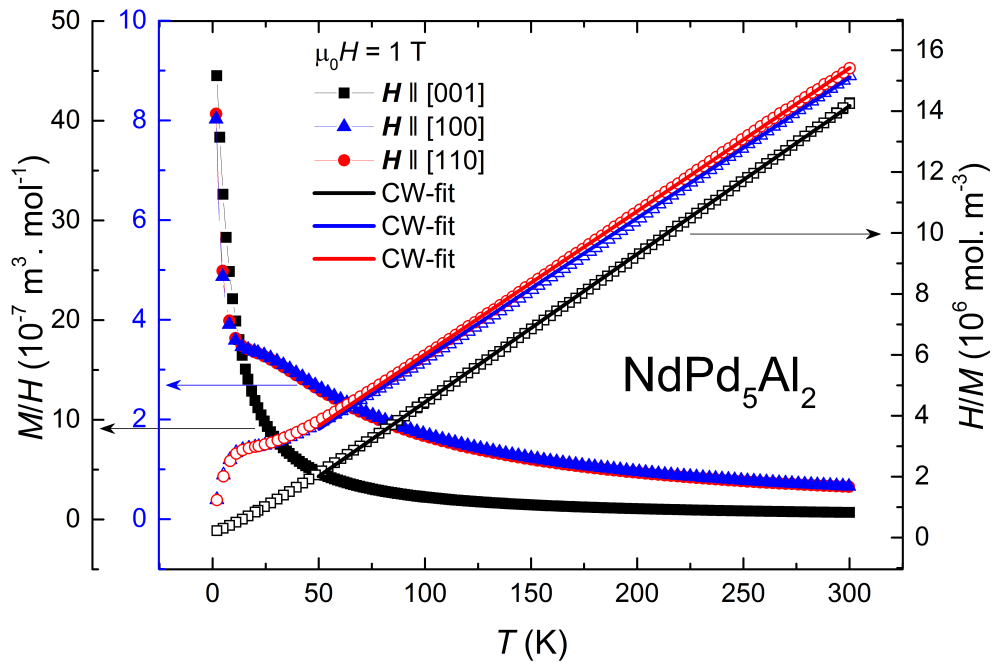


Figure 4.3: The temperature dependence of the magnetic susceptibility in the field of 1 T applied along [100], [110] and [001] directions. Solid lines represent fit by the Curie-Weiss law. Please note different scales on the left y-axis.

	$H \parallel [100]$	$H \parallel [110]$	$H \parallel [001]$
$\mu_{\text{eff}} (\mu_B)$	3.71	3.68	3.62
$\Theta_p$ (K)	-27.1	-28.0	8.6

Table 4.3: Effective magnetic moments  $\mu_B$  and Curie-Weiss paramagnetic temperatures  $\Theta_p$  obtained from the fit by the Curie-Weiss law.

Field dependences of magnetization in the paramagnetic state (Fig. 4.4) were measured for  $H \parallel [100]$ ,  $H \parallel [110]$  and  $H \parallel [001]$  and at 2 K and 10 K. In the range from 0 to 7 T all curves exhibit a linear dependence with exception of  $H \parallel [001]$  at 2 K which saturates at  $\approx 2.3 \mu_B/\text{Nd}$  above 4 T. The data indicate  $c$ -axis as the easy axis of magnetization and corroborates that there is no substantial anisotropy in the basal plane, correspondingly to our results from  $M/H$  vs.  $T$  data.

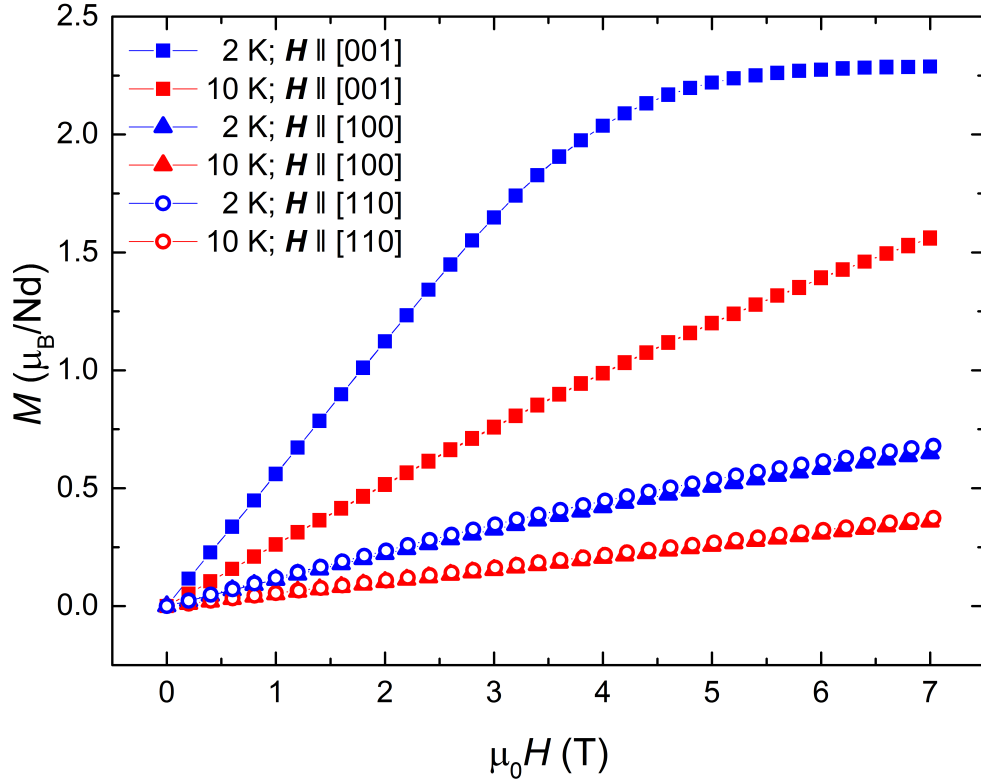


Figure 4.4: Magnetic isotherms in the paramagnetic state for two different temperatures and field applied along the significant crystallographic directions.

Figure 4.5 shows  $M$  vs.  $H$  dependence for  $H \parallel [001]$  measured using the Hall probes. The ordered-state magnetization ( $T < 1.3$  K) shows a rapid increase of the magnetization around 1.25 T in the 0.3 K data which further shifts to the lower fields with increasing temperature. This feature corresponds to the anomaly observed in the specific heat data and can be attributed to the magnetic transition from antiferromagnetic phase 1 to the phase 2 as will be discussed below.

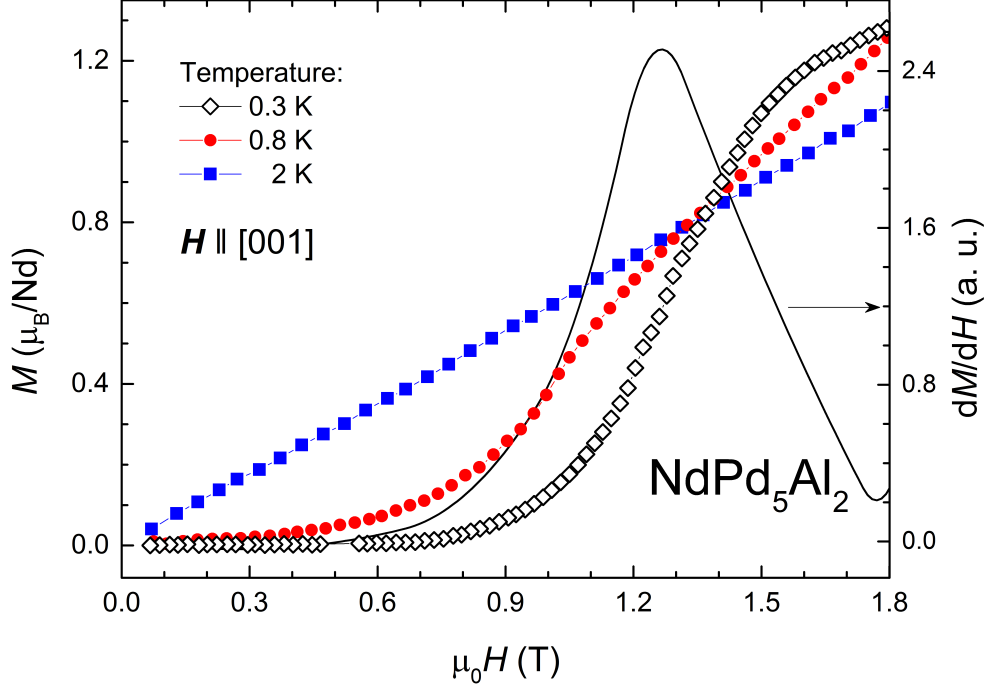


Figure 4.5: Magnetic isotherms in the ordered state and paramagnetic state measured employing the Hall probes. The absolute values were calculated using the reference measurement at 2 K. The solid line represents derivative of the 0.3 K curve. The data are shown only up to 1.8 T since in higher fields the method introduces varying background which is not easy to eliminate completely.

### 4.3 Specific heat and magnetic phase diagram

The low-temperature evolution of specific heat in the magnetic fields applied along [001] direction is presented in the Figure 4.6. It shows a well pronounced anomaly which is related to magnetic order below  $T_N = 1.3(1)$  K, in agreement with previous results [66].

The anomaly in the  $C_p/T$  vs.  $T$  plot shifts to lower temperatures with increasing field suggesting the antiferromagnetic ordering. The 0.94 T dependence reveals additionally another transition at approx. 1.2 K alongside the first one at 0.9 K. This transition is observed only as rather weak anomaly, but becomes more pronounced in higher fields where it also shifts to lower temperatures (see inset of Figure 4.6). The 1.08 T dependence still features both transitions, while in higher fields only the transition at higher temperature is observable in our specific heat data.

Figure 4.7 presents  $C_p/T$  vs.  $T$  in magnetic fields applied perpendicular to the [001] direction. In contrast with heat capacity for  $H \parallel [001]$ , specific heat for  $H \perp [001]$  is not significantly influenced by low magnetic fields (e. g. 0.5 T). The antiferromagnetic ordering still survives in the field of 3 T, while in 5 T, we already observe  $C_p/T$  vs.  $T$  behaviour which reflects the field-induced ferromagnetic state.

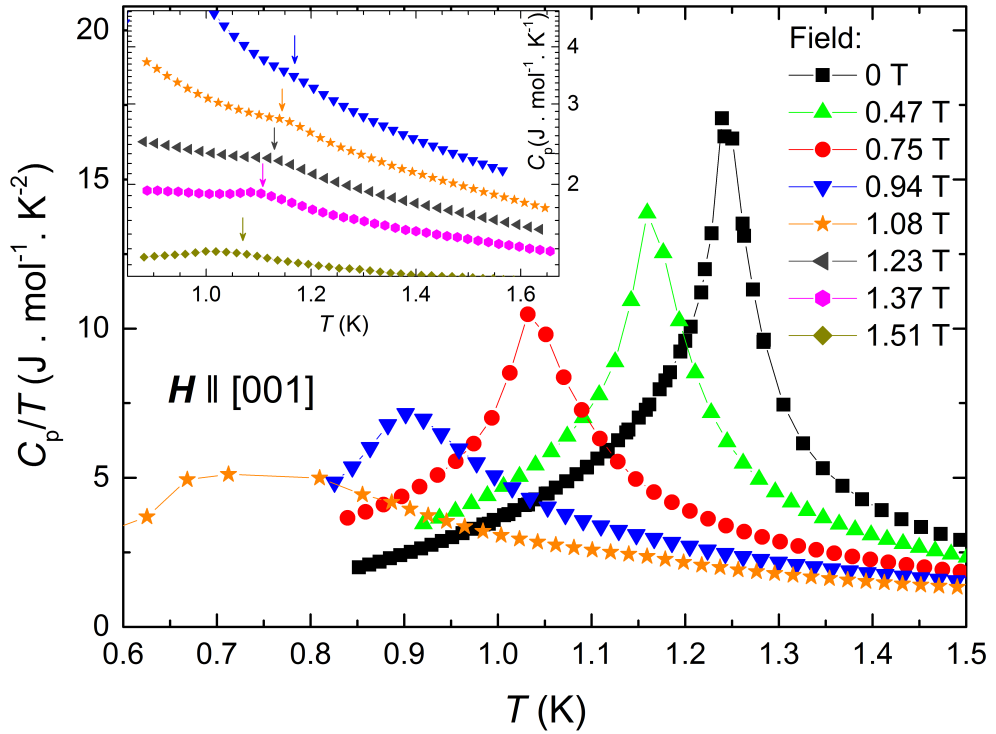


Figure 4.6: Low-temperature specific heat of  $\text{NdPd}_5\text{Al}_2$  plotted as  $C_p/T$  vs.  $T$ . Measurements were performed in magnetic fields applied along the tetragonal  $c$ -axis using dual-slope curve analysis. The inset depicts a detail of the  $C_p(T)$  dependence in the region where another transition appears.

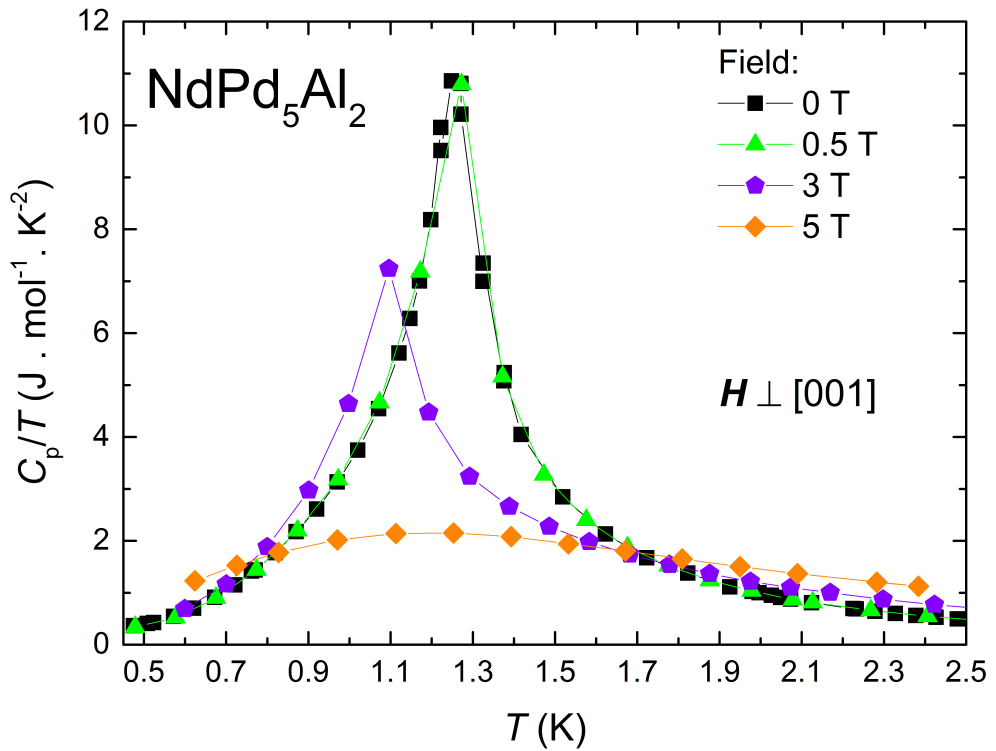


Figure 4.7: Low-temperature specific heat (plotted as  $C_p/T$  vs.  $T$ ) in magnetic fields applied perpendicular to the tetragonal  $c$ -axis. Data were collected using standard time-relaxation technique.

Besides the  $C_p(T)$ , we have also measured the dependence of the heat capacity on magnetic field in the ordered state. Results for the measurement at 0.8 K are presented in the Figure 4.8a. The data clearly demonstrate the occurrence of the two phase transitions located around 1 and 3 T and resemble  $C_p(H)$  dependences measured for e. g.  $\text{Nd}_2\text{RhIn}_8$  [73]. the field-induced ferromagnetic state.

In addition, we also present the magnetoresistivity measured above and below  $T_N$  (Figure 4.8b). The ordered-state data apparently differ from the paramagnetic ones by the hump between 1 and 3 T. Nevertheless, the transitions are not so pronounced in the case of magnetoresistivity as in the heat capacity data and were not used to construct the magnetic phase diagram. We note that weak magnetoresistivity effect was found also in related  $\text{Nd}_2\text{RhIn}_8$  compound [58]. Temperature dependence of resistivity in zero field (inset of Figure 4.8b) shows similar behaviour around the transition temperature as in previously studied  $\text{Nd}_2\text{TIn}_8$  and  $\text{NdTIn}_5$  compounds [55].

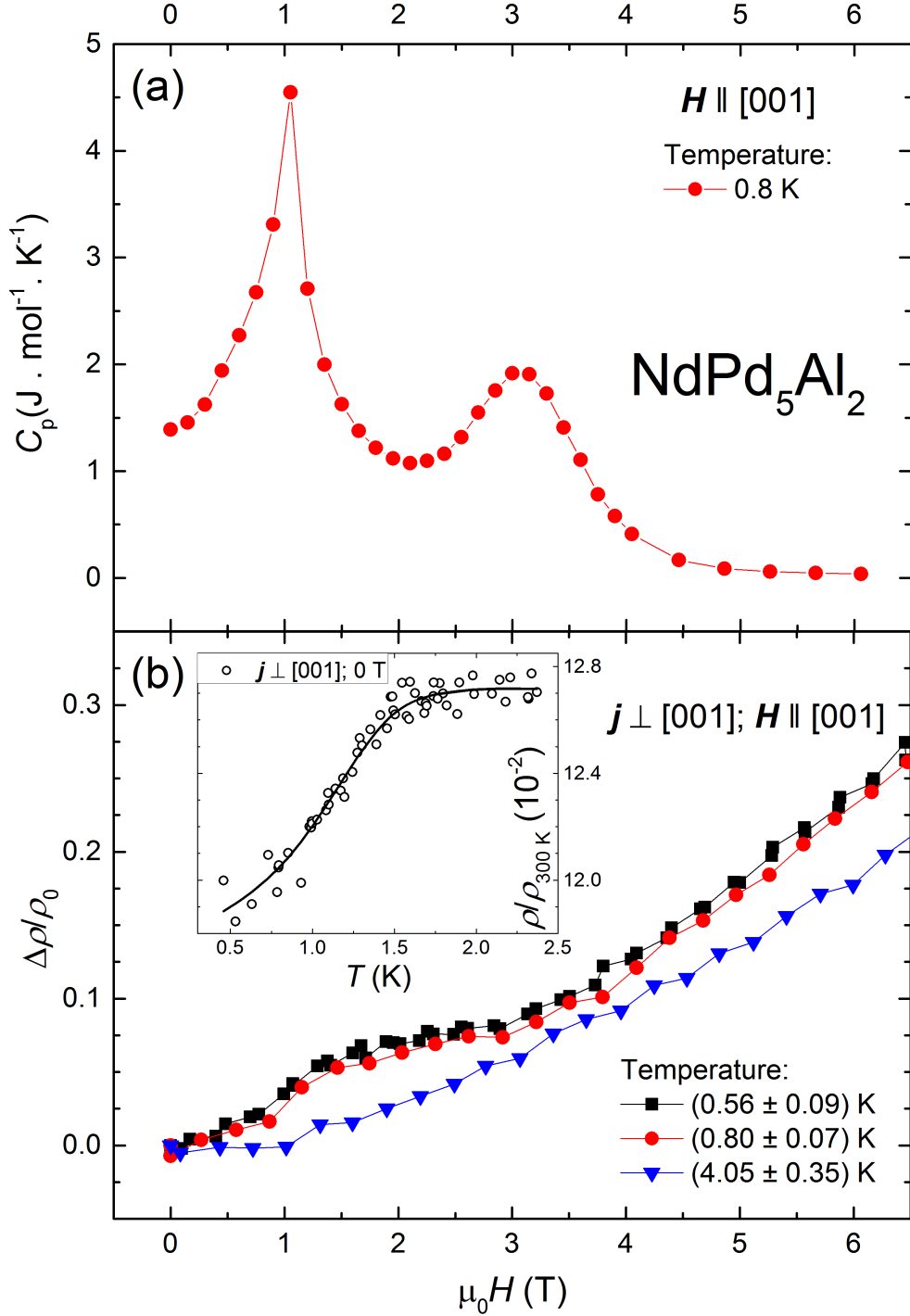


Figure 4.8: Specific heat as a function of magnetic field (a). Magnetoresistivity (b) expressed as the  $\Delta\rho/\rho_0$  ratio where  $\Delta\rho = \rho(H, T) - \rho_0$  and  $\rho_0$  is the resistivity in zero field. The inset of the lower figure shows the resistivity around the phase transition. Solid line represents smoothing spline interpolation of the data and is just a guide for an eye.

The magnetic phase diagram represented in the Figure 4.9 summarizes our findings from low-temperature  $C_p$  and  $M(H)$  measurements in field applied along the  $c$ -axis (Sections 4.2 and 4.3). It features two different magnetic phases - the lower-field phase 1 which is supposed to be antiferromagnetic and another field-induced magnetic phase 2.

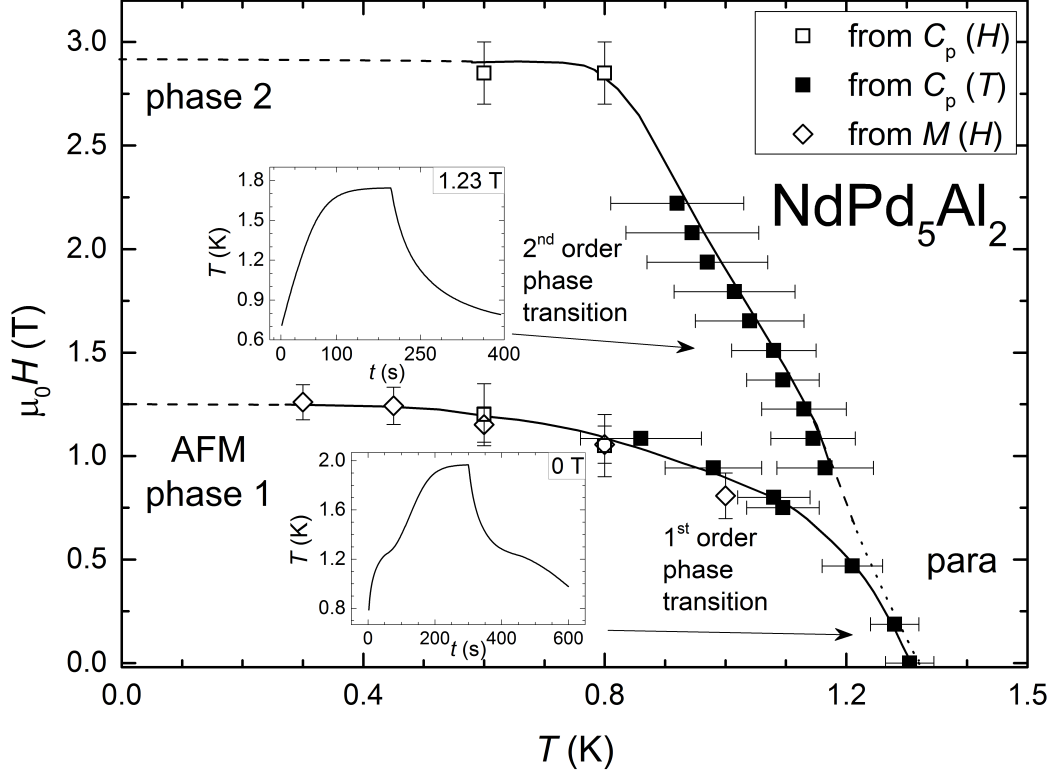


Figure 4.9: The magnetic phase diagram of  $\text{NdPd}_5\text{Al}_2$  based on the  $C_p(T)$  (full squares),  $C_p(H)$  (empty squares) and  $M(H)$  (empty diamonds) measurements in field applied along the  $c$ -axis. The error bars were estimated from the width of the anomalies in the case of  $C_p(T)$  and  $M(H)$  data and from the step between datapoints in the  $C_p(H)$  data. The lines connecting points in the graph are just a guide for an eye. The insets show temperature vs. time dependences during the heating pulse in the field of 0 and 1.23 T demonstrating different order of the two phase transitions. The dotted line serves as a tentative phase border as discussed in Section 4.7.

The insets in the Figure 4.9 display time dependences of the sample's temperature during the constant heating pulse and following relaxation. Their shape is clearly different when measured below 0.5 T and above 1.1 T. Whereas the low-field curves exhibit plateaus around  $T_N$  due to the latent heat involved indicating the first-order phase transition, the curves above 1.1 T show behaviour typical for the second-order phase transition; in the region from approx. 0.5 T to 1.1 T curves gradually change their character from the former type to the latter.

## 4.4 Magnetic specific heat

Figure 4.10a presents magnetic specific heat of  $\text{NdPd}_5\text{Al}_2$ . To evaluate this magnetic contribution, we have subtracted specific heat of analogous non-magnetic  $\text{LuPd}_5\text{Al}_2$  and  $\text{YPd}_5\text{Al}_2$  [70] compounds from the total specific heat of the  $\text{NdPd}_5\text{Al}_2$ :  $C_{\text{mag}}(\text{NdPd}_5\text{Al}_2) = C(\text{NdPd}_5\text{Al}_2) - C(\text{non-mag.})$ . As can be deduced from Fig. 4.10b, these compounds are not good non-magnetic analogues for  $\text{NdPd}_5\text{Al}_2$  since they both seemingly undervalue phonon contribution to the heat capacity of  $\text{NdPd}_5\text{Al}_2$  leading to the magnetic entropy which exceeds the possible high-temperature limit.

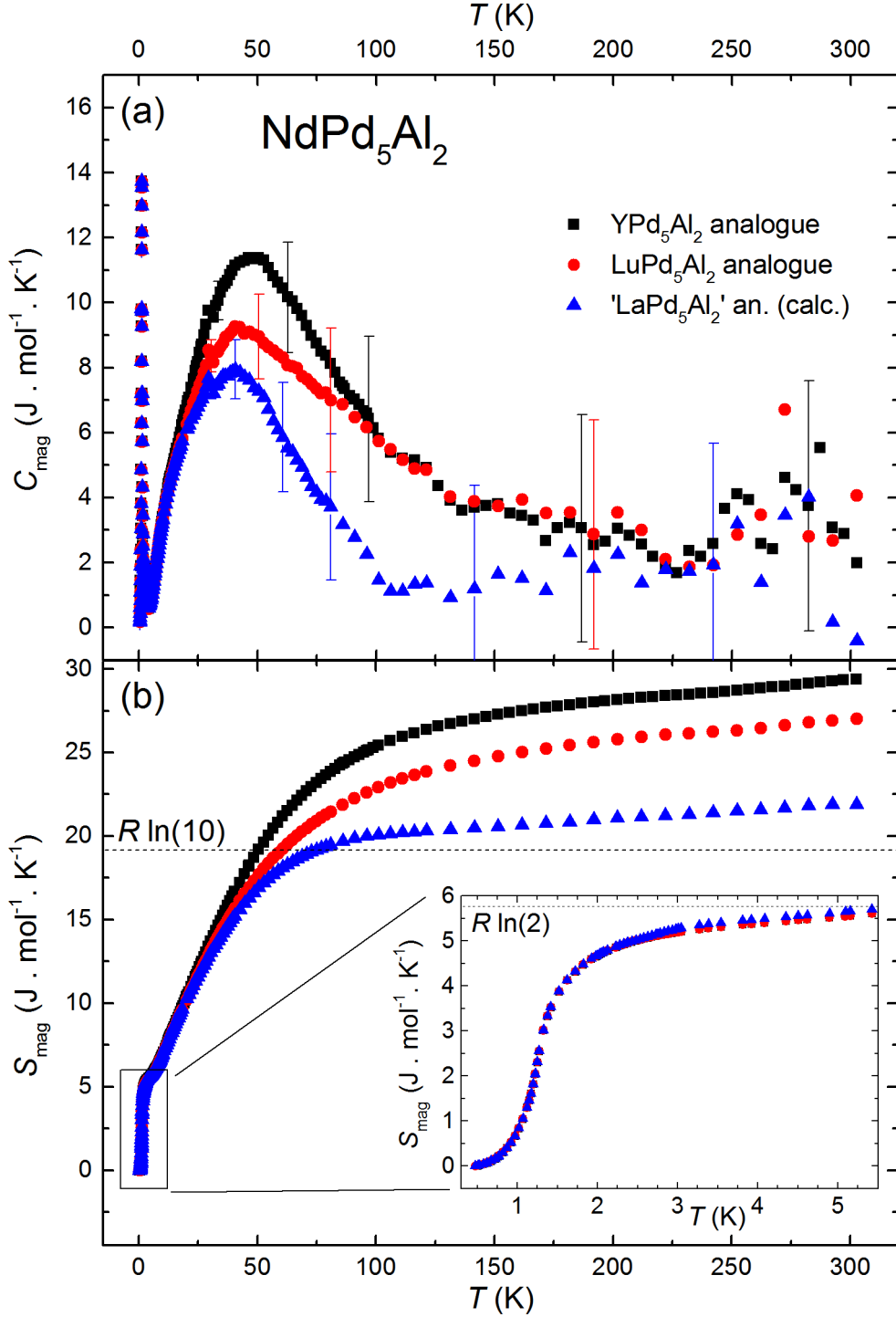


Figure 4.10: (a) Magnetic specific heat of  $\text{NdPd}_5\text{Al}_2$  obtained by subtracting lattice specific heat of various non-magnetic analogues, i. e.  $C_{\text{mag}}(\text{NdPd}_5\text{Al}_2) = C(\text{NdPd}_5\text{Al}_2) - C(\text{non-mag.})$ . Error bars were estimated assuming 1 % error of initial values. (b) Corresponding magnetic entropy of  $\text{NdPd}_5\text{Al}_2$ . Detail shows a zoomed low-temperature region.

The probably much more convenient analogue  $\text{LaPd}_5\text{Al}_2$  presumably does not form, we have therefore tried to approximate its lattice specific heat by simple

relation (being aware of its limited validity) as

$$C_p(\text{"LaPd}_5\text{Al}_2\text{"}) = C_p(\text{YPd}_5\text{Al}_2) \frac{C_p(\text{La}_2\text{RhIn}_8)}{C_p(\text{Y}_2\text{RhIn}_8)}, \quad (4.1)$$

where we employed available specific heat data of non-magnetic  $R_2\text{RhIn}_8$  compounds [37]. Estimated magnetic specific heat of  $\text{NdPd}_5\text{Al}_2$  using this analogue results into somewhat more reasonable value of magnetic entropy at high temperatures, i. e. closer to  $R \ln 10$  (Fig. 4.10b). As can be seen in the inset of the figure, the entropy at low temperatures reaches  $R \ln 2$  close above  $T_N$ , indicating the doublet ground state.

Figure 4.11 shows the low-temperature magnetic heat capacity of  $\text{NdPd}_5\text{Al}_2$  (using yttrium analogue) replotted as  $C_{\text{mag}}/T$  vs.  $T^2$ . Since the lattice contribution to the specific heat of  $\text{NdPd}_5\text{Al}_2$  is negligible in comparison with the magnetic specific heat in the presented temperature region, the choice of the non-magnetic analogue does not play an important role here (see the inset the Fig. 4.10b). The data in the ordered state have been fitted by the expected specific heat dependences (1.42) for magnetic excitations (including a gap in the magnon spectrum). However, we are not able to unambiguously determine whether the compound exhibits 3D or 2D antiferromagnetic magnons mainly due to the very limited fitting range, in which the experimental data can be reasonably described by both dependences as presented in the Figure 4.11.

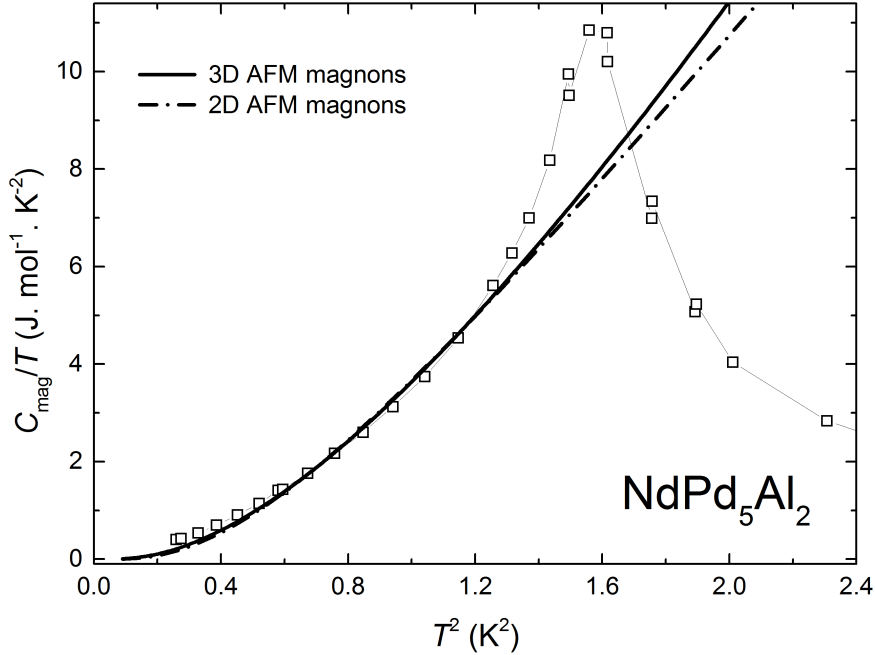


Figure 4.11: Low-temperature magnetic specific heat replotted as  $C_{\text{mag}}/T$  vs.  $T^2$ . Data were evaluated using standard time-relaxation method. The thick lines represents fits of the data by the expected dependences given by the Equation 1.42 for antiferromagnetic excitations. The resulting parameters obtained by the fitting in the temperature range 0.5-1.1 K are  $a = 17.10 \text{ J mol}^{-1} \text{ K}^{-4}$  and  $\Delta = 1.55 \text{ K}$  for the 3D AFM magnons, respectively  $a = 44.27 \text{ J mol}^{-1} \text{ K}^{-3}$  and  $\Delta = 2.49 \text{ K}$  for the 2D AFM magnons.

## 4.5 Neutron diffraction

### 4.5.1 Magnetic structure

In order to determine the ground-state magnetic structure of  $\text{NdPd}_5\text{Al}_2$ , the experiment of powder neutron diffraction was performed on the E6 diffractometer at the Helmholtz Centre Berlin using the neutron wavelength\* 2.414 Å. A polycrystalline sample (same as for the INS experiment) with the total mass of 4.3 g was used. Since the experiment required very low temperatures down to 0.4 K, a cylindrical copper sample container was employed instead of a more common vanadium one. In addition to that, the powdered sample was mixed with the deuterized ethanol/methanol solution to assure proper thermalisation.

After installing the sample we have at first collected data well in the paramagnetic state, namely at 5.5 K. In total, we have measured 12 approximately one-hour full-range scans at higher resolution which were then summed up. Figure 4.12 shows the resulting pattern including structure refinement in the  $I4/mmm$  space group leading to lattice parameters  $a = 4.097$  Å and  $c = 14.751$  Å and Bragg  $R$ -factor 20.9%. The original data contained additionally two peaks

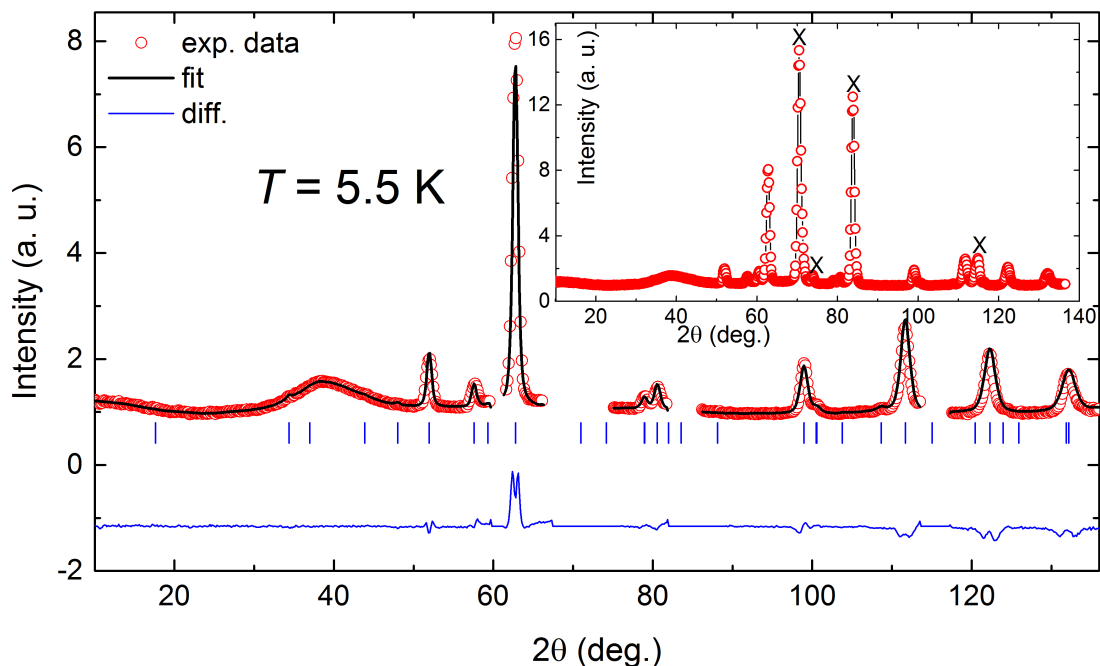


Figure 4.12: Refined neutron diffraction pattern taken in the paramagnetic state at 5.5 K. The inset shows original data with the peaks which were excluded from the fitting (X). Further details in the text.

coming from the holder at positions  $2\theta \approx 71^\circ$  and  $2\theta \approx 84^\circ$  which pertain to reflections (111), respectively (200) of copper (two strongest peaks in the inset of Fig. 4.12). Apart from that, we have also observed peaks at positions approximately  $62^\circ$ ,  $75^\circ$  and  $116^\circ$  which cannot be attributed to  $\text{NdPd}_5\text{Al}_2$  and were not detected in the room-temperature XRD measurements. These peaks were

---

\*Since the measurement of the standard sample was not carried out before the experiment and settings of the monochromator was changed during the measurement, we have evaluated the neutron wavelength from the position of diffraction (200) of the copper holder.

present both in the paramagnetic data at 5.5 K and in ordered-state pattern at 0.4 K, their magnitudes do not change registerably between these two temperatures and their intensities are comparable with the intensities belonging to the primary phase even at relatively high angles. From that we can infer that these diffractions are presumably nuclear peaks which could be ascribed to a so-far unspecified foreign phase. To disprove/confirm that this phase is really intrinsic to the sample and to reveal eventually its precise character low-temperature XRD would be desirable. However, there were no indications in our bulk measurements on a single crystalline sample which would speak in favour of existence or forming of such a phase. Consequently, we have excluded due to these additional peaks corresponding  $2\theta$ -regions from the original diffraction patterns. Besides, the data contained a broad hump around  $2\theta \approx 40^\circ$  attributed to the mentioned amorphous ethanol/methanol mixture which was treated as a background.

Figure 4.13 presents the ordered-state diffraction pattern measured at 0.4 K with the same statistics as the 5.5 K data. By comparison with the paramagnet-

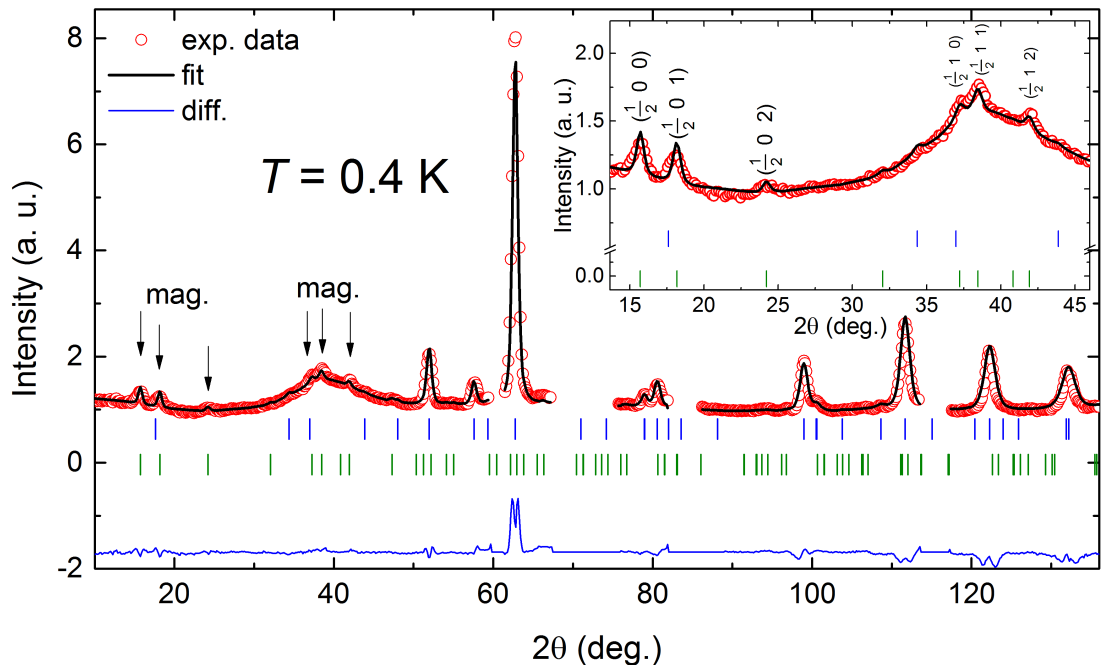


Figure 4.13: Neutron diffraction pattern taken in the antiferromagnetic state and zero external magnetic field including refinement. The inset depicts the detail of strongest magnetic peaks in the low-angle region.

ic pattern we were able to identify a signal of the magnetic origin, especially we have observed several strong magnetic reflections at low angles (inset of Fig. 4.13). Having known the crystal structure given by nuclear peaks already, we have used positions of these magnetic peaks as the input for the `kSearch` utility (part of the Fullprof Suite). The program has determined  $\mathbf{k} = (\frac{1}{2}00)$  as the most plausible propagation vector. Moreover, representational analysis using `SARAh` and `BasIreps` software was employed to reveal possible basis vectors consistent with this propagation vector, space group  $I4/mmm$  and Nd at the Wyckoff position  $2a$  lying along one of the crystallographic axes. Supposing  $\mathbf{k} = (\frac{1}{2}00)$  and the basis vector parallel to the crystallographic  $x$  or  $y$  axes, we were not able to qualitatively well reproduce all magnetic peaks. In contrast, the interpretation

of the data was successful assuming  $\mathbf{k} = (\frac{1}{2}00)$  and basis vector aligned to the direction of the tetragonal  $c$ -axis resulting into the magnetic  $R$ -factor 29.4 % and magnetic moments with the magnitude of  $2.22 \mu_B$  which corresponds well to the magnetization data (Figs. 4.4 and 4.5). Enhanced value of the magnetic  $R$ -factor is due to the relatively low intensity of magnetic reflections. Nevertheless, the calculation well reproduce the experimental data as can be seen in Fig. 4.13. The lower magnetic moment here (in comparison with the free-ion value  $3.27 \mu_B$ ) reflects the effect of CF.

In general, there is also a possibility that more than one propagation vector is involved in description of magnetic structure, e. g. it may simultaneously contain several vectors from so-called star of the propagation vector (set of propagation vectors arising from a given  $\mathbf{k}$  by applying operations of rotational symmetry of the space group) [37]. But in our case no such option is applicable to explain reasonably our data.

To conclude:  $\text{NdPd}_5\text{Al}_2$  is presumably a collinear antiferromagnet characterized by the propagation vector  $\mathbf{k} = (\frac{1}{2}00)$  with magnetic moments oriented along the tetragonal  $c$ -axis. The proposed magnetic structure is depicted in Fig. 4.14.

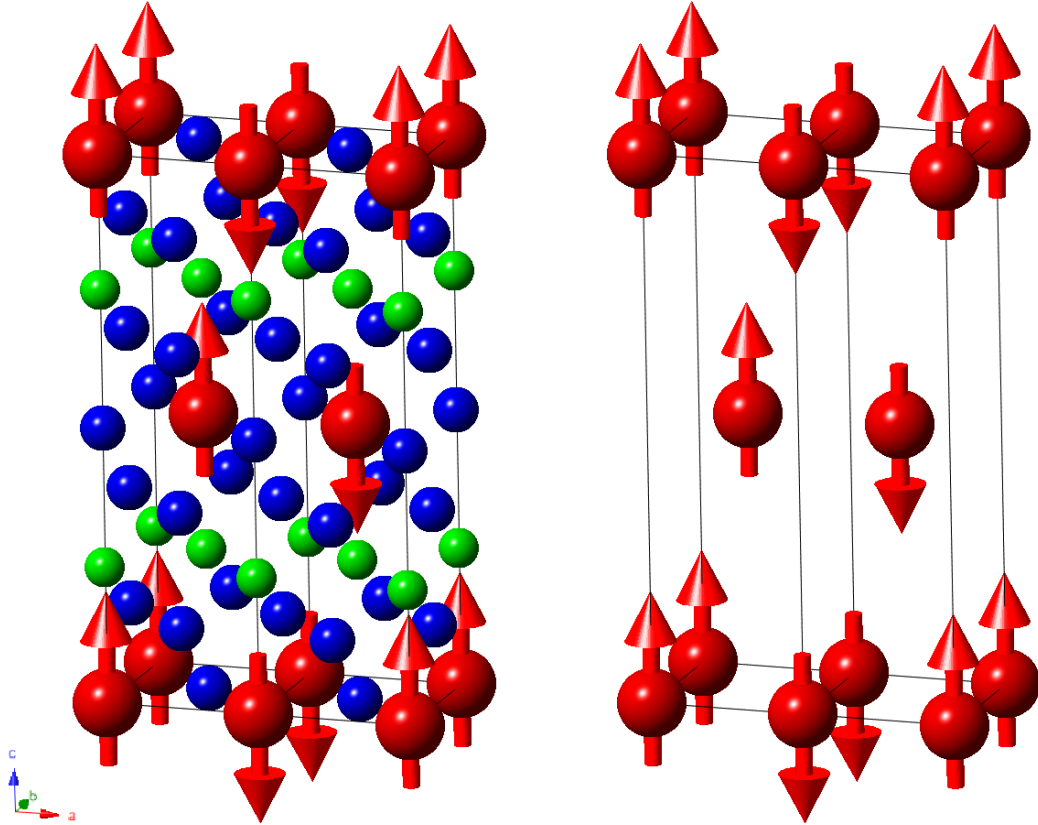


Figure 4.14: Magnetic structure of  $\text{NdPd}_5\text{Al}_2$  with all atoms (left) and magnetic Nd atoms only (right).

## 4.5.2 Critical behaviour

To follow the temperature development of magnetic intensities and to assess the critical behaviour of  $\text{NdPd}_5\text{Al}_2$ , we have, apart from previously mentioned measurements, taken also several diffraction patterns with lower statistics in the limited angular range and at temperatures from 0.4 K to 1.4 K. The paramagnetic pattern obtained at 5 K was then used for subtraction of the non-magnetic signal, resulting data for diffractions  $(\frac{1}{2}00)$  and  $(\frac{1}{2}01)$  are shown in the Fig. 4.15a. Expectedly, magnitudes of magnetic reflections gradually decrease with increasing temperature, more abruptly above ca. 1 K. Figure 4.15b presents temperature of their intensities from 0.4 K to 1.35 K<sup>†</sup>. Fitting of this dependence to the power law  $I \propto (T_N - T)^{2\beta}$  leads to the  $T_N = 1.37(2)$  K for  $(\frac{1}{2}00)$  diffraction and  $T_N = 1.32(2)$  K for  $(\frac{1}{2}01)$  diffraction and critical exponents  $\beta = 0.10(2)$  for  $(\frac{1}{2}00)$  and  $\beta = 0.09(2)$  for  $(\frac{1}{2}01)$  diffraction, respectively. Varying of the lower bound of the fitting range in the interval from 0.4 K up to  $\sim 0.9$  K does not change these parameters significantly. Resulting Néel temperatures are consistent with  $T_N = 1.3(1)$  K as determined from the specific heat. Obtained critical exponents are substantially lower than corresponding values theoretically predicted ([37] and refs. therein) by the mean-field theory ( $\beta = \frac{1}{2}$ ), for Heisenberg ( $\beta = 0.367$ ), X-Y ( $\beta = 0.345$ ) or Ising 3D model ( $\beta = 0.313$ ). They are rather closer to the value for the Ising 2D model where  $\beta = \frac{1}{8}$ .

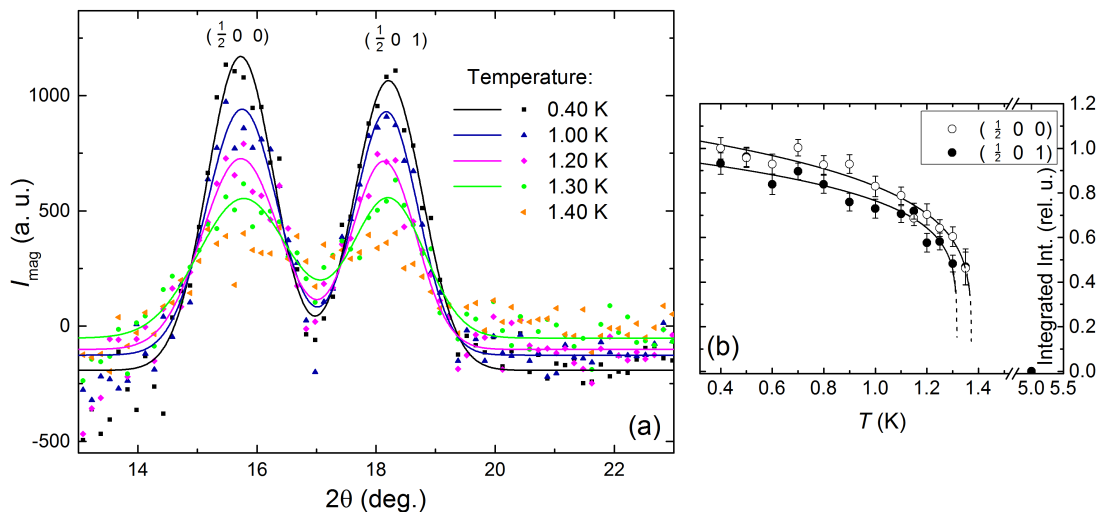


Figure 4.15: (a) Temperature dependence of magnetic reflections  $(\frac{1}{2}00)$  and  $(\frac{1}{2}01)$ . Full lines represent fits by the Gaussian function. (b) Integrated intensities as resulting from the Gaussian fit normalized to the intensity of magnetic reflection  $(\frac{1}{2}00)$  at 0.4 K. Full line represents fit to  $I \propto (T_N - T)^{2\beta}$  leading to the  $T_N = 1.37(2)$  K and  $\beta = 0.10(2)$  for  $(\frac{1}{2}00)$  reflection, respectively  $T_N = 1.32(2)$  K and  $2\beta = 0.9(2)$  for  $(\frac{1}{2}01)$  reflection.

<sup>†</sup>We note that we have registered some intensity of the magnetic origin in the vicinity of the diffractions  $(\frac{1}{2}00)$  and  $(\frac{1}{2}01)$  also at 1.4 K., but this signal had rather a form of broad feature than of distinct well-resolved peaks so we did not consider it for further analysis.

## 4.6 Crystal-field analysis

In order to inspect the influence of the CF on properties of  $\text{NdPd}_5\text{Al}_2$  and eventually evaluate CF parameters which determine CF states and energies we have employed following three different approaches: Fitting of experimental  $M/H$  vs.  $T$  data based on relation (1.26) is a significant extension of standard Curie-Weiss analysis and it might be seen as an indirect method of determination of CF parameters since susceptibility comprises averaged information about CF states and energies. It can be utilized using data obtained by measurements on relatively small single crystalline samples (i. e. in order of  $\sim 1$  mg). On the contrary, analysis of the CF by INS allows to exactly determine CF energy levels. However, a relatively large amount of the sample is required and in case of polycrystalline powder and unpolarized neutrons averaging of matrix elements of the angular momentum (2.7) still applies instead of detecting appropriate matrix elements between particular states directly. Theoretical approach complements these two methods enabling computation of CF parameters with help of up-to-date first-principles techniques.

One of the major disadvantages in determination of CF parameters is, that complete set of these parameters cannot be reasonably estimated in advance by e. g. using a known set of CF parameters for a different isostructural rare-earth compound. We therefore further compare outcomes of these methods applied on  $\text{NdPd}_5\text{Al}_2$ , discuss qualitatively some aspects of the CF in this compound and confront them with our magnetization and specific heat measurements to assess their reliability.

### 4.6.1 Susceptibility fitting and ab-initio calculations

To evaluate CF parameters of from experimental susceptibility data a self-assembled Matlab code was employed. This program operates with Stevens operators and computes eigenvalues and eigenstates of the CF Hamiltonian. At first, we have produced a routine which calculates susceptibility according relations (1.26) and (1.31) using CF parameters and eventually the molecular field constant  $\lambda_i$  and a temperature-independent term  $\chi_0^i$  as the input. Fitting script utilizing lsqnonlin solver [74] then enables to solve inverse problem and extract these parameters from experimental data. It uses least-squares minimization and fits two experimental dependencies for  $H \parallel [001]$  and  $H \perp [001]$  simultaneously to obtain one set of CF parameters.

First-principles calculations of CF parameters were performed by doc. Martin Diviš using the same method of computation as in [75]. Within this method, the electronic structure and corresponding distributions of ground-state charge density are obtained using the full potential augmented plane waves plus local orbitals. The CF parameters then originate from the aspherical part of the total single-ion potential in the crystal. For more details and description of the method refer to [76].

The resulting susceptibility fit for  $\text{NdPd}_5\text{Al}_2$  is presented in Fig. 4.16. As can be seen it reproduces well experimental  $M/H$  vs.  $T$  data for both directions of the field in the whole temperature range 2-300 K. Parameters of the fit and resulting energies and wavefunctions corresponding to the 5 Kramers doublets

of  $\text{Nd}^{3+}$  ion in the tetragonal CF are summarized in the Table 4.4. Observed anisotropy of the susceptibility is predominantly caused by the CF effects, molecular field (represented by parameters  $\lambda_i$  for particular directions) introduces only a small shift of the reciprocal susceptibility. Obtained values of  $\chi_0^i$  were within the numerical precision of the fit equal to zero. Resulting value of the parameter  $B_2^0 = -0.557$  K is significantly lower than that which might be estimated from paramagnetic Curie-Weiss temperatures (Table 4.3) using Eq. (1.35), i. e.  $B_2^0 \approx -1.2$ - $1.3$  K. This might suggest that anisotropic properties of  $\text{NdPd}_5\text{Al}_2$  are influenced by higher-order CF parameters since the relation (1.35) assumes the only lowest-rank approximation [10]. A kink observed in the dependence for  $H \parallel [100]$  around ca. 30 K might be with respect to obtained results associated to the energy position and properties of the first excited doublet  $|\psi_{\text{II}}\rangle \pm 0.586 |\pm 5/2\rangle \mp 0.81 |\mp 3/2\rangle$  as this gets thermally occupied, since this state leads to  $|\langle \psi_{\text{II}} | J_x | \psi_{\text{II}} \rangle|^2 = 0.45$ , whereas  $|\langle \psi_{\text{I}} | J_x | \psi_{\text{I}} \rangle|^2 = 0$  for the ground state  $|\psi_{\text{I}}\rangle = 0.895 |\pm 9/2\rangle - 0.431 |\pm 1/2\rangle + 0.11 |\mp 7/2\rangle$ .

CF parameters										
$B_2^0$ (K)	$B_4^0$ (K)	$B_4^4$ (K)	$B_6^0$ (K)	$B_6^4$ (K)	$\lambda$ (mol/m <sup>3</sup> )			$\chi_0$ (m <sup>3</sup> /mol)		
-0.557	-0.041	0.261	-0.0009	0.0011	$\lambda_{[100]} = -1.36 \times 10^5$			$\chi_0^{[100]} \approx 0$		
					$\lambda_{[001]} = -2.24 \times 10^5$			$\chi_0^{[001]} \approx 0$		
Energies and wave functions										
$E$ (K)	$ 9/2\rangle$	$ 7/2\rangle$	$ 5/2\rangle$	$ 3/2\rangle$	$ 1/2\rangle$	$ -1/2\rangle$	$ -3/2\rangle$	$ -5/2\rangle$	$ -7/2\rangle$	$ -9/2\rangle$
259.8	0.067	0	0	0	0.375	0	0	0	0.925	0
259.8	0	0.925	0	0	0	0.375	0	0	0	0.067
180.9	0	0	-0.81	0	0	0	-0.586	0	0	0
180.9	0	0	0	-0.586	0	0	0	-0.81	0	0
100.4	-0.44	0	0	0	-0.821	0	0	0	0.365	0
100.4	0	-0.365	0	0	0	0.821	0	0	0	0.44
40.5	0	0	0.586	0	0	0	-0.81	0	0	0
40.5	0	0	0	0.81	0	0	0	-0.586	0	0
0	0	0.11	0	0	0	-0.431	0	0	0	0.895
0	0.895	0	0	0	-0.431	0	0	0	0.11	0

Table 4.4: CF parameters, energy levels and corresponding wave functions for  $\text{NdPd}_5\text{Al}_2$  as resulting from the susceptibility fit (see Fig. 4.16).

CF parameters and energies for  $\text{NdPd}_5\text{Al}_2$  obtained by first-principles calculations are shown and compared to the output of the susceptibility fitting in the Table 4.5. As can be seen in the Fig. 4.16, calculated susceptibility using these parameters corresponds qualitatively with the experimental data showing a negative value of the parameter  $B_2^0 < 0$  (similarly as the susceptibility fit) which is consistent with the [001] direction as the easy axis of magnetization. However, deviation from the experimental data is recognizable especially for  $H \parallel [100]$  (hard axis of magnetization) at low temperatures below  $\approx 50$  K. This is seemingly a reflection of the fact that presented set of the first-principles CF parameters estimate energy of the first excited doublet as 14.5 K which is much lower than its real position as will be shown in Section 4.6.2 discussing the INS experiment. Both methods of determination of the CF parameters indicate the ground-state doublet consisting primarily from the  $|\pm 9/2\rangle$  wave functions leading to slightly different moments  $g\langle J_z \rangle = 2.66 \mu_B$  for the parameters from the susceptibility fit and  $g\langle J_z \rangle = 2.49 \mu_B$  for the parameters from the first principles, respectively, which is reduced with respect to the free-ion saturated moment  $3.27 \mu_B$ . We have

thus confronted these sets of CF parameters also with the experimental  $M(H)$  data measured at 2 K and calculated magnetization using relation (1.12) and diagonalization of the Hamiltonian Eq. (1.24) in field. The comparison is presented in the inset of the Fig. 4.16. As can be seen, these calculated curves follow the experimental data for  $H \parallel [100]$ . Nevertheless, they both exceed the  $M(H)$  for  $H \parallel [001]$  and result into a high-field values of magnetization higher than experimental  $\approx 2.3\mu_B$  in 7 T.

CF parameters (K)					
	$B_2^0$	$B_4^0$	$B_4^4$	$B_6^0$	$B_6^4$
susc. fit	-0.557	-0.041	0.261	-0.0009	0.0011
first princ.	-1.03	0.0064	-0.0028	-0.0005	0.0115
Energies (K) (doublets)					
susc. fit	0	40.5	100.4	180.9	259.8
first princ.	0	14.5	82.5	122.4	180.6

Ground states:

$$|\psi_1^{\text{susc.fit}}\rangle = 0.895 |\pm 9/2\rangle - 0.431 |\pm 1/2\rangle + 0.11 |\mp 7/2\rangle$$

$$|\psi_1^{\text{first p.}}\rangle = -0.860 |\pm 9/2\rangle + 0.502 |\pm 1/2\rangle - 0.09 |\mp 7/2\rangle$$

Table 4.5: Comparison of the CF parameters, energies and ground states as obtained by susceptibility fitting and first-principles calculations.

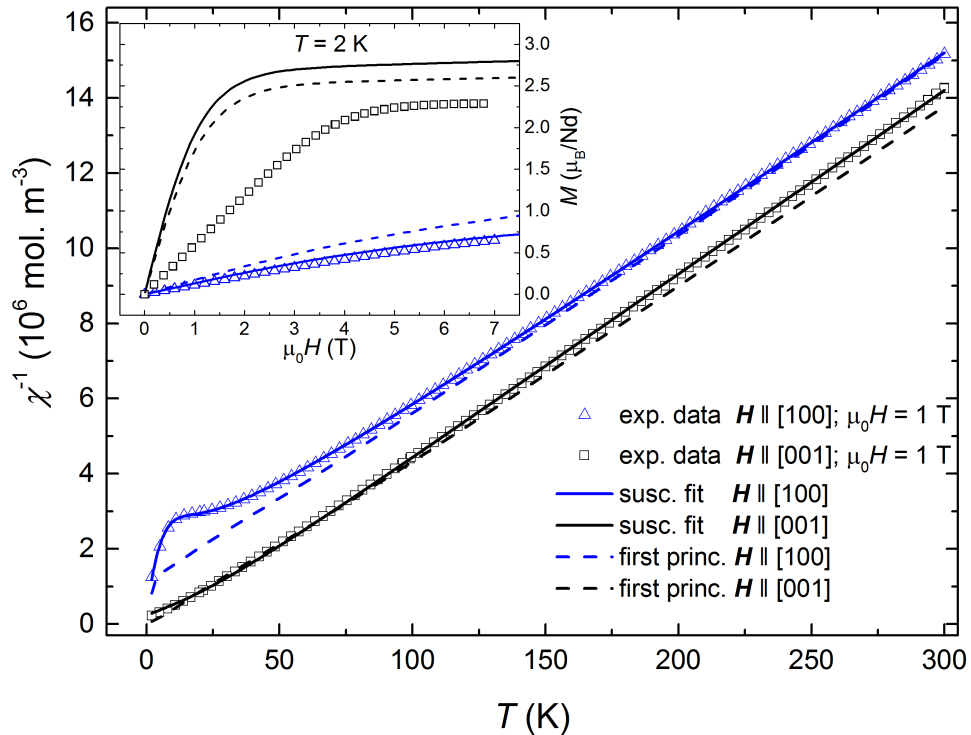


Figure 4.16: Fit of the experimental  $M/H$  vs.  $T$  data to relation (1.31) compared to the susceptibility calculated from the first-principles CF parameters (Table 4.5). The inset presents experimental  $M(H)$  data and calculated magnetization without molecular field contribution as resulting from the CF parameters obtained by susceptibility fitting and from first principles.

## 4.6.2 Inelastic neutron scattering

To investigate CF excitations in  $\text{NdPd}_5\text{Al}_2$  thoroughly, the INS experiment has been undertaken at the ILL Grenoble employing IN4C time-of-flight spectrometer (see Section 2.3.2). For the measurement we have used powderized polycrystalline sample of the total mass of 12.3 g which was wrapped into aluminium foil. Since the  $^4\text{I}_{9/2}$  ground state of  $\text{Nd}^{3+}$  ion splits into 5 Kramers doublets in the tetragonal CF, we expected to observe in INS spectra four transitions from the CF ground state to excited states at lowest temperatures alongside other transitions between excited states which appear as these states get thermally populated. For clarity, we will refer to these doublets with Greek numbers I, II,  $\dots$ , V from the lowest lying to the highest and to transitions between them as I $\rightarrow$ II etc. In order to identify these transitions unambiguously and to be able to reconstruct CF energy-level scheme completely, we have carried out measurements of the INS spectra at various different temperatures (in the paramagnetic state) and at several incident neutron energies. Generally, higher incident energies allow to cover wider range of the CF excitation spectrum, but at the expense of lower energy resolution, so switching to lower incident energies is necessary to examine more subtle details. Scattering function  $S(Q, E)$  which is obtained in the INS experiment involves inherently, besides non-dispersive CF excitations, also other contributions to scattering, e. g. elastic Bragg peaks or a scattering from low-lying phonons which emerge at higher temperatures typically at higher scattering angles as a relatively broad dispersive signal. Since we were interested primarily in inelastic scattering due to the CF which is of a magnetic origin and thus decreases with increasing wavevector transfer as  $\approx f(Q)^2$  and since we have not performed measurements on a non-magnetic analogue for subtraction of the non-magnetic signal, we have always summed  $S(Q, E)$  over lower scattering angles only up to  $90^\circ$  to prevent from involving phonons (let us remind that the full range of  $Q$  corresponds to scattering angles up to  $120^\circ$ ). Resulting quantity is presented as intensity (in arbitrary units) in the following.

Figure 4.17 shows scattering functions  $S(Q, E)$  at selected temperatures from 2 K to 80 K taken at the incident neutron energy  $E_i = 28.9$  meV. Corresponding INS spectra are presented in the Fig. 4.18. At the lowest measured temperature, namely at 2 K, we have observed a transition at 17.1 meV and another broader peak around 8.5 meV. While magnitudes of these two peaks are gradually decreasing with increasing temperature, another two peaks arise at 14.1 meV and  $\sim 5$  meV developing rapidly between 10 K and 40 K. This suggests that the former two peaks can presumably correspond to excitations from the ground state, whereas the latter two might be related to transitions from the first excited doublet as it gets thermally populated. In addition, we have observed intensities at energy transfers  $\sim 5$  meV and  $\sim 8.5$  meV symmetrically also in the negative (neutron-gain) part of the spectrum (see Fig. 4.18) which is related to the positive part by the principle of detailed balance [77] and thus it carries similar information.

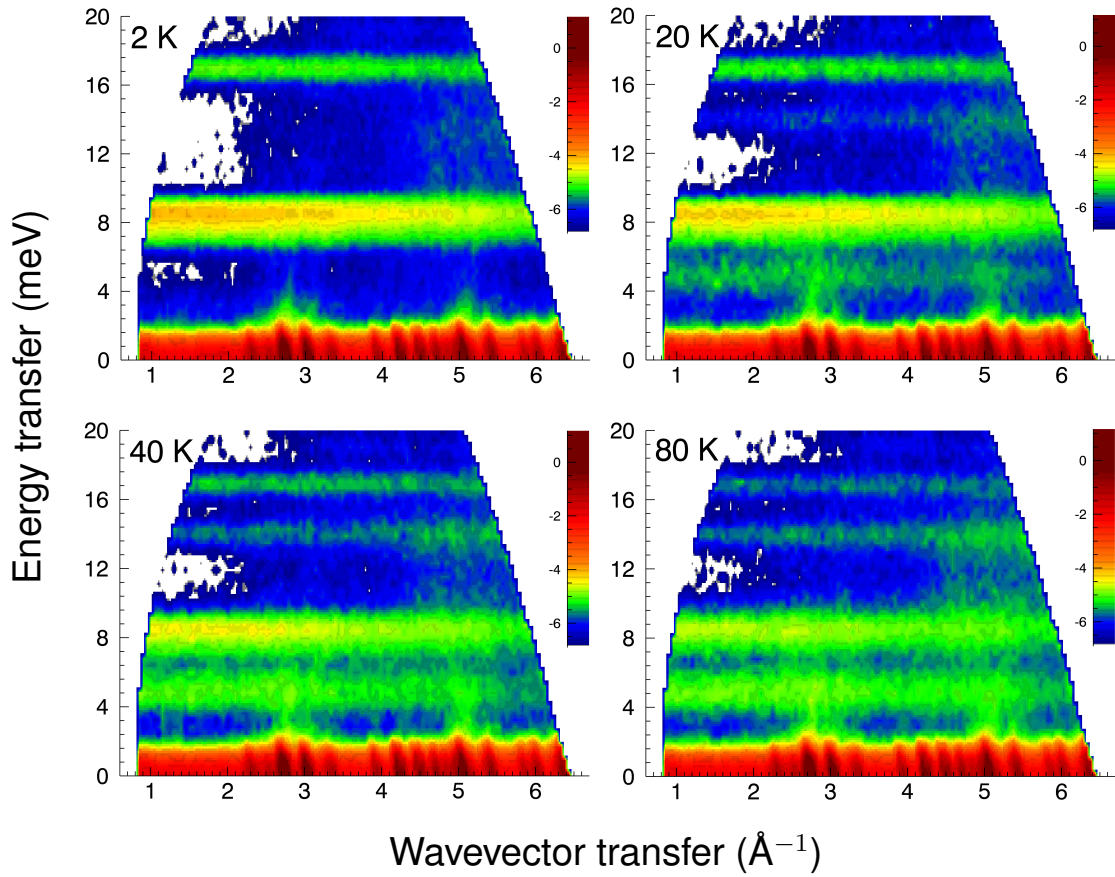


Figure 4.17: Scattering function  $S(Q, E)$  in logarithmic representation at several temperatures and for incident neutron energy  $E_i = 28.9$  meV.

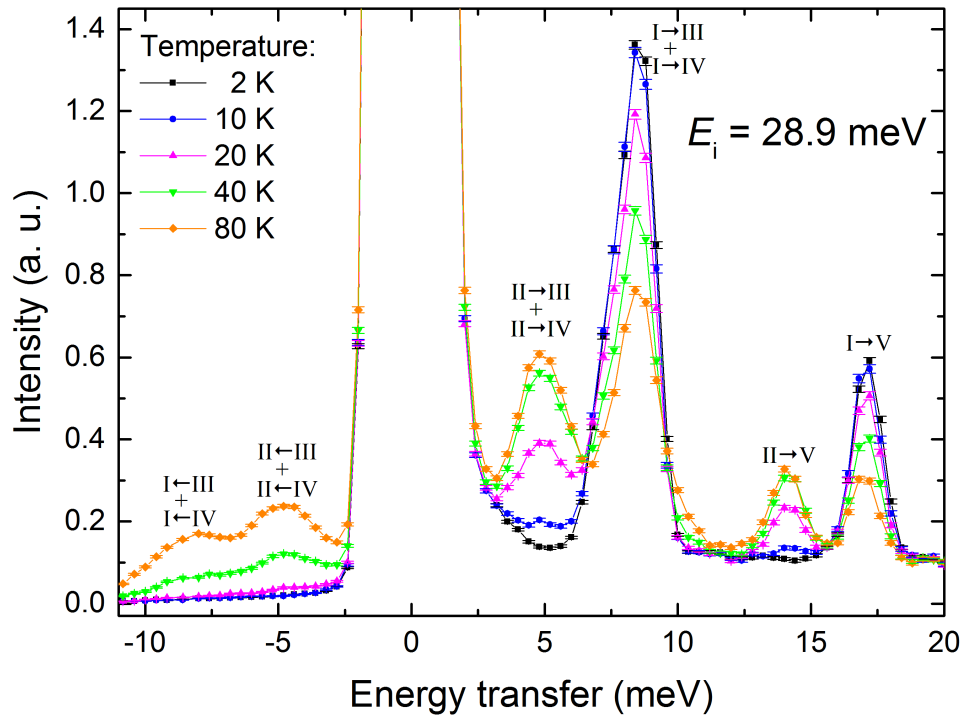


Figure 4.18: INS spectrum taken at incident neutron energy  $E_i = 28.9$  meV. We refer to the CF energy-level scheme (Fig. 4.21) and to the discussion in the text for the better understanding of indicated transitions.

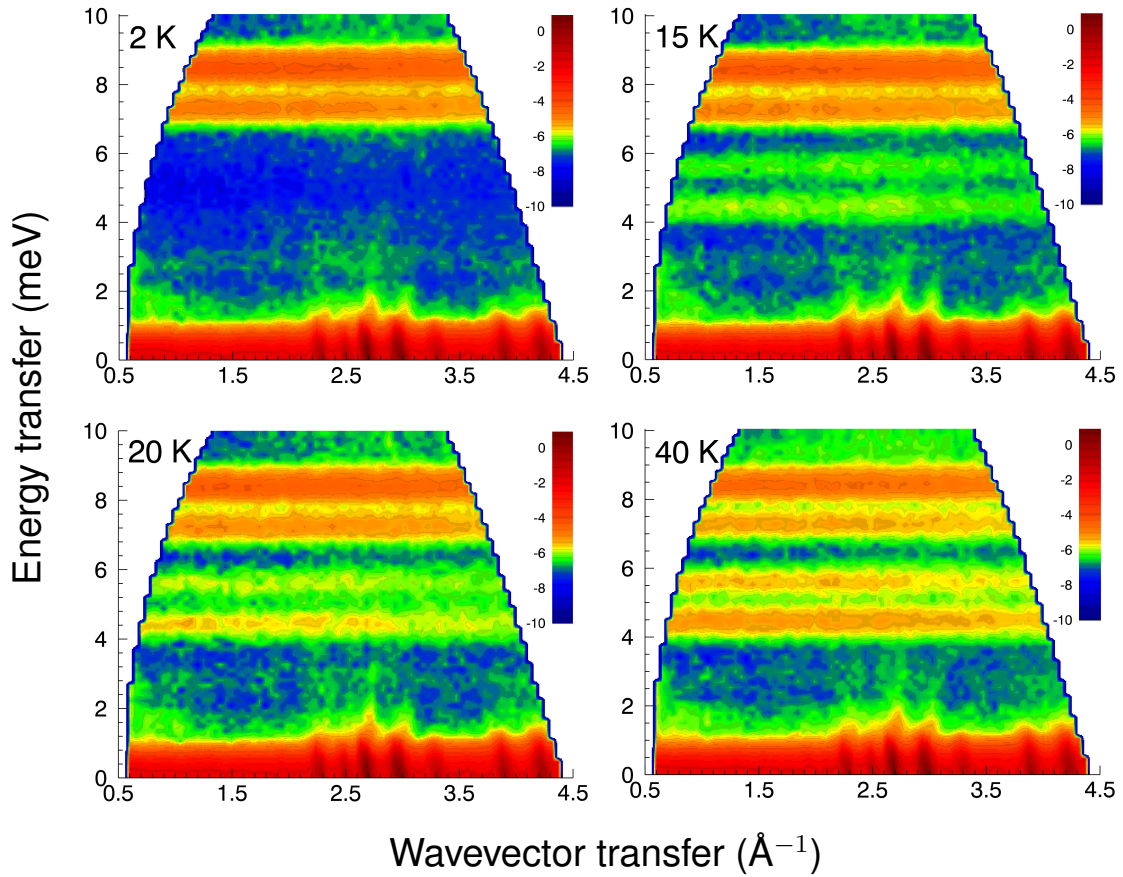


Figure 4.19: Scattering function  $S(Q, E)$  in logarithmic representation at several temperatures and for incident neutron energy  $E_i = 13.7$  meV.

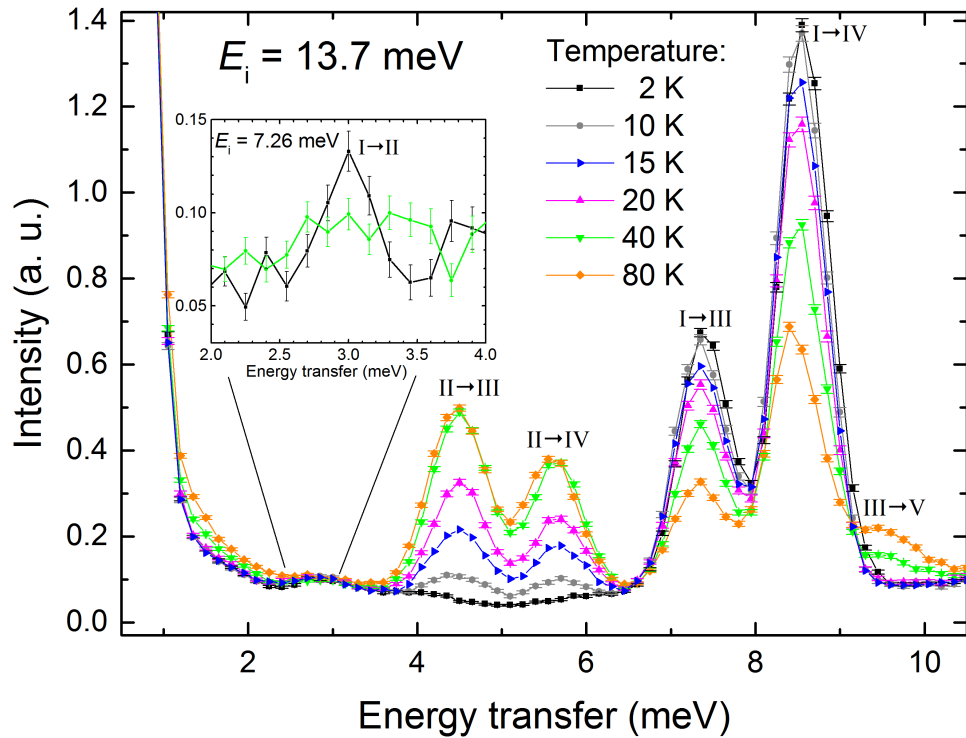


Figure 4.20: INS spectrum taken at incident neutron energy  $E_i = 13.7$  meV and at various temperatures. Refer to Fig. 4.21 for the CF energy-level scheme.

We continued with measurement using  $E_i = 13.7$  meV at the same temperature range 2-80 K to explore further aspects of the CF. As can be seen in contour graphs of  $S(Q, E)$  and associated INS spectra (Figs. 4.19 and 4.20), it has been revealed that each of the broad peaks appearing at  $\sim 8.5$  meV and  $\sim 5$  meV in the previous measurement in fact consists of two peaks at 7.4 meV and 8.6 meV, respectively at 4.4 meV and 5.6 meV. The argument about temperature development from the previous paragraph remains still valid and thus peaks at 7.4 meV and 8.6 meV might be attributed to CF excitations from the ground state doublet and those at 4.4 meV and 5.6 meV from the first excited doublet to higher states. Moreover, it might be noticed that energies 7.4 meV and 8.6 meV are shifted by the factor of 3 meV ( $\sim 35$ K) with respect to 4.4 meV and 5.6 meV pointing to the position of the first excited doublet which would be in a good agreement with its position as preliminary determined by the susceptibility fitting (i. e.  $\sim 40$  K). Corresponding excitation from the ground state to the first excited state has been really clearly observed at 3.0 meV when using  $E_i = 7.26$  meV as can be seen in the inset of the Fig. 4.20, although the peak is of a very small intensity.

By combining measurements with  $E_i = 7.26$  meV,  $E_i = 13.7$  meV and  $E_i = 28.9$  meV at 2 K we are consequently able to identify all excitations from the ground state as presented in Fig. 4.21. They are located at 3.0 meV (I $\rightarrow$ II), 7.4 meV (I $\rightarrow$ III), 8.6 meV (I $\rightarrow$ IV) and 17.1 meV (I $\rightarrow$ V). Consistently with this, we also observed transitions II $\rightarrow$ V at 14.1 meV (Fig. 4.18), II $\rightarrow$ III at 4.4 meV, II $\rightarrow$ IV at 5.6 meV and presumably III $\rightarrow$ V emerging around 9.7 meV (Fig. 4.20). This allows us to complete CF energy-level scheme of NdPd<sub>5</sub>Al<sub>2</sub> as presented in Fig. 4.21 (right panel).

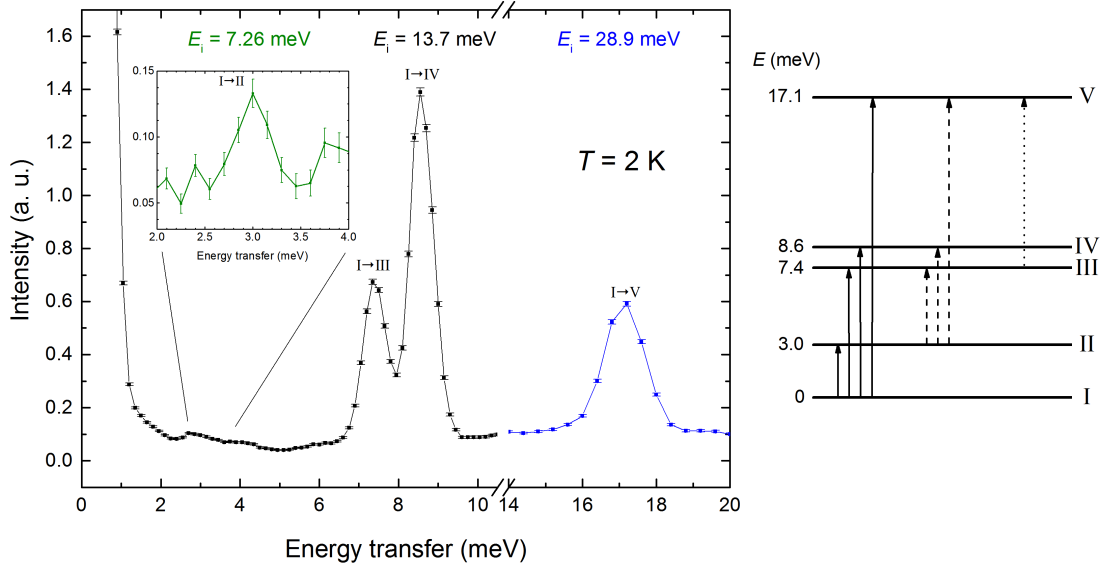


Figure 4.21: INS spectrum at 2 K obtained by combining measurements at incident 7.26, 13.7 and 28.9 meV show all four transitions from the ground state (left). Right panel shows CF energy-level scheme of NdPd<sub>5</sub>Al<sub>2</sub>. Transitions from the ground state (full lines), first and second excited state (dashed, respectively dotted lines) observable in the INS spectra are indicated.

### 4.6.3 Energy-level scheme and specific heat

To conclude our findings about the CF in  $\text{NdPd}_5\text{Al}_2$ , we compare the CF energies directly measured in the INS experiment with those obtained by the susceptibility fitting and first-principles calculations (Figure 4.22), calculate corresponding Schottky specific heat (1.43) and discuss them with respect to the experimental magnetic specific heat. Although that CF energy-level schemes tentatively determined by these two indirect methods do not correspond accurately to that actually measured in the INS experiment, they also show some qualitative similarities: The overall CF splitting evaluated by the first-principles calculations  $\approx 180$  K is similar to the real splitting  $\approx 200$  K, but it does not determine correctly energy of the first excited doublet leading to the Schottky specific heat presenting 2 maxima contrary to the experimental data (see Fig. 4.23).

On the other hand, susceptibility fitting allowed us to correctly estimate the energy of this first excited and also approximately (with  $\sim 10\%$  accuracy) of the second excited doublet, but the estimated position of higher states is seemingly burdened with a substantial error and thus unreliable. Schottky anomaly resulting from the fit (Fig. 4.23) exhibits then a relatively broad maximum around 40 K, i. e. close to the extremal value of the Schottky contribution to the experimental magnetic specific heat. However, maximum of the Schottky specific heat as resulting from energies determined by the INS lies at 25 K. Discrepancy between this curve and experimental data might be ascribed to the manner of necessary estimation of magnetic specific heat under the absence of a proper non-magnetic analogue as was discussed in Section 4.4. Since the INS scattering is a direct method of determination of the CF levels, we put more emphasis on credibility of Schottky specific heat calculated using energies obtained from this experiment.

Let us note here that we also tried to directly analyse INS spectra to obtain CF parameters which would reasonably describe both intensities of measured CF transitions as well as observed CF energies and which would lead to a reasonable interpretation of experimental magnetic specific heat and magnetization data. We would be then not only able to compare this set of CF parameters with those already available from susceptibility fitting and first-principles calculations, which as we already know do not reproduce CF energies accurately, but also discuss the nature of actual CF states in  $\text{NdPd}_5\text{Al}_2$  in detail. Having to face several serious difficulties, e. g. that is possible to find several different sets of CF parameters leading to the similar energies, our efforts in finding of such set of CF parameters were so far fruitless.

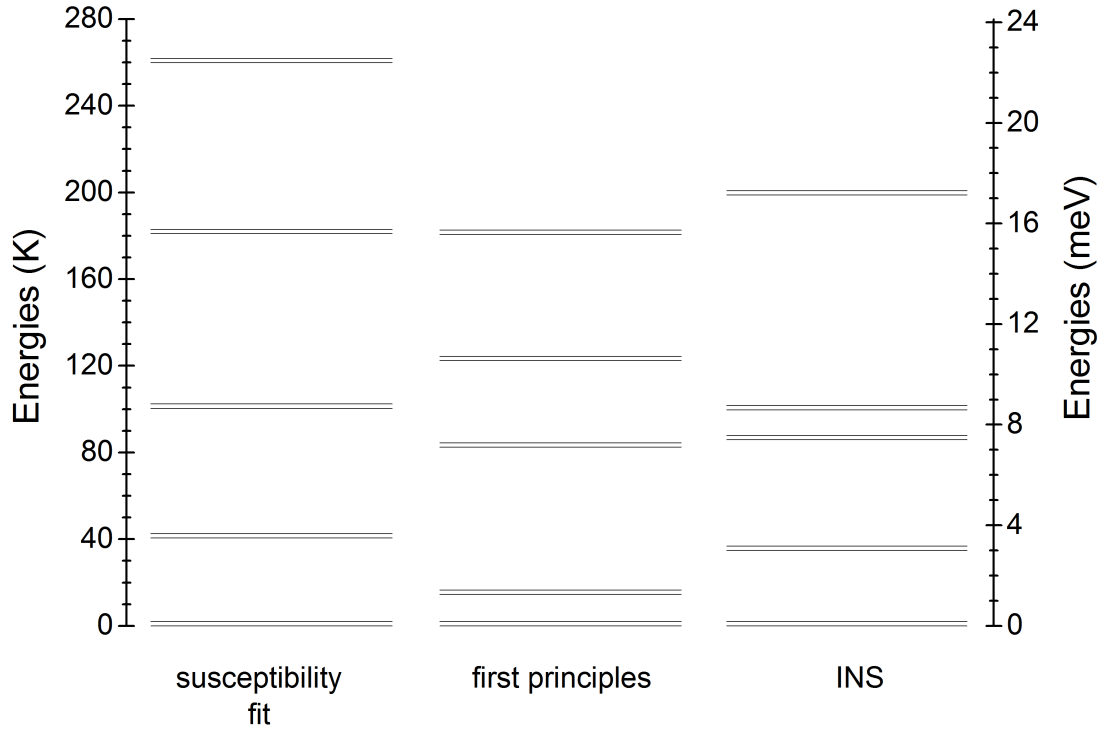


Figure 4.22: Comparison of the proposed CF energy-level schemes in  $\text{NdPd}_5\text{Al}_2$  as evaluated by the susceptibility fitting and first-principles calculations with the CF energies measured in the INS experiment.

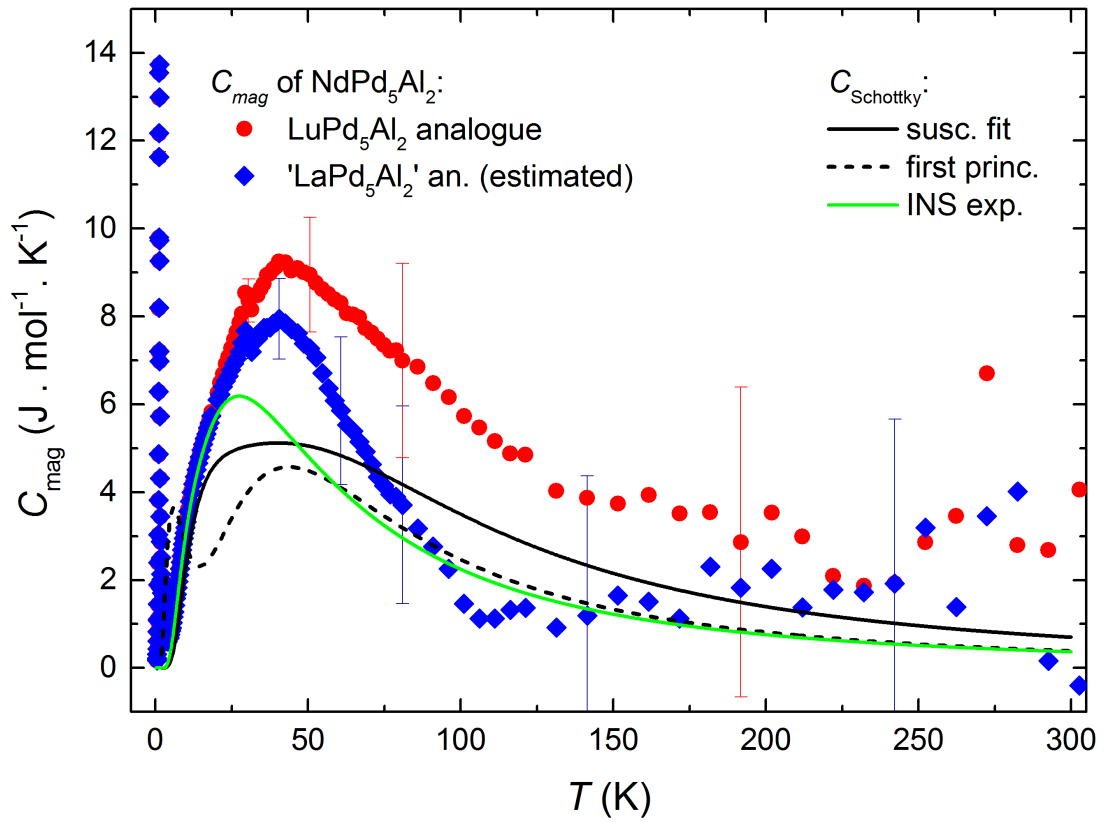


Figure 4.23: Magnetic specific heat of  $\text{NdPd}_5\text{Al}_2$  evaluated using non-magnetic analogues and Schottky contributions to the specific heat as resulting from CF energy levels (Fig. 4.22) obtained by three different methods.

## 4.7 Discussion

We have investigated thoroughly the intermetallic  $\text{NdPd}_5\text{Al}_2$  compound by means of bulk specific heat and magnetization measurements, neutron diffraction and inelastic neutron scattering.  $\text{NdPd}_5\text{Al}_2$  crystallizes in the tetragonal  $\text{ZrNi}_2\text{Al}_5$ -type structure (space group  $I4/mmm$ ) with lattice parameters  $a = 4.147 \text{ \AA}$  and  $c = 14.865 \text{ \AA}$  and orders magnetically below  $T_N = 1.3 \text{ K}$ .

The magnetic phase diagram of  $\text{NdPd}_5\text{Al}_2$  (Fig. 4.9) has been constructed on the basis of specific heat and  $M(H)$  measurements in the field applied along the tetragonal  $c$ -axis. It features two distinct magnetically ordered phases. The zero-field phase is a collinear antiferromagnet with the magnetic structure described by the propagation vector  $\mathbf{k} = (\frac{1}{2}00)$  and magnetic moments oriented along the  $[001]$  direction as was demonstrated by the neutron diffraction in Section 4.5.1. The transition to the another field-induced phase is accompanied, alongside the anomaly in the specific heat (Figs. 4.6 and 4.8), with the rapid increase of magnetization (Fig. 4.5). The existence of two magnetic phases resembles phase diagrams of related  $RTX_5$  and  $R_2TX_8$  [50, 54, 56, 58, 78]. The shape of the border between both phases is similar to that found in  $R_2\text{CoGa}_8$  series [54], while somewhat distinguishes from those published for  $RRh\text{In}_5$  [50, 78] and  $R_2\text{RhIn}_8$  compounds [56, 58], see Fig. 3.2. The microscopic nature of both magnetic phases has been thoroughly studied by neutron diffraction in the case of  $\text{Ho}_2\text{RhIn}_8$  [57]. In both magnetic phases here, the rare-earth moments are oriented parallel along the  $c$ -axis. The ground state magnetic structure of  $\text{Ho}_2\text{RhIn}_8$  is a simple collinear antiferromagnet characterized by the propagation vector  $\mathbf{k} = (\frac{1}{2}00)$ , similarly to  $\text{NdPd}_5\text{Al}_2$ . The magnetic structure in the field-induced phase is then a complex multi- $k$  structure described by four propagation vectors. The transition between both phases can be simply viewed also as flipping of one quarter of the Ho magnetic moments which causes the total magnetization to be half of the field-induced ferromagnetic state value [57]. In the case of  $\text{NdPd}_5\text{Al}_2$ , the magnetization (Fig. 4.5) after the first transition reaches  $\approx 1.2 \mu_B/\text{Nd}$  which is roughly half of the saturated value presented in the Figure 4.4, i.e. we observe the same behaviour as reported for  $R_2\text{RhIn}_8$  compounds including  $\text{Ho}_2\text{RhIn}_8$  [56, 58]. Such similarity together with a closely related crystal structure indicates possibly the same nature of the phase transition between the two magnetic phases also in  $\text{NdPd}_5\text{Al}_2$ .

Interestingly, analysis of the heating pulses (inset of Fig. 4.9) revealed first-order character of the transition from the paramagnetic to the antiferromagnetic phase. First-order phase transition in zero field is rather unusual for transition between paramagnetic and magnetically ordered state and for the  $R_2\text{CoGa}_8$  compounds [54] exhibiting similar phase diagram has not been reported, but it was observed in several cases, for instance by the antiferromagnetic compounds  $\text{U}_2\text{Rh}_3\text{Si}_5$  [79, 80] and  $\text{EuSn}_3$  [81]. Common feature of these two compounds is, besides non-trivial ground-state magnetic structure, that both exhibit step-like changes of lattice parameters at  $T_N$ . Another compound presenting first-order phase transition between paramagnetic and antiferromagnetic state,  $\text{Dy}_3\text{Ru}_4\text{Al}_{12}$  [82, 83], shows whilst only small orthorhombic distortion at  $T_N$  indicating presumably different driving mechanism behind the first-order phase transition than the previous two. Regarding these results, an experiment following the develop-

ment of the crystal lattice of  $\text{NdPd}_5\text{Al}_2$  across the  $T_N$ , e. g. thermal expansion or low-temperature XRD, would be desirable to reveal more precise details about nature of the transition in our case. Another tentative explanation of the behaviour observed by  $\text{NdPd}_5\text{Al}_2$  might be the fact that the phase 2 region in the phase diagram reaches down to the zero field (dotted line in Figure 4.9) or due to possible presence of some other magnetic phase existing only in a very narrow temperature range as in the case of  $\text{Ho}_2\text{RhIn}_8$  [57]. The first-order character of the transition seen in low fields arises then from transition between this phase (or phase 2) and phase 1.

In Section 4.6, we presented our findings about the CF in  $\text{NdPd}_5\text{Al}_2$  comparing results obtained by susceptibility fitting, INS and first-principles calculations. Analysis of experimental susceptibilities for  $H \parallel [001]$  and  $H \perp [001]$  measured on a single crystalline sample is a common method of determination of CF parameters, e. g. [51, 54]. In other cases [84, 85], CF parameters were obtained from the INS and then confronted only with the polycrystalline susceptibility data which comprise only averaged information about the magnetocrystalline anisotropy caused by CF. Nevertheless, comprehensive cross-validation of the obtained results is usually missing, mostly either due to the absence of proper single crystals for anisotropic susceptibility measurements or due to the limited size of often exclusively flux-grown samples for which the INS experiment is not reasonably feasible. As an exception to this, we may mention the work of Blanco [86]. However, even when using both INS and single-crystal susceptibilities for the CF parameters refinement, the author was still able to find several distinct sets of these parameters well-describing his data as he illustrated on the example of the tetragonal  $\text{HoAg}_2$  compound. This suggests that CF parameters, in particular those of higher order and especially determined from susceptibility fitting only, do not always have to be completely reliable and thus meaningfully interpretable. Generally, the most powerful technique which could help to determine a unique set of CF parameters in such cases unambiguously would be INS employing polarization analysis and single crystalline samples<sup>‡</sup>, where the averaging Eq. (2.7) does not apply and matrix elements of particular components of the total angular momentum corresponding to transition between CF eigenstates are directly observable [87].

In regard to compounds from the  $\text{RPd}_5\text{Al}_2$  series, CF parameters obtained by susceptibility fitting have been reported for  $\text{PrPd}_5\text{Al}_2$  [27] and  $\text{CePd}_5\text{Al}_2$  [27, 61] compounds.  $\text{CePd}_5\text{Al}_2$ <sup>§</sup> was subsequently studied also by means of INS [63] revealing CF excitations at 21.3 meV (=247 K) and 22.4 meV (=260 K) and somewhat different set of CF parameters from the previous two, the results are compared in Table 4.6. As can be noticed in Fig. 4.24, both sets of CF parameters reported by Nakano et al. [27] and Onimaru et al. [61] reproduce well the susceptibility data whilst they lead to somewhat different energies of excited CF states i. e. 230 K and 300 K, respectively 247 K and 260 K. Parameters obtained by Inoue from the INS experiment lead reportedly reproduced experimental susceptibilities sufficiently as well [63]. Not intending to speculate about the source of discrepancies, we wanted to demonstrate possibilities and accuracy

---

<sup>‡</sup>with already mentioned limitations given by sample size/technical possibilities of neutrons

<sup>§</sup>Let us note that determination of the CF parameters is in the case of Ce simplified by the fact, that only 3 from 5 CF parameters for tetragonal symmetry apply.

Table 4.6: CF parameters for  $\text{CePd}_5\text{Al}_2$  and corresponding energies as reported by different authors.

author	ref.	method	$B_2^0$ (K)	$B_4^0$ (K)	$B_4^4$ (K)	$E_i$ (K) (doublets)
Nakano et al.	[27]	susc.	-12	-0.1	1.9	0 197 224
Onimaru et al.	[61]	susc.	-16.4	-0.071	1.56	0 230 300
Inoue et al.	[63]	INS	-13.28	-0.15	2.94	0 247 260

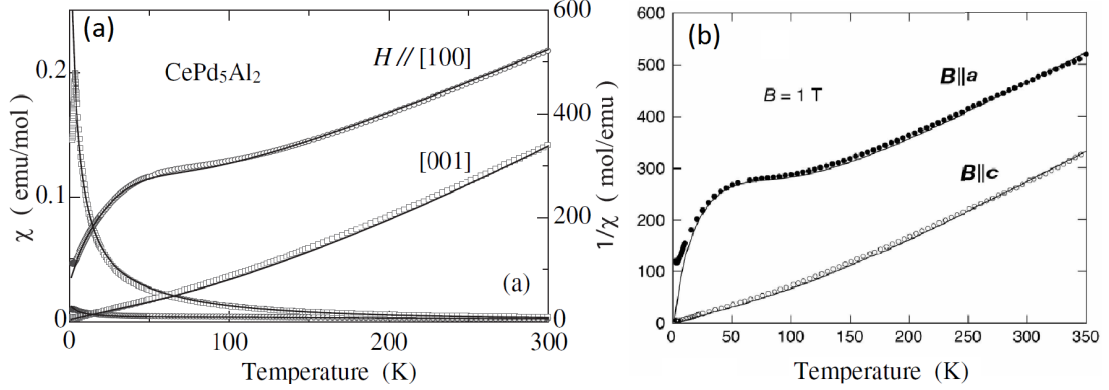


Figure 4.24: Susceptibility of  $\text{CePd}_5\text{Al}_2$  and fits (full lines) leading to the CF parameters in Table 4.6 as reported by (a) Nakano et al. [27] and (b) Onimaru et al. [61]. Discussion in the text.

of susceptibility fitting as a technique of determination of CF parameters here.

In our case of  $\text{NdPd}_5\text{Al}_2$ , susceptibility analysis indicated parameters presented in Table 4.4. The obtained value of the leading CF parameter  $B_2^0 = -0.557$  K  $<$  0 is consistent with the  $c$ -axis as the easy axis of magnetization presenting the same type of anisotropy as  $\text{CePd}_5\text{Al}_2$ . Expressing this parameter in terms of CF parameters  $A_l^m$  (1.19), whose values are more appropriate when comparing CF effects on different rare-earth ions (since they do not involve ion-dependent multiplicative coefficients) and assuming  $\langle r^2 \rangle = 0.3120$  Å for Nd [24], we will get  $A_2^0 \approx 280$  K/Å<sup>2</sup> which is lower than  $A_2^0 \approx 600 - 800$  K/Å<sup>2</sup> resulting from parameters  $B_2^0$  for  $\text{CePd}_5\text{Al}_2$  as listed in the Table 4.6. For related  $\text{NdRhIn}_5$  compound, Hieu et. al. reported a value of the parameter  $B_2^0 = -1.21$  K [51]. This set of CF parameters for  $\text{NdPd}_5\text{Al}_2$  obtained from susceptibilities leads to 5 Kramers doublets at 0, 40, 100, 180 and 260 K. The subsequent INS experiment presented in Section 4.6.2 has shown CF excitations at 3.0 meV ( $\approx 35$  K), 7.4 meV ( $\approx 86$  K), 8.6 meV ( $\approx 100$  K) and 17.1 meV ( $\approx 198$  K), for comparison of the CF energy-level schemes see Fig. 4.22. Although we were not able to reproduce the CF energy-level scheme of  $\text{NdPd}_5\text{Al}_2$  from these parameters completely, we were, within the precision of the method (with similar results as in the mentioned case of  $\text{CePd}_5\text{Al}_2$ ), able to sketch some of its features, e. g. estimate the energy of the first excited doublet and, with lower accuracy, approximate position of the higher CF states which allowed us to produce a Schottky curve in reasonable agreement with the experimental data (Fig. 4.23). We suppose thus, that determination of the CF parameters from susceptibility fit as it was presented has, despite mentioned disadvantages, its significance and it can be well-employed in the CF analysis when complemented by other techniques.

# 5. Conclusion

We have investigated thoroughly the intermetallic  $\text{NdPd}_5\text{Al}_2$  compound by means of bulk specific heat and magnetization measurements, neutron diffraction and inelastic neutron scattering.  $\text{NdPd}_5\text{Al}_2$  crystallizes in the tetragonal  $\text{ZrNi}_2\text{Al}_5$ -type structure (space group  $I4/mmm$ ) with lattice parameters  $a = 4.147 \text{ \AA}$  and  $c = 14.865 \text{ \AA}$ . The compound orders magnetically below  $T_N = 1.3 \text{ K}$  and presents large magnetocrystalline anisotropy due to the crystal-field effects.

The magnetic phase diagram of  $\text{NdPd}_5\text{Al}_2$  has been constructed on the basis of specific heat and  $M(H)$  measurements in the field applied along the tetragonal  $c$ -axis. It features two distinct magnetically ordered phases - ground-state antiferromagnetic phase and another field-induced phase, similarly to related tetragonal  $R_2TX_5$  and  $R_2TX_8$  compounds.

The nature of the zero-field antiferromagnetic phase has been studied in detail by means of neutron diffraction. It has been established that the magnetic structure is characterized by the commensurate propagation vector  $\mathbf{k} = (\frac{1}{2}00)$  and magnetic moments are oriented parallel to the  $[001]$  direction with resulting amplitude of magnetic moments  $2.22 \mu_B$  per Nd ion.

The analysis of the heating pulses has revealed the first-order character of the phase transition from paramagnetic to antiferromagnetic phase in the zero field due to the presence of latent heat. Such behaviour is rather unusual for the phase transition from paramagnetic to magnetically ordered phase and for the  $R_2TX_8$  compounds exhibiting analogical magnetic phase diagrams [54] has not been reported.

The tetragonal CF splits the  $4I^{9/2}$  ground state of  $\text{Nd}^{3+}$  ions into 5 Kramers doublets and influences fundamentally the magnetocrystalline anisotropy. To investigate its effects in  $\text{NdPd}_5\text{Al}_2$ , we have employed following three different techniques: susceptibility fitting, first-principles calculations and inelastic neutron scattering. Susceptibility fit resulted into a set of CF parameters reproducing well the experimental data for both  $H \parallel [001]$  and  $H \parallel [100]$  and indicated the value of the leading CF parameter  $B_2^0 = -0.557 \text{ K}$  which corresponds to the tetragonal  $c$ -axis as the easy direction of magnetization. It allowed us to correctly approximate the energy of the first excited CF doublet as 40 K and estimate higher CF levels as 100, 180 and 260 K leading into Schottky specific heat which was in qualitative agreement with the experimental magnetic specific heat. On the contrary, while susceptibilities calculated from the first-principles CF parameters followed approximately the experimental susceptibility data at high temperatures, at low temperatures discrepancies were observable both in susceptibility and Schottky specific heat due to the inaccurate position of the first excited doublet. Subsequent INS experiment, which enables direct observation of crystal field excitations, revealed their positions in  $\text{NdPd}_5\text{Al}_2$  at energies 35 K, 86 K, 100 K and 198 K. Disagreement from CF energy-level scheme proposed using CF parameters determined by susceptibility fit was registered at higher energies. This suggests that actual values of CF parameters for  $\text{NdPd}_5\text{Al}_2$  might be different from those obtained by the susceptibility fit. Their precise evaluation which would allow us coherent a interpretation of magnetization, magnetic specific data as well as INS spectra will be the matter of future studies.

# Bibliography

1. HEGGER, H.; PETROVIC, C.; MOSHOPOULOU, E. G., et al. Pressure-Induced Superconductivity in Quasi-2D CeRhIn<sub>5</sub>. *Phys. Rev. Lett.* 2000, vol. 84, pp. 4986–4989. Available also from WWW: (<http://link.aps.org/doi/10.1103/PhysRevLett.84.4986>).
2. PETROVIC, C; PAGLIUSO, P. G.; HUNDLEY, M. F., et al. Heavy-fermion superconductivity in CeCoIn<sub>5</sub> at 2.3 K. *Journal of Physics: Condensed Matter.* 2001, vol. 13, no. 17, pp. L337. Available also from WWW: (<http://stacks.iop.org/0953-8984/13/i=17/a=103>).
3. NICKLAS, M.; SIDOROV, V. A.; BORGES, H. A., et al. Magnetism and superconductivity in Ce<sub>2</sub>RhIn<sub>8</sub>. *Phys. Rev. B.* 2003, vol. 67, pp. 020506. Available also from WWW: (<http://link.aps.org/doi/10.1103/PhysRevB.67.020506>).
4. AOKI, D.; HAGA, Y.; D. MATSUDA, T., et al. Unconventional heavy-fermion superconductivity of a new transuranium compound NpPd<sub>5</sub>Al<sub>2</sub>. *Journal of the Physical Society of Japan.* 2007, vol. 76, no. 6, pp. 063701. Available also from WWW: (<http://dx.doi.org/10.1143/JPSJ.76.063701>).
5. ALMEIDA RIBEIRO, R. de; ONIMARU, T.; UMEO, K., et al. A Kondo lattice antiferromagnet CePd<sub>5</sub>Al<sub>2</sub>. *Journal of the Physical Society of Japan.* 2007, vol. 76, no. 12, pp. 123710. Available also from WWW: (<http://dx.doi.org/10.1143/JPSJ.76.123710>).
6. HONDA, F.; MEASSON, M.-A.; NAKANO, Y., et al. Pressure-induced superconductivity in antiferromagnet CePd<sub>5</sub>Al<sub>2</sub>. *Journal of the Physical Society of Japan.* 2008, vol. 77, no. 4, pp. 043701. Available also from WWW: (<http://dx.doi.org/10.1143/JPSJ.77.043701>).
7. KLÍMA, J.; VELICKÝ, B. *Kvantová mechanika II*. Praha: SPN, 1990. ISBN 80-7066-185-2.
8. NEKVASIL, V.; DIVIŠ, M. Localized 4*f* and 5*f* Moments: Magnetism. In *Encyclopedia of Materials: Science and Technology*. Second Edition. Oxford: Elsevier, 2001, pp. 4613–4627. Available also from WWW: (<http://www.sciencedirect.com/science/article/pii/B0080431526008068>). ISBN 978-0080431529.
9. MAJLIS, N. *The quantum theory of magnetism*. 2nd ed. Singapore: World Scientific, 2000. ISBN 978-9812567925.
10. JENSEN, J.; MACKINTOSH, A. R. *Rare earth magnetism*. Oxford: Clarendon Press, 1991. Available also from WWW: (<http://www.fys.ku.dk/~jjensen/Book/Ebook.pdf>). ISBN 978-0198520276.
11. BUSCHOW, K. H. J.; BOER, F. R., et al. *Physics of magnetism and magnetic materials*. New York: Kluwer Academic Publishers, 2004. ISBN 0-306-48408-0.
12. ASHCROFT, N. W.; MERMIN, N. D. *Solid state physics*. 1976. ISBN 978-0030839931.
13. KITTEL, C. *Úvod do fyziky pevných látek*. 1st ed. 1985.
14. COEY, J. M. D. *Magnetism and magnetic materials*. Cambridge: Cambridge University Press, 2010. ISBN 978-0511677434.

15. BETHE, H. A. Splitting of terms in crystals. *Ann. Physik.* 1929, vol. 3, no. 5, pp. 133.
16. AMARA, M. *Crystal field effect on atomic states*. Ecole Thématique: Apport des symétries en matière condensée, Giens 2009. Available also from WWW: <http://neel.cnrs.fr/spip.php?rubrique1021>.
17. KRAMERS, H. A. Théorie générale de la rotation paramagnétique dans les cristaux. *Proc. Acad. Amst.* 1930, vol. 33, pp. 959–972.
18. HUTCHINGS, M. T. Point-Charge Calculations of Energy Levels of Magnetic Ions in Crystalline Electric Fields\*. 1964, vol. 16, pp. 227–273. Available also from WWW: <http://www.sciencedirect.com/science/article/pii/S0081194708605172>. ISSN 0081-1947.
19. STEVENS, K. W. H. Matrix Elements and Operator Equivalents Connected with the Magnetic Properties of Rare Earth Ions. *Proceedings of the Physical Society. Section A.* 1952, vol. 65, no. 3, pp. 209. Available also from WWW: <http://stacks.iop.org/0370-1298/65/i=3/a=308>.
20. NEWMAN, D. J.; NG, B. *Crystal field handbook*. New York: Cambridge University Press, 2007. ISBN 978-0521039369.
21. JACKSON, J. D. *Classical Electrodynamics*. 1st ed. New York: John Wiley & Sons, Inc., 1962. ISBN 978-0471431312.
22. ROTTER, M. *McPhase USERS MANUAL: Tesseral Harmonics* [online]. 2013-09-19 [visited on 2016-03-19]. Available from WWW: [http://www2.cpfs.mpg.de/~rotter/homepage\\_mcphase/manual/node131.html](http://www2.cpfs.mpg.de/~rotter/homepage_mcphase/manual/node131.html).
23. ABRAGAM, A; BLEANEY, B. *Electron paramagnetic resonance of transition ions*. Oxford: Clarendon Press, 1970.
24. BAUER, E.; ROTTER, M. *Magnetism of complex metallic alloys: crystalline electric field effects*. 2007. A script for a lecture given at the CMA Euroschool 2007, Ljubljana, Slovenia.
25. MOZE, O. Crystal Field Effects in Intermetallic Compounds: Inelastic Neutron Scattering Results. In *Concise Encyclopedia of Magnetic & Superconducting Materials*. 2nd ed. Oxford: Elsevier, 2005, pp. 95–100. ISBN 978-0-080445861.
26. HIEU, N. V. *Single Crystal Growth and Magnetic Properties of RRhIn<sub>5</sub> Compounds (R: Rare Earths)*. 2007. Doctoral thesis. Osaka University. Osaka.
27. NAKANO, Y.; HONDA, F.; TAKEUCHI, T., et al. Magnetic and Fermi Surface Properties of CePd<sub>5</sub>Al<sub>2</sub> and PrPd<sub>5</sub>Al<sub>2</sub>. *Journal of the Physical Society of Japan*. 2010, vol. 79, no. 2, pp. 024702. Available also from WWW: <http://dx.doi.org/10.1143/JPSJ.79.024702>.
28. BLUNDELL, S. *Magnetism in condensed matter*. New York: Oxford University Press, 2001. ISBN 978-0198505914.
29. KITTEL, C. *Quantum Theory of Solids*. 2nd Revised Edition. New York: John Wiley & Sons, 1987. ISBN 978-0-471624127.
30. SUNDSTRÖM, L. J. Low temperature heat capacity of the rare earth metals. *Handbook on the physics and chemistry of rare earths*. 1978, vol. 1, pp. 379–410.

31. ELLIOTT, R. J. *Magnetic Properties of Rare Earth Metals*. 1st ed. New York: Springer US, 1972. ISBN 978-1-4757-5693-7.
32. MCELFFRESH, M. Fundamentals of magnetism and magnetic measurements. *Quantum Design*. 1994. Available also from WWW: (<http://www.qdusa.com/sitedocs/appNotes/mpms/FundPrimer.pdf>).
33. STEWART, G. R. Measurement of low-temperature specific heat. *Review of Scientific Instruments*. 1983, vol. 54, no. 1, pp. 1–11. Available also from WWW: (<http://scitation.aip.org/content/aip/journal/rsi/54/1/10.1063/1.1137207>).
34. *PPMS Heat Capacity Option User's Manual*. 1085-150, Rev. L3, 2010.
35. VENTURA, G.; PERFETTI, M. *Thermal properties of solids at room and cryogenic temperatures*. Dordrecht: Springer, 2014. Available also from WWW: (<http://dx.doi.org/10.1007/978-94-017-8969-1>). ISBN 9789401789691.
36. RIEGEL, S; WEBER, G. A dual-slope method for specific heat measurements. *Journal of Physics E: Scientific Instruments*. 1986, vol. 19, no. 10, pp. 790. Available also from WWW: (<http://stacks.iop.org/0022-3735/19/i=10/a=006>).
37. ČERMÁK, P. *Magnetic properties of  $R_2TIn_8$  and related tetragonal compounds*. 2014. Doctoral thesis. Charles University. Prague.
38. SIVARDIERE, J.; BARUCHEL, J., et al. *Neutron and Synchrotron Radiation for Condensed Matter Studies: Applications to Solid State Physics and Chemistry*. Berlin: Springer-Verlag, 1994. ISBN 978-3-540-57691-4.
39. HZB. *E6 Focusing Powder Diffractometer [online]*. Visited on: 17.4.2016. Available from WWW: ([http://www.helmholtz-berlin.de/pubbin/igama\\_output?modus=einzel&sprache=en&gid=1701&typoid=50728](http://www.helmholtz-berlin.de/pubbin/igama_output?modus=einzel&sprache=en&gid=1701&typoid=50728)).
40. TOVAR, M. (ed.). *Neutron-Scattering Instrumentation at the Research Reactor BER II*. Berlin: BENSC, 2007. Available also from WWW: ([https://www.helmholtz-berlin.de/media/media/grossgeraete/nutzerdienst/neutronen/instrumente/inst/bensc\\_all.pdf](https://www.helmholtz-berlin.de/media/media/grossgeraete/nutzerdienst/neutronen/instrumente/inst/bensc_all.pdf)).
41. BUCHSTEINER, A.; STÜSSER, N. Optimizations in angular dispersive neutron powder diffraction using divergent beam geometries. *Nuclear Instruments and Methods in Physics Research Section A: Accelerators, Spectrometers, Detectors and Associated Equipment*. 2009, vol. 598, no. 2, pp. 534–541. Available also from WWW: (<http://dx.doi.org/10.1016/j.nima.2008.09.022>).
42. TOVAR, M. (ed.). *Neutron-Scattering Instrumentation at the Research Reactor BER II*. Berlin: BENSC, 2001. Available also from WWW: ([https://www.helmholtz-berlin.de/media/media/oea/web/pr\\_webseite/druckschriften/infos/neutr\\_scat\\_instrum.pdf](https://www.helmholtz-berlin.de/media/media/oea/web/pr_webseite/druckschriften/infos/neutr_scat_instrum.pdf)).
43. FULDE, P.; LOEWENHAUPT, M. Magnetic excitations in crystal-field split  $4f$  systems. *Advances in Physics*. 1985, vol. 34, no. 5, pp. 589–661. Available also from WWW: (<http://dx.doi.org/10.1080/00018738500101821>).
44. MOZE, O. Chapter 4: Crystal field effects in intermetallic compounds studied by inelastic neutron scattering. In *Handbook of Magnetic Materials*. 1998, pp. 493–624. Available also from WWW: (<http://www.sciencedirect.com/science/article/pii/S1567271998110089>).

45. ILL. *Webpages of the The Time-of-flight and High-Resolution Group at ILL Grenoble [online]*. Updated: 30. 04. 2010. Visited on: 18. 4. 2016. Available from WWW: <https://www.ill.eu/instruments-support/instruments-groups/groups/tof/>.
46. ILL. *Thermal neutron time-of-flight spectrometer IN4C [online]*. Updated: 29. 10. 2015. Visited on: 18. 4. 2016. Available from WWW: <https://www.ill.eu/instruments-support/instruments-groups/instruments/in4c>.
47. CICOGNANI, G; MUTKA, H; SACCHETTI, F. The thermal neutron time-of-flight spectrometer IN4C. *Physica B: Condensed Matter*. 2000, vol. 276 - 278, pp. 83 –84. Available also from WWW: <http://www.sciencedirect.com/science/article/pii/S0921452699013666>. ISSN 0921-4526.
48. ISIKAWA, Y; KATO, D; MITSUDA, A; MIZUSHIMA, T; KUWAI, T. Magnetic properties of single crystals of  $R\text{CoIn}_5$  ( $R = \text{Tb, Dy, Ho, Er, Yb}$ ). *Journal of magnetism and magnetic materials*. 2004, vol. 272, pp. 635–636. Available also from WWW: <http://dx.doi.org/10.1016/j.jmmm.2003.12.1021>.
49. HUDIS, J.; HU, R.; BROHOLM, C.; MITROVIĆ, V.; PETROVIC, C. Magnetic and transport properties of  $R\text{CoIn}_5$  ( $R = \text{Pr; Nd}$  and  $R\text{CoGa}_5$  ( $R = \text{Tb-Tm}$ )). *Journal of magnetism and magnetic materials*. 2006, vol. 307, no. 2, pp. 301–307. Available also from WWW: <http://dx.doi.org/10.1016/j.jmmm.2006.04.023>.
50. HIEU, N. V.; SHISHIDO, H.; TAKEUCHI, T., et al. Unique Magnetic Properties of  $\text{NdRhIn}_5$ ,  $\text{TbRhIn}_5$ ,  $\text{DyRhIn}_5$ , and  $\text{HoRhIn}_5$ . *Journal of the Physical Society of Japan*. 2006, vol. 75, no. 7, pp. 074708. Available also from WWW: <http://dx.doi.org/10.1143/JPSJ.75.074708>.
51. HIEU, N. V.; TAKEUCHI, T.; SHISHIDO, H., et al. Magnetic Properties and Crystalline Electric Field Scheme in  $R\text{RhIn}_5$  ( $R$ : Rare Earth). *Journal of the Physical Society of Japan*. 2007, vol. 76, no. 6, pp. 064702. Available also from WWW: <http://dx.doi.org/10.1143/JPSJ.76.064702>.
52. JOSHI, D. A.; TOMY, C. V.; MALIK, S. K. Magnetic, transport and thermal properties of ternary indides  $R_2\text{CoIn}_8$  ( $R = \text{rare earths and Y}$ ). *Journal of Physics: Condensed Matter*. 2007, vol. 19, no. 13, pp. 136216. Available also from WWW: <http://stacks.iop.org/0953-8984/19/i=13/a=136216>.
53. KRATOCHVÍLOVÁ, M.; BARTHA, A.; DIVIŠ, M., et al. Anisotropic magnetic properties of  $\text{RE}_2\text{CoIn}_8$  ( $\text{RE} = \text{Pr, Nd, Dy}$ ) compounds. *Physica B: Condensed Matter*. 2014, vol. 444, pp. 65–69. Available also from WWW: <http://dx.doi.org/10.1016/j.physb.2014.03.031>. ISSN 0921-4526.
54. JOSHI, D. A.; NAGALAKSHMI, R; DHAR, S.; THAMIZHAVEL, A. Anisotropic magnetization studies of  $R_2\text{CoGa}_8$  single crystals ( $R = \text{Gd, Tb, Dy, Ho, Er, Tm, Y, and Lu}$ ). *Physical Review B*. 2008, vol. 77, no. 17, pp. 174420. Available also from WWW: <http://dx.doi.org/10.1103/PhysRevB.77.174420>.
55. PAGLIUSO, P.; THOMPSON, J.; HUNDLEY, M.; SARRAO, J. Crystal-field-induced magnetic frustration in  $\text{NdMIn}_5$  and  $\text{Nd}_2\text{MIn}_8$  ( $M = \text{Rh, Ir}$ ) antiferromagnets. *Physical Review B*. 2000, vol. 62, no. 18, pp. 12266. Available also from WWW: <http://dx.doi.org/10.1103/PhysRevB.62.12266>.

56. ČERMÁK, P.; KRATOCHVÍLOVÁ, M.; PAJSKR, K.; JAVORSKÝ, P. Magnetic phase diagrams of  $R_2\text{RhIn}_8$  ( $R = \text{Tb, Dy, Ho, Er}$  and  $\text{Tm}$ ) compounds. *Journal of physics. Condensed matter: an Institute of Physics journal*. 2012, vol. 24, no. 20, pp. 206005. Available also from WWW: <http://dx.doi.org/10.1088/0953-8984/24/20/206005>.
57. ČERMÁK, P.; PROKEŠ, K.; OULADDIAF, B., et al. Magnetic structures in the magnetic phase diagram of  $\text{Ho}_2\text{RhIn}_8$ . *Physical Review B*. 2015, vol. 91, no. 14, pp. 144404. Available also from WWW: <http://dx.doi.org/10.1103/PhysRevB.91.144404>.
58. JAVORSKÝ, P.; PAJSKR, K.; KLICPERA, M., et al. High-field magnetization and magnetic phase diagrams in  $\text{Nd}_2\text{RhIn}_8$  and  $\text{Tb}_2\text{RhIn}_8$ . *Journal of Alloys and Compounds*. 2014, vol. 598, pp. 278–281. Available also from WWW: <http://dx.doi.org/10.1016/j.jallcom.2014.02.042>.
59. GRIVEAU, J.-C.; GOFRYK, K.; REBIZANT, J. Transport and magnetic properties of the superconductor  $\text{NpPd}_5\text{Al}_2$ . *Phys. Rev. B*. 2008, vol. 77, pp. 212502. Available also from WWW: <http://link.aps.org/doi/10.1103/PhysRevB.77.212502>.
60. GOFRYK, K.; GRIVEAU, J.-C.; COLINEAU, E., et al. Kondo behavior in superconducting  $\text{NpPd}_5\text{Al}_2$ . *Phys. Rev. B*. 2009, vol. 79, pp. 134525. Available also from WWW: <http://link.aps.org/doi/10.1103/PhysRevB.79.134525>.
61. ONIMARU, T.; F. INOUE, Y.; SHIGETOH, K., et al. Giant uniaxial anisotropy in the magnetic and transport properties of  $\text{CePd}_5\text{Al}_2$ . *Journal of the Physical Society of Japan*. 2008, vol. 77, no. 7, pp. 074708. Available also from WWW: <http://dx.doi.org/10.1143/JPSJ.77.074708>.
62. HONDA, F.; MEASSON, M.; NAKANO, Y., et al. Magnetic and superconducting properties of a pressure-induced superconductor  $\text{CePd}_5\text{Al}_2$ . *Physica B: Condensed Matter*. 2009, vol. 404, no. 19, pp. 3202–3205. Available also from WWW: <http://dx.doi.org/10.1143/JPSJ.79.024702>.
63. INOUE, Y.; ONIMARU, T.; ISHIDA, A., et al. Sinusoidally modulated magnetic structure of a Kondo lattice compound  $\text{CePd}_5\text{Al}_2$ . In *Journal of Physics: Conference Series*. No. 3, 2010, pp. 032023. Available also from WWW: <http://dx.doi.org/10.1088/1742-6596/200/3/032023>.
64. HAGA, Y.; AOKI, D.; HOMMA, Y., et al. Crystal structure and magnetic properties of the new ternary actinide compounds  $\text{AnPd}_5\text{Al}_2$  ( $\text{An} = \text{U, Np}$ ). *Journal of Alloys and Compounds*. 2008, vol. 464, no. 1, pp. 47–50. Available also from WWW: <http://dx.doi.org/10.1016/j.jallcom.2007.10.037>.
65. GRIVEAU, J.-C.; GOFRYK, K.; COLINEAU, E.; REBIZANT, J. Crystal structure and physical properties of  $\text{PuPd}_5\text{Al}_2$ . *Journal of Nuclear Materials*. 2009, vol. 385, no. 1, pp. 11–14. Available also from WWW: <http://dx.doi.org/10.1016/j.jnucmat.2008.10.034>.
66. RIBEIRO, R.; INOUE, Y.; ONIMARU, T., et al. Magnetic properties of  $\text{RPd}_5\text{Al}_2$  ( $R = \text{Y, Ce, Pr, Nd, Sm, Gd}$ ). *Physica B: Condensed Matter*. 2009, vol. 404, no. 19, pp. 2946–2948. Available also from WWW: <http://dx.doi.org/10.1016/j.physb.2009.07.038>.

67. HIROSE, Y.; NISHIMURA, N.; ENOKI, K., et al. Electrical and Magnetic Properties of New Yb-based Compound  $\text{YbPd}_5\text{Al}_2$ . *Journal of the Physical Society of Japan*. 2012, vol. 81, no. Suppl.B, pp. SB057. Available also from WWW: <http://dx.doi.org/10.1143/JPSJS.81SB.SB057>.
68. GRIVEAU, J.-C.; GOFRYK, K.; BOUËXIÈRE, D.; COLINEAU, E.; REBIZANT, J. Crystal structure and physical properties of  $^{243}\text{AmPd}_5\text{Al}_2$ . *Phys. Rev. B*. 2012, vol. 85, pp. 085108. Available also from WWW: <http://link.aps.org/doi/10.1103/PhysRevB.85.085108>.
69. BENNDORF, C.; STEGEMANN, F.; ECKERT, H.; JANKA, O. New transition metal-rich rare-earth palladium/platinum aluminides with  $\text{RET}_5\text{Al}_2$  composition: structure, magnetism and  $^{27}\text{Al}$  NMR spectroscopy. *Zeitschrift für Naturforschung B*. 2015, vol. 70, no. 2, pp. 101–110. Available also from WWW: <http://www.degruyter.com/view/j/znb.2015.70.issue-2/znb-2014-0223/znb-2014-0223.xml>.
70. DIVIŠ, M; ČERMÁK, P; JAVORSKÝ, P. Structural and electronic properties of  $\text{YPd}_5\text{Al}_2$ . *Physica B: Condensed Matter*. 2012, vol. 407, no. 2, pp. 276–279. Available also from WWW: <http://dx.doi.org/10.1016/j.physb.2011.10.048>.
71. ZUBÁČ, J.; VLÁŠKOVÁ, K.; PROKLEŠKA, J.; PROSCHEK, P.; JAVORSKÝ, P. Magnetic properties and phase diagram of  $\text{NdPd}_5\text{Al}_2$ . *Journal of Alloys and Compounds*. 2016, vol. 675, pp. 94–98. Available also from WWW: <http://www.sciencedirect.com/science/article/pii/S0925838816305345>. ISSN 0925-8388.
72. RODRÍGUEZ-CARVAJAL, J. Recent advances in magnetic structure determination by neutron powder diffraction. *Physica B: Condensed Matter*. 1993, vol. 192, no. 1, pp. 55–69.
73. JAVORSKÝ, P.; KAŠTIL, J.; MÍŠEK, M., et al. Pressure influence on magnetic properties of  $\text{Nd}_2\text{RhIn}_8$ . *Journal of Magnetism and Magnetic Materials*. 2016, vol. 411, pp. 98–102. Available also from WWW: <http://www.sciencedirect.com/science/article/pii/S0304885316302554>. ISSN 0304-8853.
74. MATHWORKS. *Global Optimization Toolbox User's Guide*. 2016. Visited on: 6.5.2016. Available from WWW: [http://www.mathworks.com/help/pdf\\_doc/gads/gads\\_tb.pdf](http://www.mathworks.com/help/pdf_doc/gads/gads_tb.pdf).
75. PAJSKR, K; JAVORSKÝ, P; DIVIŠ, M; ZUBÁČ, J; VLÁŠKOVÁ, K. Low-temperature magnetic phase diagram and specific heat of  $\text{Nd}_2\text{IrIn}_8$ . *Physica B: Condensed Matter*. 2016, vol. 483, pp. 94–98. Available also from WWW: <http://dx.doi.org/10.1016/j.physb.2015.12.015>.
76. DIVIŠ, M.; RUSZ, J.; MICHOR, H., et al. Magnetic properties of  $\text{NdNi}_2\text{B}_2\text{C}$  from first principles calculations. *Journal of Alloys and Compounds*. 2005, vol. 403, no. 1-2, pp. 29–33. Available also from WWW: <http://www.sciencedirect.com/science/article/pii/S0925838805010224>. ISSN 0925-8388.
77. SQUIRES, G. L. *Introduction to the Theory of Thermal Neutron Scattering*. Third. 2012. Cambridge Books Online. Available also from WWW: <http://dx.doi.org/10.1017/CB09781139107808>. ISBN 9781139107808.

78. DUQUE, J.; SERRANO, R. L.; GARCIA, D., et al. Field induced phase transitions on NdRhIn<sub>5</sub> and Nd<sub>2</sub>RhIn<sub>8</sub> antiferromagnetic compounds. *Journal of Magnetism and Magnetic Materials*. 2011, vol. 323, no. 7, pp. 954–956.
79. BECKER, B; RAMAKRISHNAN, S; MENOVSKY, A.; NIEUWENHUYS, G.; MYDOSH, J. Unusual Ordering Behavior in Single-Crystal U<sub>2</sub>Rh<sub>3</sub>Si<sub>5</sub>. *Physical Review Letters*. 1997, vol. 78, no. 7, pp. 1347.
80. FEYERHERM, R.; WIEBE, C. R.; GAULIN, B. D., et al. First-order transition to a noncollinear antiferromagnetic structure in U<sub>2</sub>Rh<sub>3</sub>Si<sub>5</sub>. *Phys. Rev. B*. 1997, vol. 56, pp. 13693–13696. Available also from WWW: <http://dx.doi.org/10.1103/PhysRevB.56.13693>.
81. MORI, A.; MIURA, Y.; TSUTSUMI, H., et al. First-Order Antiferromagnetic Transition and Fermi Surfaces in Semimetal EuSn<sub>3</sub>. *Journal of the Physical Society of Japan*. 2014, vol. 83, no. 2, pp. 024008. Available also from WWW: <http://dx.doi.org/10.7566/JPSJ.83.024008>.
82. GORBUNOV, D. I.; HENRIQUES, M. S.; ANDREEV, A. V., et al. Electronic properties of a distorted kagome lattice antiferromagnet Dy<sub>3</sub>Ru<sub>4</sub>Al<sub>12</sub>. *Phys. Rev. B*. 2014, vol. 90, pp. 094405. Available also from WWW: <http://link.aps.org/doi/10.1103/PhysRevB.90.094405>.
83. HENRIQUES, M.; GORBUNOV, D.; KRIEGNER, D., et al. Magneto-elastic coupling across the first-order transition in the distorted kagome lattice antiferromagnet Dy<sub>3</sub>Ru<sub>4</sub>Al<sub>12</sub>. *Journal of Magnetism and Magnetic Materials*. 2016, vol. 400, pp. 125–129. Proceedings of the 20th International Conference on Magnetism (Barcelona) 5-10 July 2015. Available also from WWW: <http://www.sciencedirect.com/science/article/pii/S0304885315303735>. ISSN 0304-8853.
84. ADROJA, D. T.; ANAND, V. K. Inelastic neutron scattering study on the non-centrosymmetric compounds PrCuAl<sub>3</sub> and NdCuAl<sub>3</sub>. *Phys. Rev. B*. 2012, vol. 86, pp. 104404. Available also from WWW: <http://link.aps.org/doi/10.1103/PhysRevB.86.104404>.
85. TOLINSKI, T.; HOSER, A.; ROLS, S.; KOWALCZYK, A.; SZLAFEREK, A. Crystal field states in CeCu<sub>4</sub>Al. *Solid State Communications*. 2009, vol. 149, no. 47-48, pp. 2240–2243. Available also from WWW: <http://www.sciencedirect.com/science/article/pii/S0038109809005511>. ISSN 0038-1098.
86. BLANCO, J. The determination of crystal field parameters in rare earth intermetallic compounds. *Journal of Alloys and Compounds*. 1998, vol. 275-277, pp. 518–525. Available also from WWW: <http://www.sciencedirect.com/science/article/pii/S0925838898003831>. ISSN 0925-8388.
87. JANOUŠOVÁ, B.; KULDA, J.; DIVIŠ, M.; SECHOVSKÝ, V.; KOMATSUBARA, T. Local symmetry of the crystal-field Hamiltonian of CePtSn by polarized neutron scattering. *Phys. Rev. B*. 2004, vol. 69, pp. 220412. Available also from WWW: <http://link.aps.org/doi/10.1103/PhysRevB.69.220412>.